DESIGN GUIDELINES, SCAN BEHAVIOR AND CHARACTERISTIC MODE ANALYSIS FOR A CLASS OF ULTRA-WIDEBAND MICROSTRIP PATCH ANTENNAS

A DISSERTATION IN
Electrical and Computer Engineering
and
Telecommunications and Computer Networking

Presented to the Faculty of the University
of Missouri–Kansas City in partial fulfillment of
the requirements for the degree

DOCTOR OF PHILOSOPHY

BY

MOHAMED MAHMOUD ELSEWE

MSEE, University of Missouri-Columbia, 2002

Kansas City, Missouri

2016

DESIGN GUIDELINES, SCAN BEHAVIOR AND CHARACTERISTIC MODE ANALYSIS FOR A CLASS OF ULTRA-WIDEBAND MICROSTRIP PATCH ANTENNAS

Mohamed Mahmoud Elsewe, Candidate for the Doctor of Philosophy Degree

University of Missouri – Kansas City, 2016

ABSTRACT

Ultra-wideband (UWB), low-profile microstrip patch antennas and phased arrays have their niche in many wireless communication and medical applications. In recent years, the U-slot patch antenna established itself as a versatile antenna that can be fine-tuned for ultra-wideband operations. The L-shaped probe feeding method has additionally led to improved impedance bandwidth for the U-slot patch antenna. The L-probe's simple structure together with its low production cost makes it an attractive feeding method for the U-slot microstrip patch antenna. In phased arrays, scan blindness due to surface wave excitations can reduce the scan bandwidth range. By reducing the mutual coupling between array elements, the scan blindness effects will be reduced. Also, by reducing the sidelobe levels and minimizing the effect of grating lobes in phased arrays, the array's scan performance and power efficiency can be improved.

In this dissertation, (1) a parametric study is performed on ε_r = 2.2 and 4.5 substrates for the design of ideal L-probe feed dimensions with optimum impedance bandwidth. Results show that first-pass optimum impedance bandwidth of over 50% is achieved using the ideal L-probe feed dimensions. (2) The mutual coupling between a 2-element UWB microstrip array using different patch orientations and U-slot topologies is examined for ε_r =

2.2 and 4.5 substrates to reduce the effect of scan blindness. Results, for $\varepsilon_r = 2.2$ substrate, indicate that a diamond patch orientation with opposite U-slot topology presents the least coupling between the array elements. For $\varepsilon_r = 4.5$ substrate, the E-plane patch orientation with parallel U-slot topology has the least coupling. (3) The scan behavior of 5x5 planar phased arrays using different patch orientations and U-slot topologies is examined for $\varepsilon_r = 2.2$ substrate. Results indicate that blind spots are less prevalent in the diamond patch orientation and more prevalent in the E-plane patch orientation which has the most coupling between the array elements. (4) The array patterns of a 17-element L-probe-fed U-slot microstrip linear phased array are examined at different combinations of uniform and nonuniform excitation and inter-element spacing. Results indicate that using nonuniform excitation and inter-element spacing can reduce the sidelobe levels by over -10dB as the array is scanned 60° away from broadside. (5) Lastly, the Theory of Characteristic Modes (TCM) is used to characterize the resonant behavior of different microstrip patch shapes, substrates and excitation feeds to realize a microstrip patch antenna design with optimum broadband behavior. Results indicate that a single-layer U-slot rectangular patch on $\varepsilon_r = 4.4$ substrate presents a highly radiating structure. Further modal analysis of this single-layer structure with a single T-probe feed shows that VSWR ≤ 2 impedance bandwidth in the order of 96% can be achieved. Experimental results show VSWR ≤ 2 impedance bandwidth in the order of 71%.

APPROVAL PAGE

The faculty listed below, appointed by the Dean of the School of Graduate Studies, have examined a dissertation titled "Design Guidelines, Scan Behavior and Characteristic Mode Analysis for a Class of Ultra-wideband Microstrip Patch Antennas," presented by Mohamed Mahmoud Elsewe, candidate for the Doctor of Philosophy degree, and hereby certify that in their opinion it is worthy of acceptance.

Supervisory Committee

Deb Chatterjee, Ph.D., Committee Chair
Department of Computer Science & Electrical Engineering

Ghulam M. Chaudhry, Ph.D.
Department of Computer Science & Electrical Engineering

Masud H Chowdhury, Ph.D.
Department of Computer Science & Electrical Engineering

Cory Beard, Ph.D.
Department of Computer Science & Electrical Engineering

Yugyung Lee, Ph.D.
Department of Computer Science & Electrical Engineering

CONTENTS

ILLUSTRATIONS

Figure Page

TABLES

Table Page

ACKNOWLEDGEMENTS

First and foremost, I would like to thank God for blessing me with the completion of this dissertation. I wish to express my sincere gratitude to my supervisor, Dr. Deb Chatterjee, for his guidance, support and encouragement. His knowledge and motivation inspired me in many ways and helped me through the hurdles I encountered during my tenure in the PhD program.

I am also grateful to Dr. Ghulam Chaudhry, Dr. Cory Beard, Dr. Masud Chowdhury, and Dr. Yugyung Lee for serving on my supervisory committee and for their valuable inputs on my research.

Many thanks are due to my parents, wife, and children who have in their own special ways inspired me to complete this dissertation.

I also would like to acknowledge the Department of Electrical and Computer Engineering and the School of Graduate Studies for allowing me the opportunity to fulfill my degree requirements as a part-time student.

CHAPTER 1

INTRODUCTION

1.1 Motivation

Ultra-wideband (UWB) antennas have a very wide frequency spectrum. In 2002, the FCC allocated the frequency range between 3.1 and 10.6 GHz for commercial use [1]. By FCC definition, systems with relative bandwidth larger than 20% or an absolute bandwidth larger than 500 MHz are considered UWB systems [1]. Some of the motivation points for UWB research are: (1) Higher data rates per Shannon's channel capacity theorem, which states that the capacity of a wireless channel varies linearly with bandwidth [2]. In other words, higher data rates can be achieved as the bandwidth over which the antenna transmits or receives data increases. (2) UWB communication is very secure. Any interference from other wireless systems will have to cover the entire UWB spectrum evenly to jam the UWB pulse [2]. (3) UWB wireless communication uses very low power transmission levels which are below acceptable noise floor levels [2]. Therefore, UWB technology does not cause much interference to other wireless communications. (4) UWB communication uses low cost transceivers which do not require any modulation or demodulation circuitry [2]. (5) Low-profile UWB microstrip patch antennas have promising applications in biomedical imaging. This is because lower frequencies provide good skin penetration and higher frequencies provide good image resolution.

In recent years, the microstrip patch antenna has been fine-tuned for UWB operations [3-13]. It is the purpose of this dissertation to characterize the various microstrip patch antenna's broadbanding techniques with the purpose of developing design guidelines

to aid the antenna design engineer in designing first-pass antenna structures with very wide bandwidth.

1.2 Microstrip Patch Antennas and Broadbanding Techniques

The Microstrip patch antenna (MSA) was first proposed in the 1953 by Deschamps [14], then it was researched more intensely in the 1970s by Munson [15] and Howell [16]. The MSA is a low-profile antenna that, in its basic form, consists of a metallic patch, dielectric substrate, and ground plane, as shown in Fig. 1.1. The patch shape can be square, rectangular, triangular, circular, or other irregular shape. The dielectric substrate can be made of materials with dielectric constant, ε_r, that ranges between 2.2 and 12 [17]. Due to its small physical dimension and low cost, the MSA finds uses in a variety of wireless communication applications, such as cellular phones, RFID, Wi-Fi, Bluetooth, GPS, and body area networks. Other uses include defense applications, such as conformal antennas on missiles and planes. Radar and satellite systems make use of MSA arrays. Biomedical imaging applications have made use of MSAs, especially in breast cancer detection and treatment [18-27]. The MSAs have a number of advantages [28], which are:

- Lightweight.
- Low profile and compact.
- Conformal, meaning they can conform to different shapes as in missiles.
- Low fabrication cost since they utilize the existing and widespread printed-circuit technology.
- Capable of linear and circular polarization.
- Support of dual- and triple-band frequency operations.

- Easily integrated with microwave integrated circuits.

Some of the disadvantages that MSAs suffer from are [28]:

- Narrow bandwidth with the higher dielectric constant substrates.
- Low efficiency due to dielectric and conductor losses.
- Surface wave excitations especially in thicker substrates.
- Low power handling ability.
- Additional radiation from feeds.

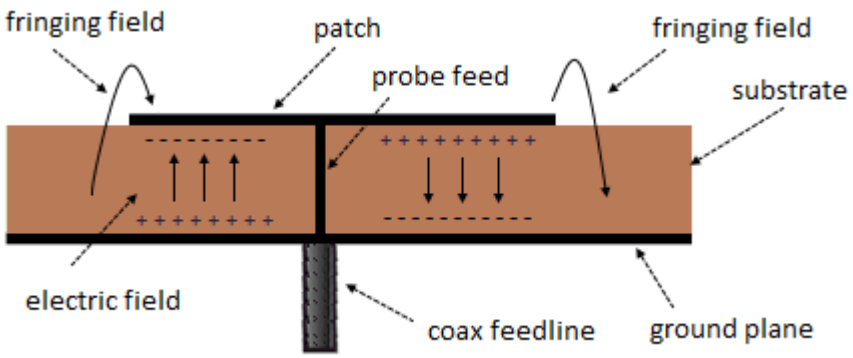

Fig. 1.1. Side view of microstrip patch antenna

The MSA can be fed by a variety of feeding methods shown in Fig. 1.2. There are three types of feeding methods: direct feeds, proximity-coupled feeds, and aperture-coupled feeds [29]. Direct feeds, in Fig. 1.2 (a), have narrow bandwidth since the probe introduces an inductance. Proximity-coupled feeds, in Fig. 1.2 (b), have more bandwidth since the gap between the probe and patch introduces capacitance which partially cancels the inductance

by the probe. Also, this permits the use of thicker substrates which introduces more bandwidth. Aperture-coupled feeds, in Fig. 1.2 (c), introduces more bandwidth since it isolates the feed system from the patch by a central ground plane with an aperture. Above the central ground plane is a substrate with low dielectric constant for better radiation. Below the central ground plane is a substrate with high dielectric constant and transmission line for better coupling of the wave to the line. The downside of this feeding method is the increase in the antenna dimension due to the double substrates. The proximity-coupled feeds, namely the probe feed with a gap, will be the primary feed used in this dissertation, since more bandwidth can be attained without increasing the antenna dimensions.

The current on the patch, represented by the magnetic field, is maximal at the center of the patch and minimal at the edges of the patch length. On the other hand, the voltage on the patch, represented by the electric field, is zero at the center of the patch and maximal near the left edge of the patch length and negative near the right edge of the patch length. It is the fringing electric fields on the patch edges, illustrated in Fig. 1.1, that add in phase and cause the patch to radiate. Since the antenna impedance is zero near the center of the patch and maximum at the edges, in order to match a 50-ohm feed to the patch, the feed needs to be placed off-center along the patch length.

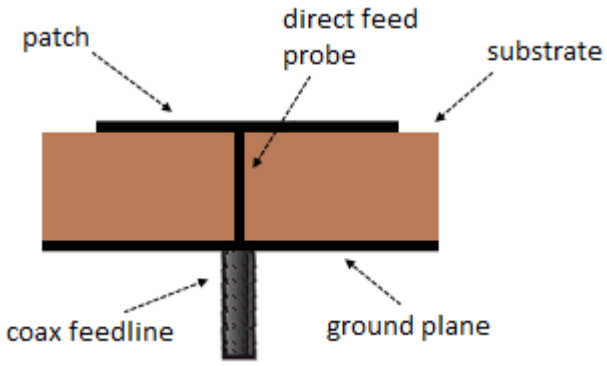

(a)

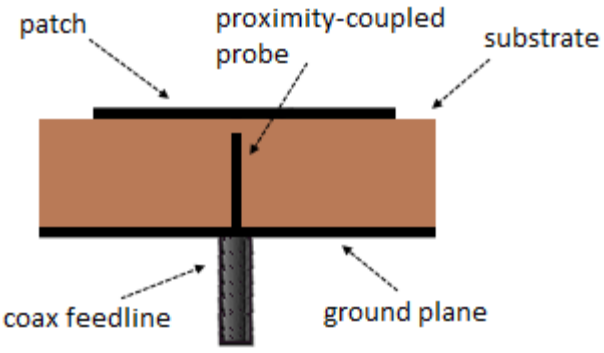

(b)

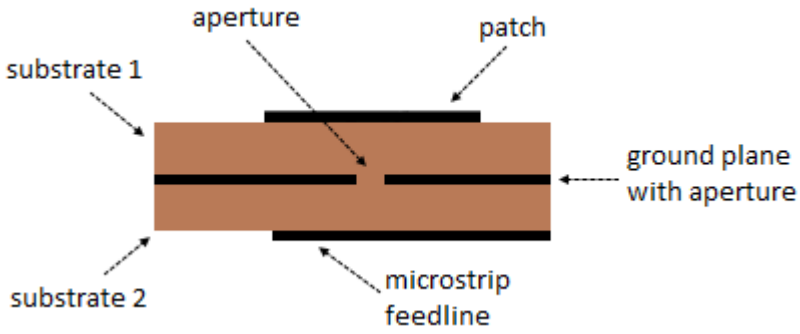

(c)

Fig. 1.2. Microstrip patch antenna feeding methods. (a) Direct feed (b) Proximity-coupled feed (c) Aperture-coupled feed

In a half-wave rectangular patch, the patch length, L, determines the resonant frequency of the antenna per Eq. 1.1 [29],

$$L = 0.49\frac{\lambda}{\sqrt{\varepsilon_r}} \tag{1.1}$$

where λ is the free-space resonant wavelength and ε_r is the dielectric constant of substrate. The patch width, W, controls the input impedance, $Z_{A,}$ of the antenna per Eq. 1.2 [29].

$$Z_A = 90\frac{\varepsilon_r^2}{\varepsilon_r - 1}\left(\frac{L}{W}\right)^2 \tag{1.2}$$

Per Eq. 1.2, as the patch width increases, the input impedance decreases. The fractional bandwidth, BW, of a rectangular patch antenna is described by Eq. 1.3 [29],

$$BW = 3.77\,\frac{\varepsilon_r - 1}{\varepsilon_r{}^2}\frac{W}{L}\,\frac{t}{\lambda} \tag{1.3}$$

where t is the dielectric substrate thickness. Per Eq. 1.3, as the dielectric substrate thickness increases, the bandwidth can be increased. Also, bandwidth is defined by Eq. 1.4 [28],

$$\mathrm{BW} = \frac{\mathrm{VSWR} - 1}{Q\sqrt{\mathrm{VSWR}}} \tag{1.4}$$

where Q is the quality factor defined as energy stored over power lost, and VSWR is the voltage standing wave ratio defined by Eq. 1.5 [28].

$$\mathrm{VSWR} = \frac{1 + |\Gamma|}{1 - |\Gamma|} \tag{1.5}$$

The Γ is the reflection coefficient, which is a measure of the reflected signal at the feed point. It is defined in Eq. 1.6 [28],

$$\Gamma = \frac{Z_{in} - Z_0}{Z_{in} + Z_0} \tag{1.6}$$

where Z_{in} is the input impedance of the antenna and Z_0 is the characteristic impedance of the feed line. A low VSWR value of 2 or less is a desirable goal of most antennas and indicates that only about 10% of the feed power is reflected and the remaining 90% is transmitted to the antenna. In addition, per Eq. 1.4, having a low quality factor is desirable to achieve higher bandwidth.

Since the purpose of this dissertation is to characterize the various microstrip patch antenna's broadbanding techniques and develop design guidelines for antennas with very wide bandwidth, it is worth noting some of the bandwidth broadening techniques found in the literature. Some of these techniques are:

1. By the use of substrates with low dielectric constant. Per Eq. 1.1, as you decrease the dielectric constant, the patch length increases. The bigger the patch, the more the

fringing fields, hence more radiation and bandwidth. The downside is an antenna with bigger footprint.

2. By the use of thicker substrates. The thicker the substrate, the more fringing fields exist, hence more radiation and bandwidth. The downside is more surface waves are introduced and antenna size is increased.
3. By the use of parasitic elements or patch slots. This introduces additional resonances in addition to the main patch resonance.
4. By the use of non-conventional probe feeds [30-32], such as L-shaped proximity coupled probe feed. The inductive reactance of the vertical arm of the L-probe feed partly suppresses the capacitive reactance of the horizontal arm, hence low reactance results, which indicates less power is stored in the near field of the antenna and thus more power is radiated.

1.3 Computational Electromagnetics Methods and Solvers

Computational Electromagnetics methods (CEM) are numerical methods which solve Maxwell's equations by breaking the model into a mesh of tetrahedrons or triangles and calculating the electric fields over the tetrahedron volume or calculating the current over the triangle surface. Two commonly used numerical methods in the analysis of microstrip patch antennas are the Method of Moments (MoM) and the Finite Element Method (FEM). MoM is implemented by the commercially available 3D solver, FEKO. MoM is an integral equation based method in the frequency domain. It is ideal for large open problems, e.g. antennas mounted on a vehicle. FEM is implemented by the commercially available 3D solvers, HFSS and FEKO. FEM is a partial differential equation based method in the

frequency domain. It is ideal for modeling irregular shapes and heterogeneous objects. The next two sections will go over the steps involved in each method to solve electromagnetic problems.

1.3.1 The Method of Moments

The inhomogeneous equation, Eq. 1.7 [33], represents most electromagnetic problems,

$$L(f) = g \tag{1.7}$$

where L is a linear integral or differential operator, g is a known function, and f is an unknown function. The residual of Eq. 1.7 can be defined as [33]:

$$R = L(f) - g \tag{1.8}$$

The next step is to discretize function f into a set of linearly independent basis functions, f_n, [33]:

$$f = \sum_n \alpha_n f_n \tag{1.9}$$

where α_n are unknown complex coefficients. Next, Eq. 1.9 is substituted in Eq. 1.8 to yield [33]:

$$R = \sum_n \alpha_n L(f_n) - g \tag{1.10}$$

Next, the inner product of Eq. 1.10 is taken with a set of test (weight) functions, w_m, then set to zero [33]:

$$<R, w_m> = 0 \qquad m = 1, 2, 3, \ldots \tag{1.11}$$

Eq. 1.11 can be written in the expanded form [33]:

$$\sum_n \alpha_n <w_m, L(f_n)> = <w_m, g> \qquad m = 1, 2, 3, \ldots \tag{1.12}$$

Eq. 1.12 can be written in the matrix form [33]:

$$[l][\alpha] = [p] \tag{1.13}$$

where

$$[l] = \begin{bmatrix} <w_1, Lf_1> & <w_1, Lf_2> & \ldots \\ <w_2, Lf_1> & <w_2, Lf_2> & \ldots \\ \ldots & \ldots & \ldots \end{bmatrix} \tag{1.14a}$$

$$[\alpha] = \begin{bmatrix} \alpha_1 \\ \alpha_2 \\ . \\ . \end{bmatrix} \tag{1.14b}$$

$$[p] = \begin{bmatrix} <w_1, g> \\ <w_2, g> \\ . \\ . \end{bmatrix} \tag{1.14c}$$

Finally, the matrix equation, Eq. 1.13, is solved and the α_n coefficients are substituted in Eq. 1.9 [33].

$$f = [f]^t [\alpha] \tag{1.15}$$

where $[f]^t$ is the basis vector.

1.3.2 The Finite Element Method

The FEM analysis consists of four major steps [34]:

1. The meshing of the object geometry into a finite number of elements. The dielectric in each element is homogeneous. Examples of some of the finite elements used to model the geometry of one-dimensional, two-dimensional and three-dimensional problems are shown in Fig. 1.3.

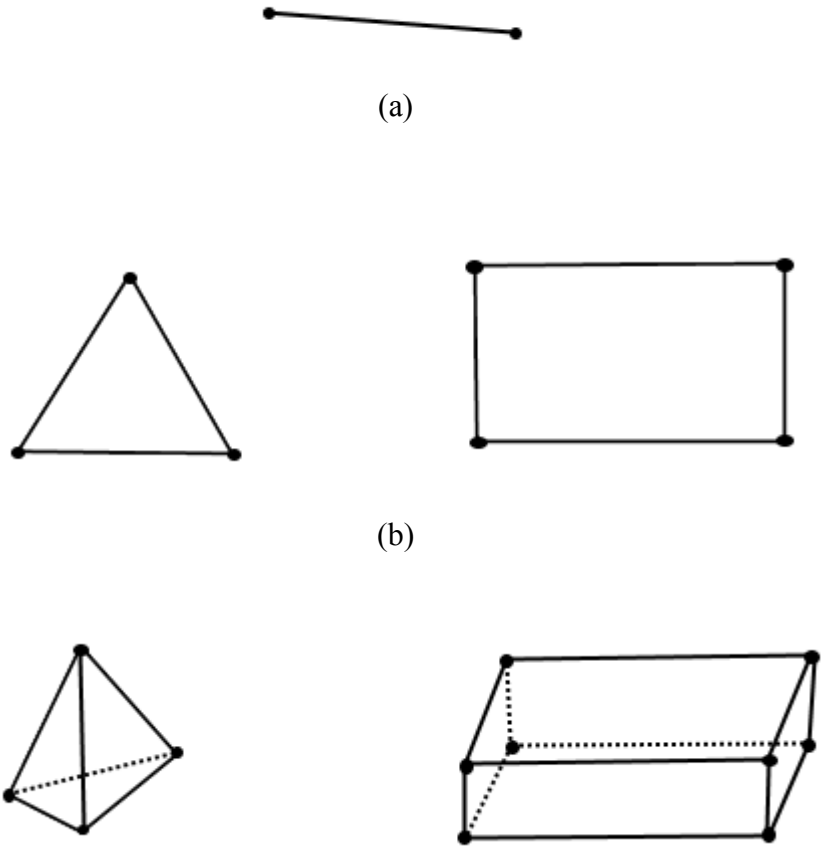

Fig. 1.3. Examples of finite elements. (a) 1D line (b) 2D triangle and rectangle (c) 3D tetrahedron and hexahedron

2. The expansion of an unknown function by a basis function, which results in the derivation of an element matrix.
3. The assembly of all element matrices to yield the system matrix.
4. The solution of the system matrix to determine the unknown function.

1.4 Summary of Contributions

This dissertation presents contributions to the antenna design community which are presented in the following chapters.

In chapter 2, a parametric study is performed for the design of ideal L-probe feed dimensions with optimum impedance bandwidth. Optimum impedance bandwidth of over 50% is achieved on first pass using the developed ideal L-probe feed dimensions.

In chapter 3, the mutual coupling between a 2-element UWB microstrip array using different patch orientations and U-slot topologies is examined to reduce the effect of scan blindness. The patch orientations with the least coupling between the array elements are presented.

In chapter 4, the scan behavior of 5x5 planar phased arrays using different patch orientations and U-slot topologies is examined. The patch orientations with the least number of blind spots and least coupling between the array elements are presented. Also, the array patterns of a 17-element L-probe-fed U-slot microstrip linear phased array are examined at different combinations of uniform and nonuniform excitation and inter-element spacing. Using nonuniform excitation and inter-element spacing, the sidelobe levels can be reduced by over -10dB as the array is scanned 60° away from broadside.

In chapter 5, the resonant behavior of different microstrip patch shapes, substrates and excitation feeds are analyzed using the Theory of Characteristic Modes to identify the individual antenna structures which are more resonant and hence contribute significantly to the radiated fields. The highly radiating structure of a single-layer U-slot rectangular patch on $\varepsilon_r = 4.4$ substrate fed by a single T-probe, which achieves 96% impedance bandwidth, is realized.

This dissertation incorporates material from previously published papers by the author in accordance with the copyright policies of the Institute of Electrical and Electronics Engineers (IEEE) and the Applied Computational Electromagnetics Society (ACES). Some portion of chapter 2 includes the results and discussions found in [45] (© 2016 ACES). Some portion of chapter 3 includes the results and discussions found in [57] (© 2016 ACES). Some portion of chapter 4 includes the results and discussions found in [64] (© 2014 IEEE) and [65] (© 2015 IEEE). Some portion of chapter 5 includes the results and discussions found in [85, 86, 88] (© 2016 ACES) and [87, 89] (© 2016 IEEE).

CHAPTER 2

UWB MICROSTRIP PATCH ANTENNA FEED DESIGN GUIDELINES

Low-profile and UWB microstrip patch antennas are finding their place in many wireless communication applications like WLAN and WiMAX [35-37], and medical applications like breast cancer detection [18-27]. In recent years, the U-slot patch antenna proved to be a versatile antenna that can be fine-tuned for dual-band, triple-band, and wideband operations, in addition to supporting linear and circular polarization operations [38]. Dual-band operation is particularly important in some wireless communication applications, and wideband operation is useful in UWB medical imaging and detection applications.

Several feeding structure designs for the U-slot patch antenna are proposed in the literature [30-32]. The L-shaped probe feeding method [39], in particular, has led to improved impedance bandwidth of 38% for the U-slot patch antenna [30]. Moreover, its simple structure and low production cost [40] make it an attractive feeding method for the U-slot microstrip patch antenna.

In this chapter, the U-slot patch antenna design method of dimensional invariance, developed and validated in earlier work [41-43], is utilized to realize an initial, low-profile, wideband design. Building on this initial wideband design and work in [44], this study establishes ideal L-probe feed dimensions which propose empirical guidelines for the design of L-probe feeds to yield first-pass optimum impedance bandwidth.

In section 2.1, the U-slot patch design method is discussed. In section 2.2, an extensive parametric study on two substrates, $\varepsilon_r = 2.2$ and 4.5, is presented to find the ideal L-probe dimensions which yield optimum impedance bandwidth. In section 2.3, a time

domain analysis is presented to evaluate the suitability of the L-probe fed U-slot patch antenna design for UWB pulse applications. In section 2.4, an empirical L-probe design technique is developed using the ideal L-probe dimension information established in section 2.2. The new L-probe design technique is then validated on substrates with different permittivities, ε_r = 3.27, 6.0 and 9.2.

2.1 The Method of Dimensional Invariance

The method of dimensional invariance described in [41] is utilized in this paper to realize the U-slot antenna patch dimensions, shown in Fig. 2.1. This method relies on empirical formulas to first obtain the rectangular patch dimensions, then uses the dimensional invariance relationships in Table 2.1 to derive the U-slot dimensions. The method employs few criteria for substrate height, h, and patch width, W, that is $\frac{h\sqrt{\varepsilon r}}{\lambda} \approx 0.15$; $\frac{W}{L} \approx 1.385$ and $(3.5 \leq \frac{W}{h} \leq 5.5)$. Once $\frac{W}{h}$ ratio is determined using the method's empirical equations, relationships in Table 2.1 can be used to derive the topology of the U-slot patch. MATLAB code (see Appendix A.1) is used to implement the method of dimensional invariance to calculate the U-slot antenna dimensions.

Comparative analysis between this method and another U-slot design method is presented in [42], which highlights the advantages of the method of dimensional invariance with respect to enhanced bandwidth and applicability to low and high permittivity substrates. Experimental validation of the design method of dimensional invariance in the design of U-slot microstrip patch antenna is reported from earlier work in [43], in which HFSS simulation results agree with experimental results as shown in Fig. 2.2. In the absence

of experimental results to validate the simulation results in this work, further validation of the results presented in the published work [43] using FEKO MoM shows good agreement with the experimental data presented in Fig. 2.2. The discrepancy between measured and simulated MoM results is mainly due to the infinite ground plane assumption in MoM method.

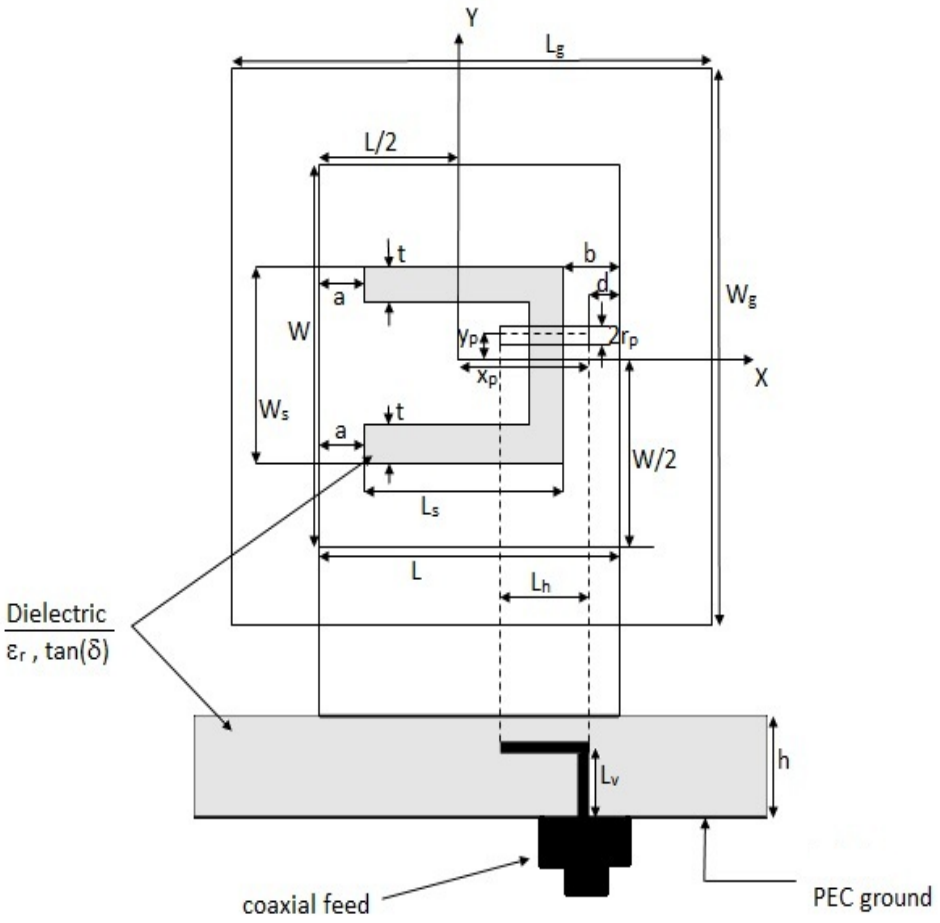

Fig. 2.1. Geometry of L-shaped, probe-fed, rectangular patch U-slot microstrip antenna [45]

(© 2016 ACES)

Table 2.1: Dimensional invariance in U-slot designs for various substrates [41]

ε_r	$\frac{L}{Ls}$	$\frac{Ws}{Ls}$	$\frac{Ls}{b}$	$\frac{t}{Ws}$	$\frac{W}{Ws}$
2.33	1.445	0.777	4.5	0.144	2.573
4.0	1.443	0.776	4.51	0.144	2.573
9.8	1.442	0.777	4.48	0.144	2.574

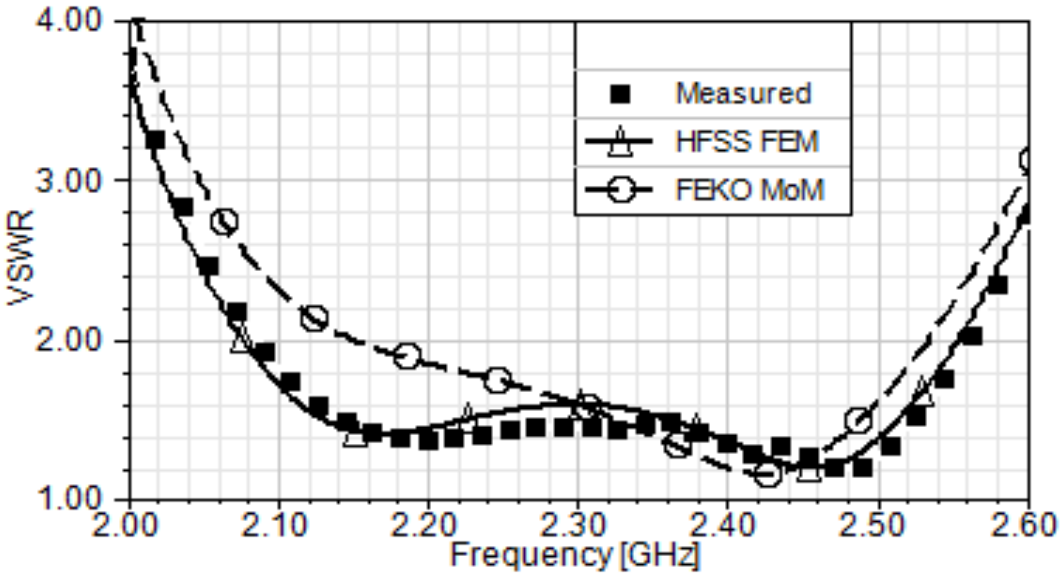

Fig. 2.2. Experimental and simulated VSWR of a probe-fed U-slot patch antenna [45] (© 2016 ACES)

2.2 Parametric Study of L-probe Dimensions

The parametric studies in this section are simulated and analyzed using the commercially available EM full-wave solvers, FEKO and HFSS, described in chapter 1. Simulation results using the Method of Moments (MoM) and Finite Element Method (FEM) solvers within FEKO are validated with simulation results using the HFSS FEM solver. The FEKO and HFSS FEM solvers have the same underlying computational electromagnetic

method and hence are expected to produce comparable results. Table 2.2 shows the dimensions of the U-slot microstrip patch antenna used in the parametric study, which are derived from the aforementioned method of dimensional invariance for a 2.4 GHz design frequency. Two substrate materials are studied: the *Rogers RT/Duroid 5880* substrate material with $\varepsilon_r = 2.2$ and $\tan(\delta) = 0.0009$ and the *Rogers TMM 4* substrate material with $\varepsilon_r = 4.5$ and $\tan(\delta) = 0.002$. Further simulation optimization runs were performed to arrive at the substrate height and probe position which yield best bandwidth.

Table 2.2: U-slot microstrip patch antenna dimensions for various substrates [45] (© 2016 ACES)

	$\varepsilon_r = 2.2$	**$\varepsilon_r = 4.5$**
a	5.17	3.61
b	5.17	3.61
W	46.53	32.54
L	33.6	23.49
L_s	23.26	16.27
t	2.6	1.82
W_s	18.09	12.65
r_p	1	1
x_p	13.8	8.745
y_p	1	-3
d	3	3
h	14	12

*All values are in mm.

In FEKO MoM solver, infinite substrate and ground is assumed. In FEKO FEM and HFSS FEM solvers, the substrate and ground (W_g and L_g) dimensions are extended by $\lambda/2$, where λ corresponds to the lower bandwidth frequency, from the edge of the patch to simulate an infinite substrate and ground for a more suited comparison between the FEM and MoM solvers. A radiation air box boundary which is $\lambda/4$, where λ corresponds to the lower bandwidth frequency, above the patch is used. The microstrip patch mesh size is $\lambda/20$, where λ corresponds to the upper bandwidth frequency. A 50-ohm coaxial feed line is used to feed the L-probe.

In this section, parametric studies are performed on two substrates, $\varepsilon_r = 2.2$ and 4.5, in which the horizontal length, L_h, and vertical length, L_v, of the L-probe are varied to find the L-probe dimensions with the highest impedance bandwidth. VSWR results for selected L_h and L_v variations are presented to show the results of three EM solvers on one figure for the sake of comparison and validation.

2.2.1 For $\varepsilon_r = 2.2$ substrate

The horizontal length, L_h, is varied at 11 different points between 5 and 13mm. L_v is fixed at 10mm. As shown in the Fig. 2.3, a wideband behavior is observed for the L_h values equal to 11mm and 12mm. Figure 2.4 summarizes the relationship between L_h/λ_o (where λ_o is the free-space wavelength corresponding to the 2.4 GHz design frequency) and bandwidth and shows good agreement between the HFSS and FEKO results for L_h = 5-13mm (0.04-0.11λ_o). As shown in Fig. 2.4, optimum bandwidth of approximately 50% is achieved when L_h is equal to 0.08-0.11λ_o.

Figure 2.5 shows the effect of varying L_h on the input impedance behavior of the U-slot patch antenna in HFSS and FEKO simulations for 1.5-4.0 GHz sweep. As shown in Fig. 2.5, the Smith charts indicate the trend that as L_h increases, the impedance loop moves toward the inductive upper half of the Smith chart. The L_h values of 10-13mm, which correspond to 0.08-0.11λ_o, are closest to the center locus (VSWR=1) of the Smith chart, indicating the highest wideband impedance behavior.

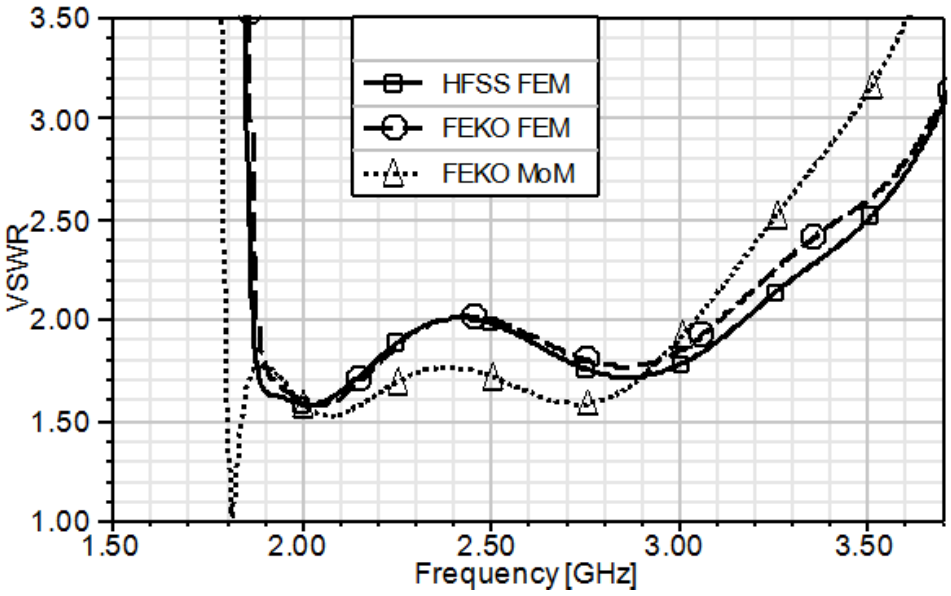

(a)

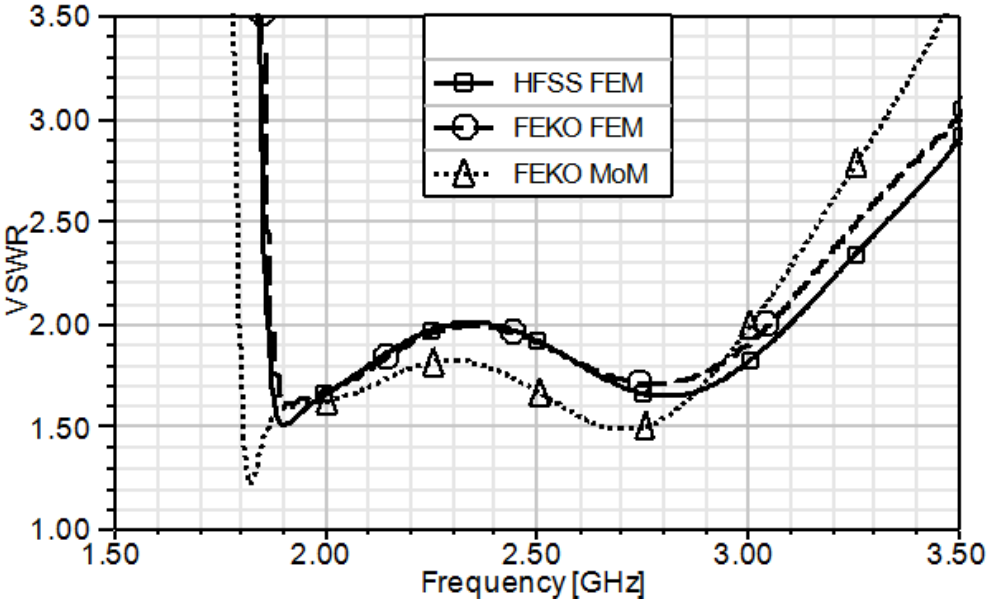

(b)

Fig. 2.3. VSWR for different L_h and $\varepsilon_r = 2.2$ substrate with fixed $L_v = 10$mm. (a) $L_h = 11$mm (b) $L_h = 12$mm [45] (© 2016 ACES)

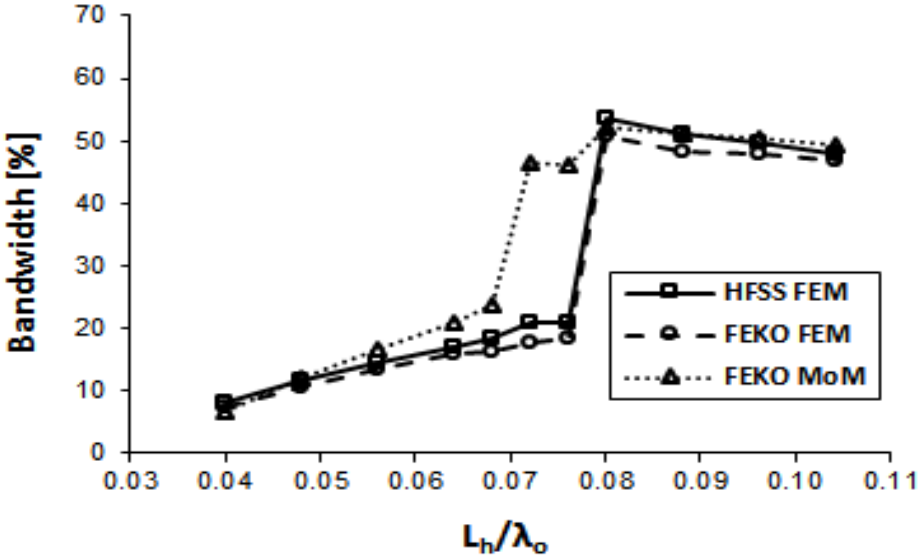

Fig. 2.4. Bandwidth versus L_h/λ_o for $\varepsilon_r = 2.2$ substrate [45] (© 2016 ACES)

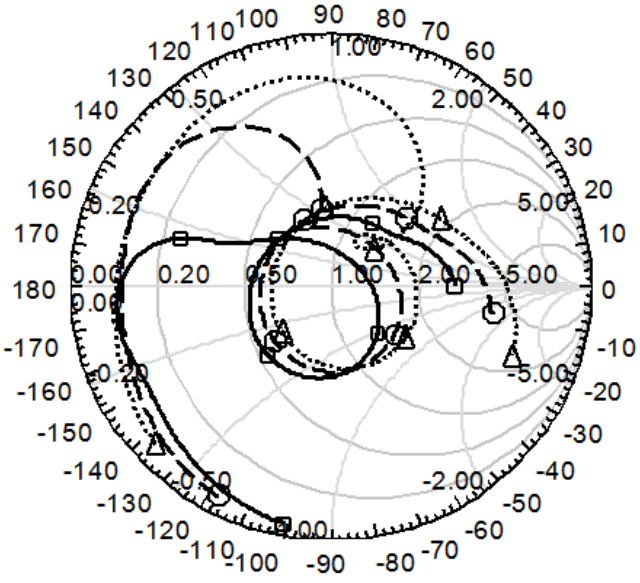

(a)

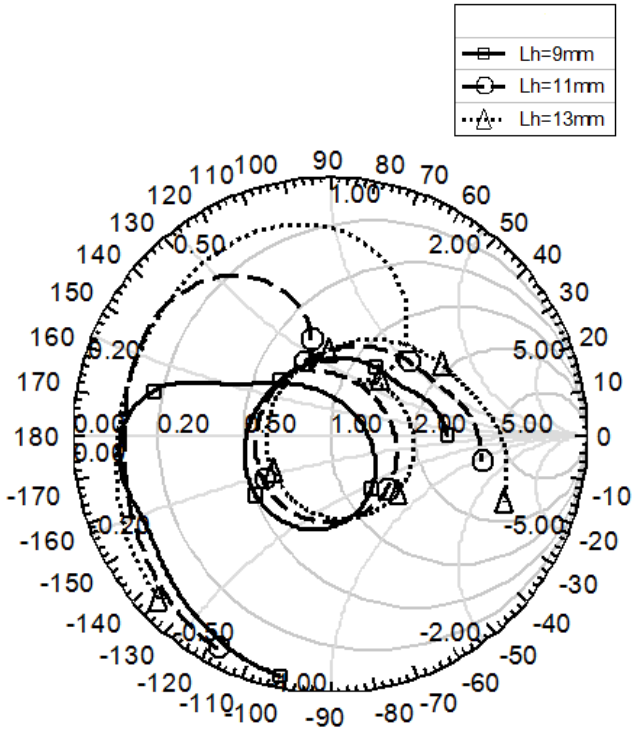

(b)

Fig. 2.5. Smith chart for different L_h and $\varepsilon_r = 2.2$ substrate. (a) HFSS FEM. (b) FEKO FEM

The vertical length, L_v, is varied at 9 different points between 7 and 12mm. L_h is fixed at 12mm. As shown in the Fig. 2.6, a dual-band behavior is observed for the L_v values equal to 11mm and 12mm. Figure 2.7 summarizes the relationship between L_v/λ_o and bandwidth and shows good agreement between the HFSS and FEKO results for L_v = 7-12mm (0.05-0.10λ_o). As shown in Fig. 2.7, optimum bandwidth of approximately 50% is achieved when L_v is equal to 10mm (0.08λ_o). Also, wideband behavior is shown in Fig. 2.3 when L_v = 10mm.

Figure 2.8 shows the effect of varying L_v on the input impedance behavior of the U-slot patch antenna in HFSS and FEKO simulations for 1.5-4.0 GHz sweep. As in the L_h case, the Smith charts in Fig. 2.8 indicate the trend that as L_v increases, the impedance values move toward the inductive upper half of the Smith chart. The impedance loop of L_v = 10mm, which corresponds to 0.08λ_o, is closest to the center locus (VSWR=1) of the Smith chart, indicating the highest wideband impedance behavior.

The antenna gain for the wideband case of L-probe dimensions L_v = 10mm and L_h = 12mm is illustrated in Fig. 2.9. As shown in the figure, there is good agreement in the gain between the HFSS and FEKO simulation results. Also, the antenna gain is around 5 dB for the 1.9-3.2 GHz (~50%) bandwidth achieved by these L-probe dimensions.

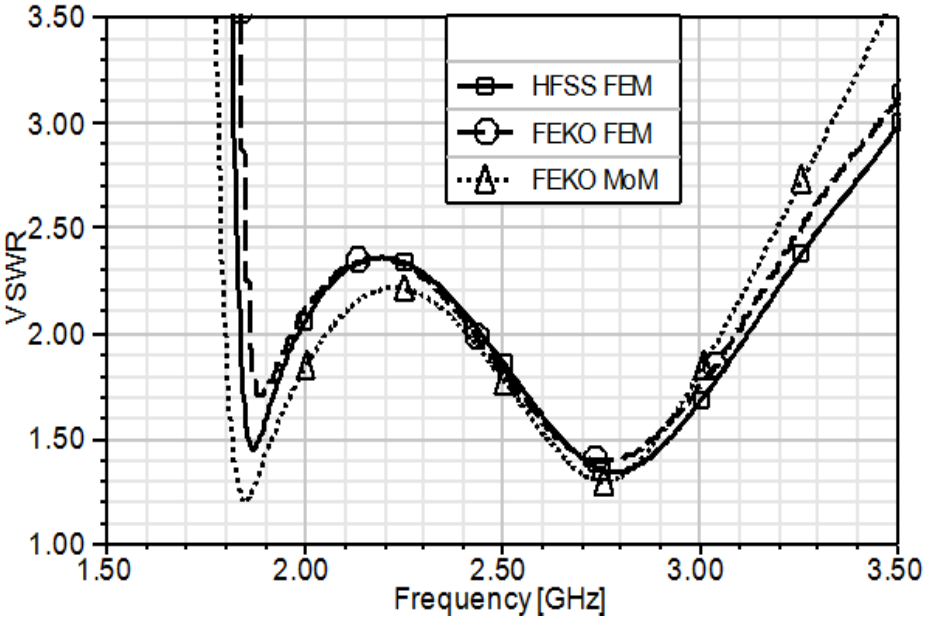

(a)

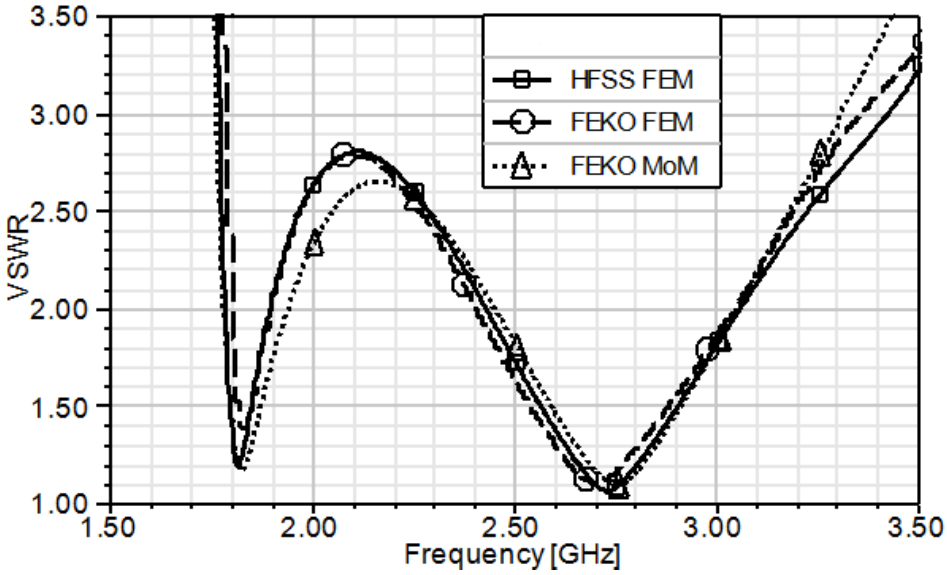

(b)

Fig. 2.6. VSWR for different L_v and $\varepsilon_r = 2.2$ substrate with fixed $L_h = 12$mm. (a) $L_v = 11$mm (b) $L_v = 12$mm [45] (© 2016 ACES)

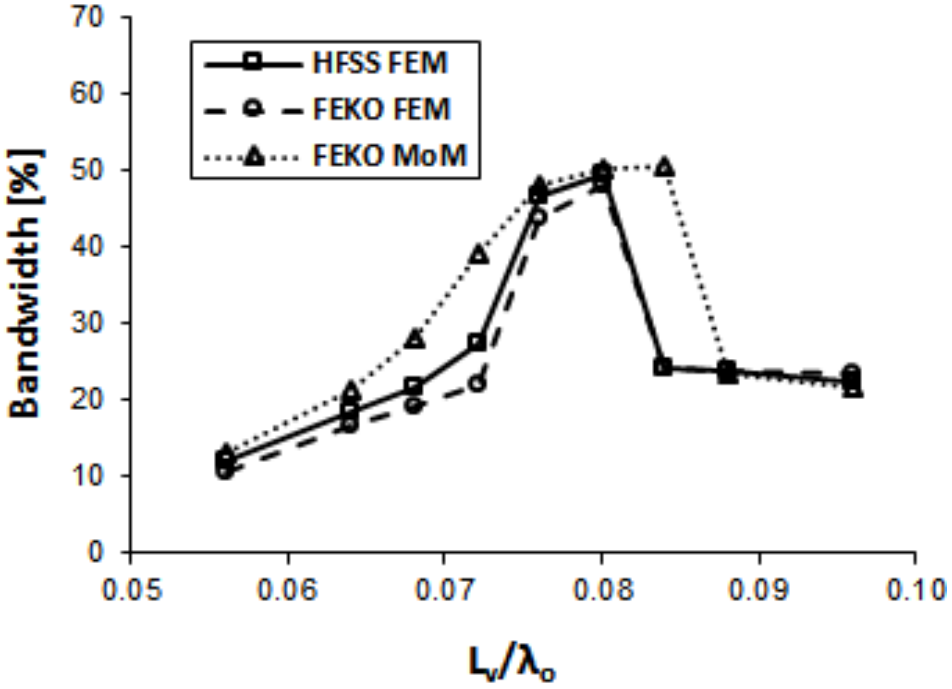

Fig. 2.7. Bandwidth versus L_v/λ_o for $\varepsilon_r = 2.2$ substrate [56] (© 2016 ACES)

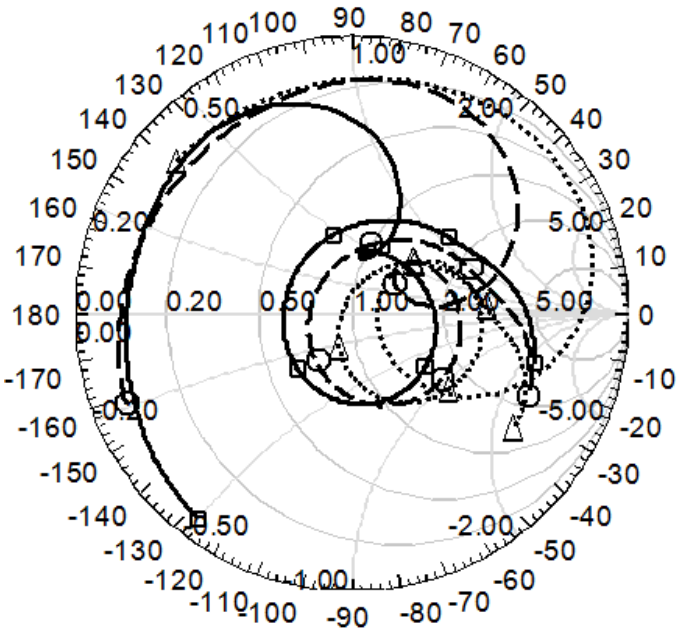

(a)

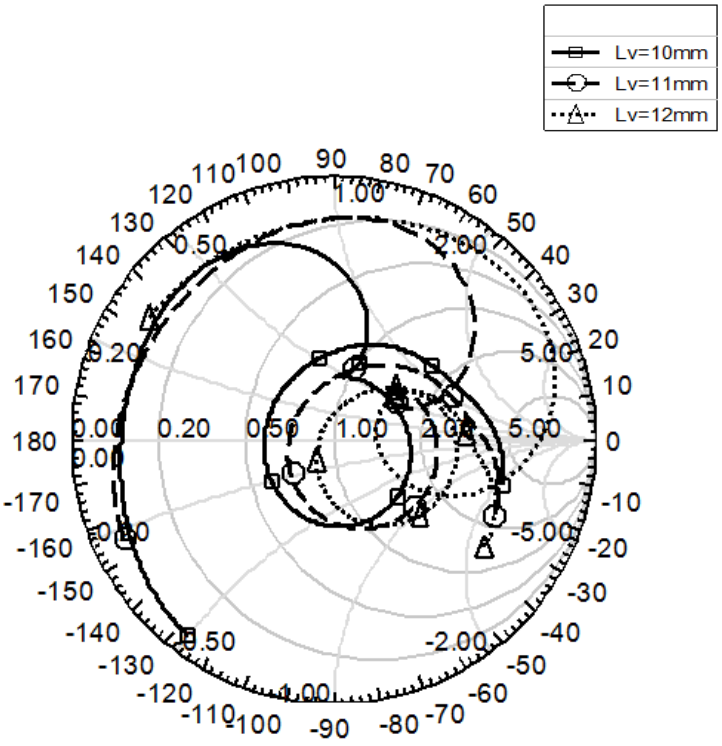

(b)

Fig. 2.8. Smith chart for different L_v and $\varepsilon_r = 2.2$ substrate. (a) HFSS FEM. (b) FEKO FEM

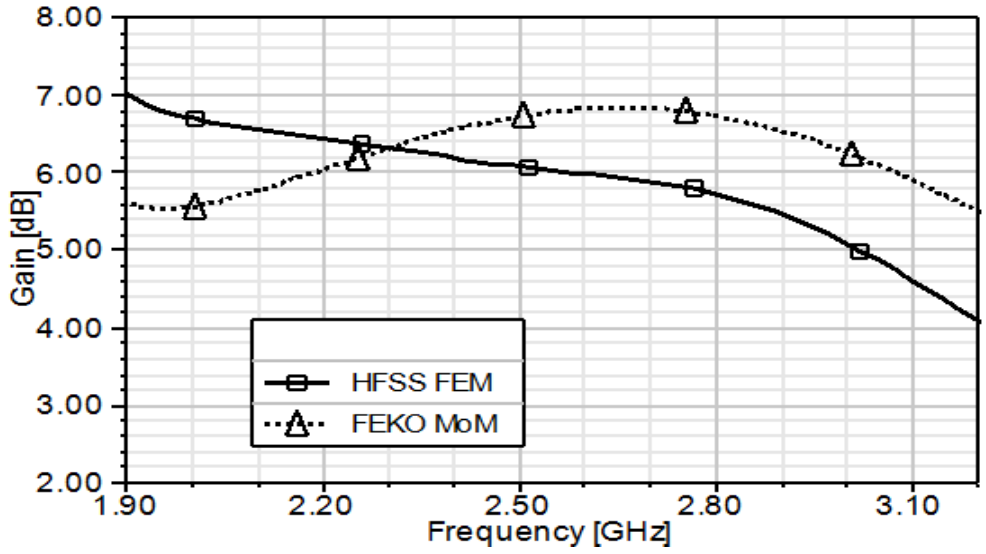

Fig. 2.9. Gain for $L_v = 10$mm, $L_h = 12$mm and $\varepsilon_r = 2.2$ substrate [45] (© 2016 ACES)

2.2.2 For $\varepsilon_r = 4.5$ substrate

The horizontal length, L_h, is varied at 8 different points between 3 and 13mm. L_v is fixed at 10mm. As shown in the Fig. 2.10, a wideband behavior is observed for the L_h values equal to 5mm and 9mm. Figure 2.11 summarizes the relationship between L_h/λ_o (where λ_o is the free-space wavelength corresponding to the 2.4 GHz design frequency) and bandwidth and shows good agreement between the HFSS and FEKO results for L_h = 3-13mm (0.02-0.11λ_o). As shown in Fig. 2.11, optimum bandwidth over 50% is achieved when L_h is equal to 0.02-0.04λ_o.

Figure 2.12 shows the effect of varying the L_h on the input impedance behavior of the U-slot patch antenna in HFSS and FEKO simulations for 1.5-5.0 GHz sweep. As shown in Fig. 2.12, the Smith charts indicate the trend that as L_h decreases from 13mm to 3mm, the impedance loop moves closer to the center locus (VSWR=1) of the Smith chart, indicating the highest wideband impedance behavior.

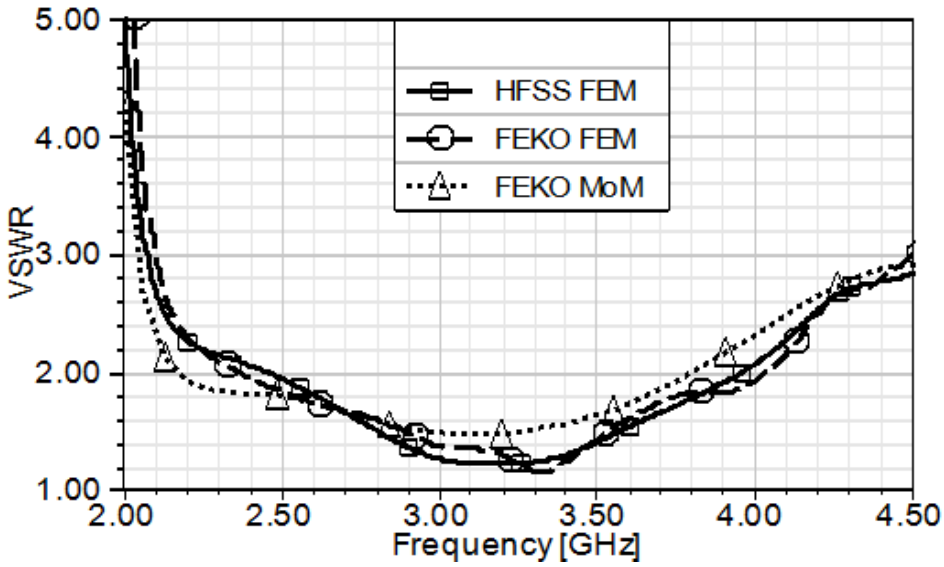

(a)

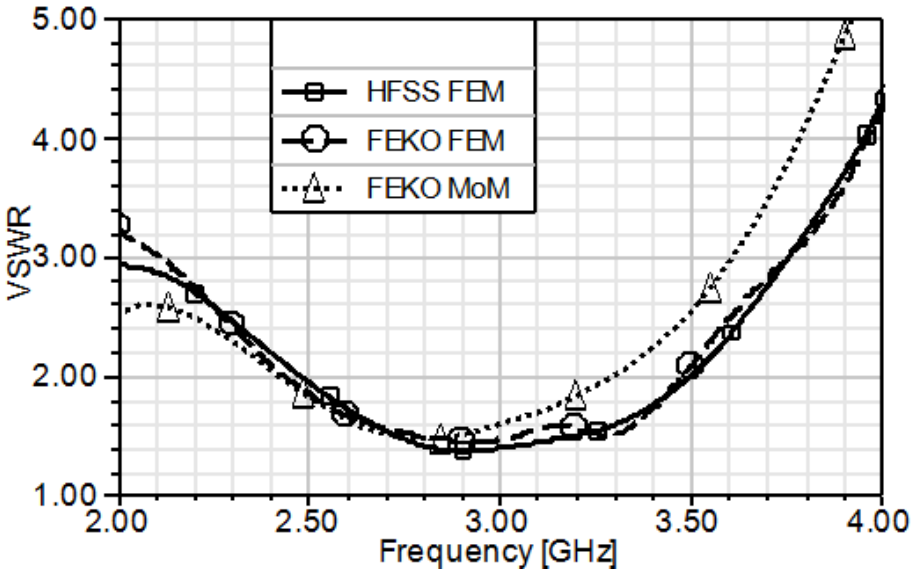

(b)

Fig. 2.10. VSWR for different L_h and $\varepsilon_r = 4.5$ substrate with fixed $L_v = 10$mm. (a) $L_h = 5$mm (b) $L_h = 9$mm [45] (© 2016 ACES)

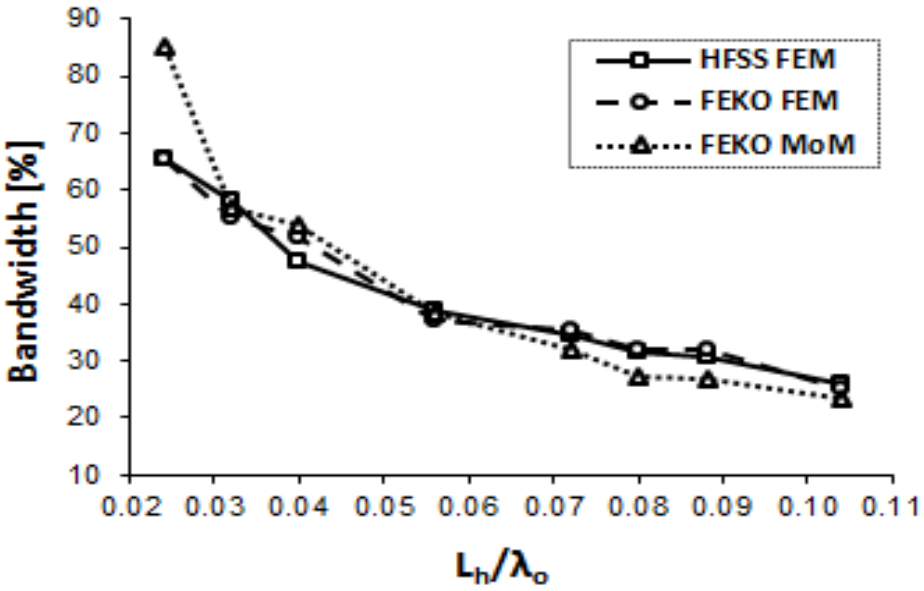

Fig. 2.11. Bandwidth versus L_h/λ_o for $\varepsilon_r = 4.5$ substrate [45] (© 2016 ACES)

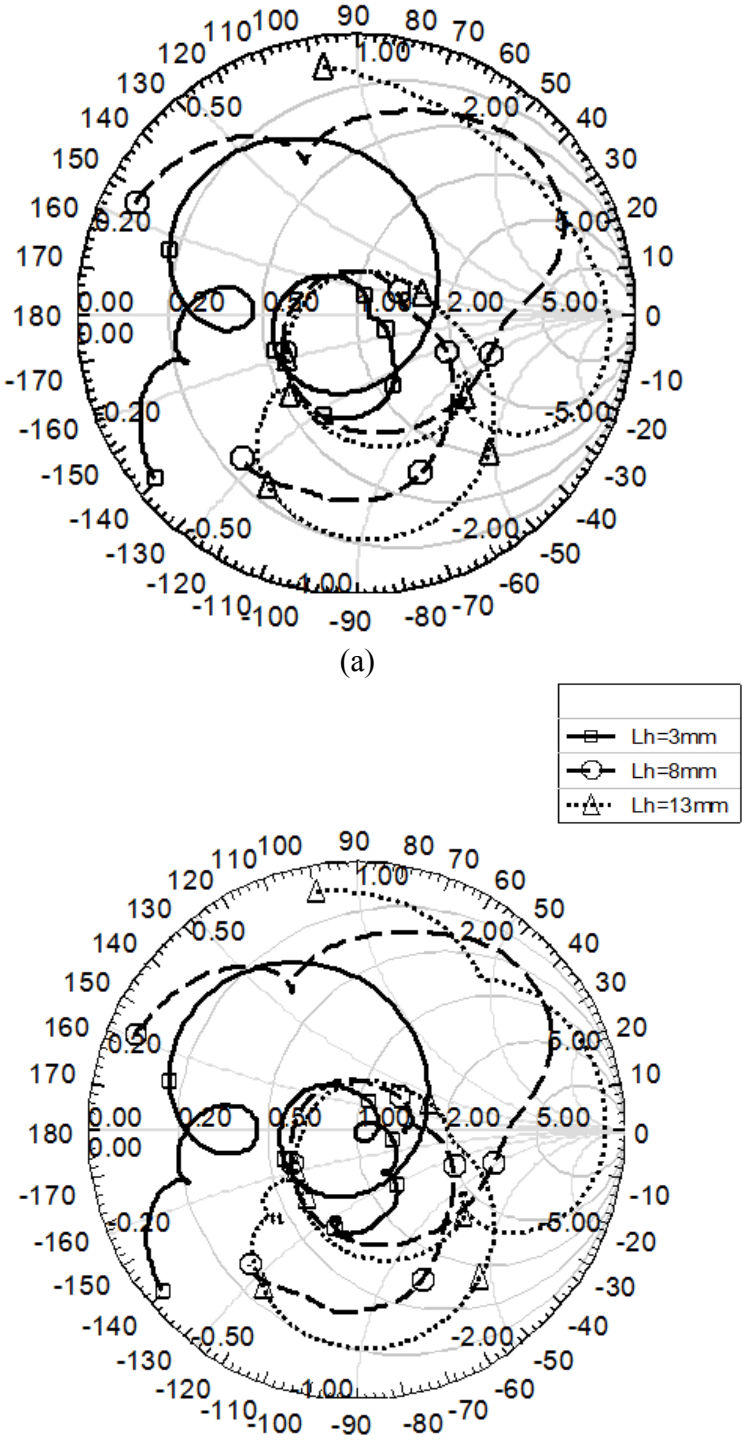

(a)

(b)

Fig. 2.12. Smith chart for different L_h and $\varepsilon_r = 4.5$ substrate. (a) HFSS FEM. (b) FEKO FEM

The vertical length, L_v, is varied at 5 different points between 6 and 10mm. L_h is fixed at 3mm. As shown in Fig. 2.13, the wideband behavior is observed for the L_v values equal to 9mm and 10mm. Figure 2.14 summarizes the relationship between L_v/λ_o and bandwidth and shows good agreement between the HFSS and FEKO results for L_v = 6-10mm (0.05-0.08λ_o). As shown in Fig. 2.14, optimum bandwidth over 50% is achieved when L_v is equal to 0.05-0.08λ_o.

Figure 2.15 shows the effect of varying L_v on the input impedance behavior of the U-slot patch antenna in HFSS and FEKO simulations for 2.0-7.5 GHz sweep at L_v=6mm and 8mm, and for 1.5-5.0 GHz sweep at L_v=10mm. The Smith charts in Fig. 2.15 indicate the trend that as L_v increases, the impedance values move toward the inductive upper half of the Smith chart. The impedance loop of L_v = 10mm, which corresponds to 0.08λ_o, is closest to the center locus (VSWR=1) of the Smith chart, indicating the highest wideband impedance behavior.

The antenna gain for the wideband case of L-probe dimensions L_v = 10mm and L_h = 3mm in HFSS and FEKO simulations is illustrated in Fig. 2.16. As shown in the figure, there is good agreement in the gain between the HFSS and FEKO results. Also, the antenna gain is around 2dB for the 2.2-2.9 GHz (~28%) bandwidth achieved by these L-probe dimensions.

Comparing the results of the ε_r = 2.2 and 4.5 substrates, it is noted that the bandwidth is increased for the ε_r = 4.5, however, the gain is decreased. This is expected since the loss tangent of the ε_r = 4.5 substrate is higher than the loss tangent of the ε_r = 2.2 substrate. This results in more losses in the dielectric substrate, which in turn decreases the input impedance leading to increased bandwidth and decreased efficiency.

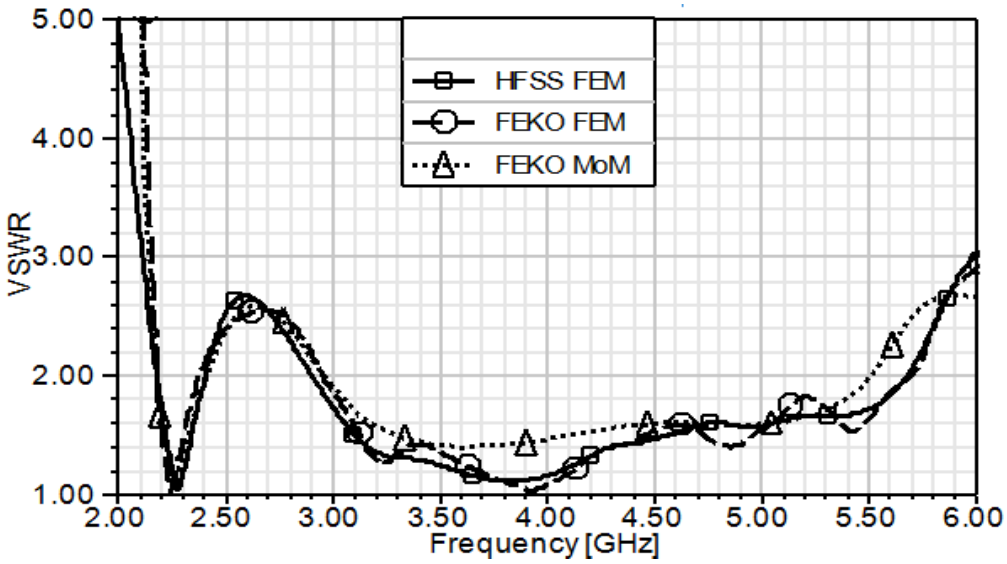

(a)

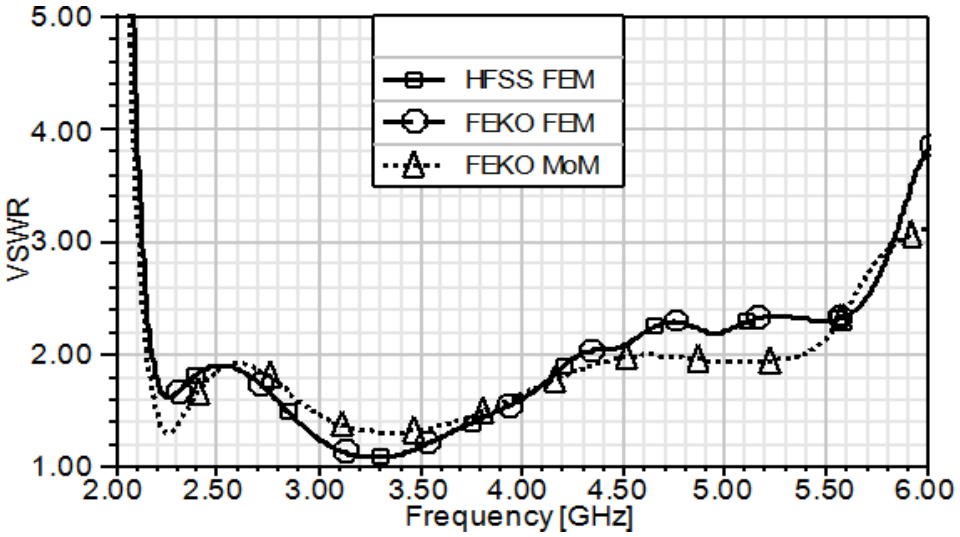

(b)

Fig. 2.13. VSWR for different L_v and $\varepsilon_r = 4.5$ substrate with fixed $L_h = 3$mm. (a) $L_v = 9$mm (b) $L_v = 10$mm [45] (© 2016 ACES)

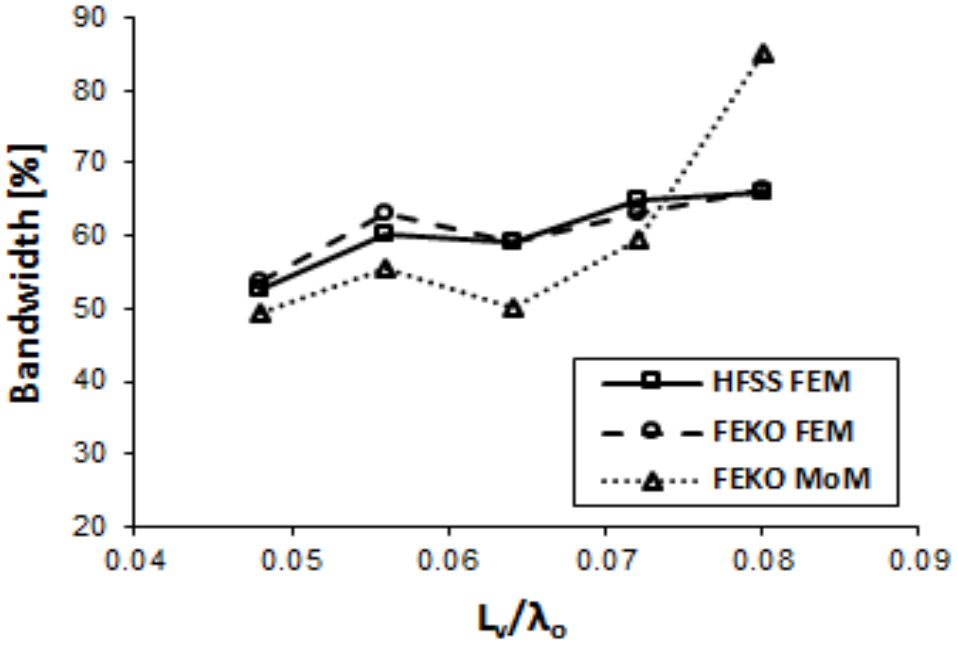

Fig. 2.14. Bandwidth versus L_v/λ_o for $\varepsilon_r = 4.5$ substrate [45] (© 2016 ACES)

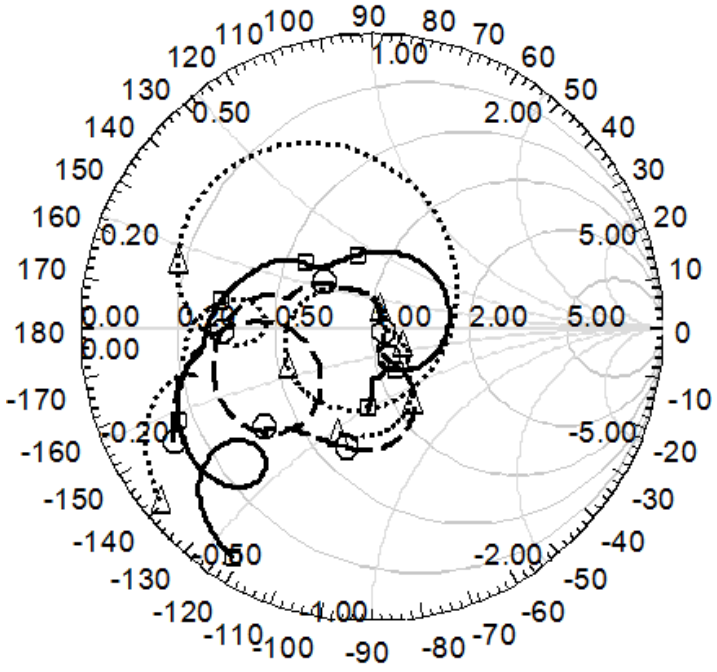

(a)

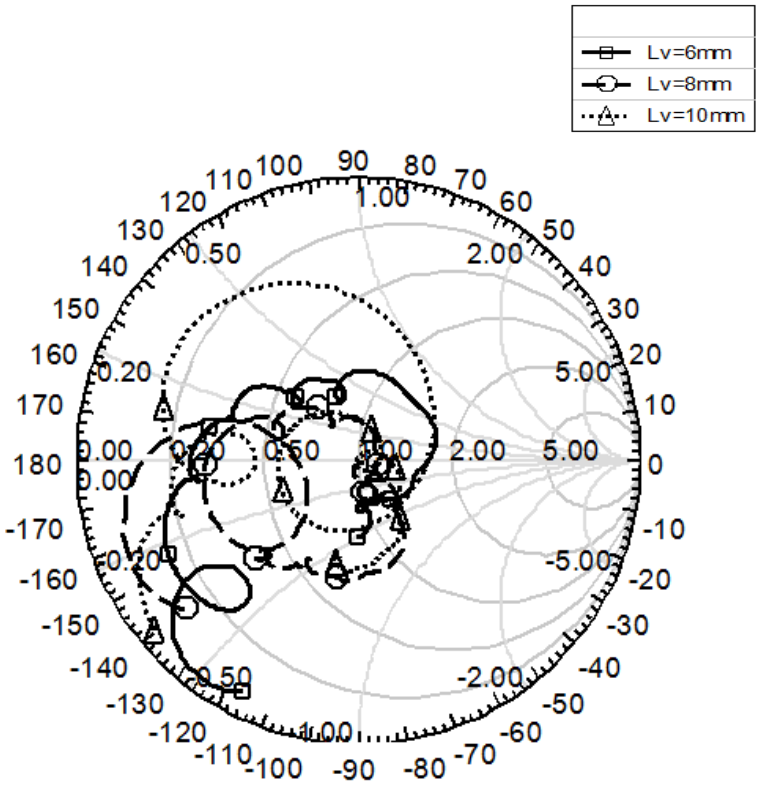

(b)

Fig. 2.15. Smith chart for different L_v and $\varepsilon_r = 4.5$ substrate. (a) HFSS FEM. (b) FEKO FEM

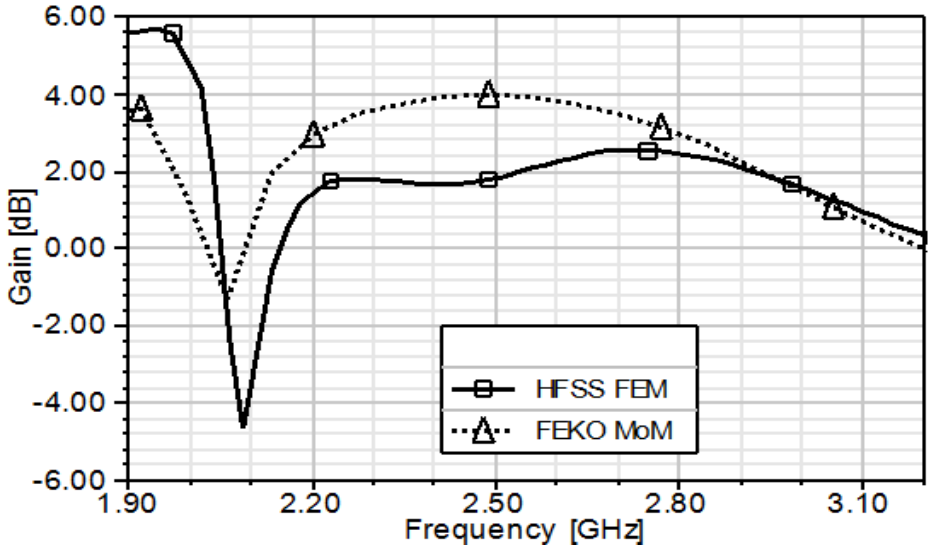

Fig. 2.16. Gain for $L_v = 10$mm, $L_h = 3$mm and $\varepsilon_r = 4.5$ substrate [45] (© 2016 ACES)

2.3 Time Domain Analysis of L-Probe Fed U-slot Patch Antenna

In this section, the wideband, L-probe fed, U-slot patch antenna for $\varepsilon_r = 2.2$ substrate, shown in Fig. 2.3(b), is analyzed in the time domain to evaluate its suitability for UWB pulse applications. Using FEKO MoM solver's post-processing engine, the antenna is excited by the modulated Gaussian pulse defined mathematically in FEKO as [46]:

$$v(t) = \cos(2\pi f_{mod} t)\, e^{\frac{-(t-t0)^2}{T^2}} \tag{2.1}$$

where *fmod* is the pulse modulation frequency set at 2.4 GHz, *t0* is the time shift set at 700 ps, and *T* is the pulse width set at 400 ps. The total signal duration is 6ns and number of samples is 300.

The antenna's fidelity is calculated using MATLAB (see Appendix A.2) and defined as the maximum normalized cross-correlation value of the excitation and radiated signals [47]:

$$F = \max_{\tau} \left| \frac{\int_{-\infty}^{\infty} a(t) r(t+\tau) dt}{\sqrt{\left(\int_{-\infty}^{\infty} a(t)^2 dt\right)\left(\int_{-\infty}^{\infty} r(t)^2 dt\right)}} \right| \tag{2.2}$$

where *a(t)* is the pulse excitation signal, *r(t)* is the radiated pulse for a given θ and ϕ in the far field, and *τ* is the time delay. The Gaussian pulse's time response at θ = 0°/ϕ = 0° in the far field is shown in Fig. 2.17 and the antenna's fidelity in this direction is calculated to equal 0.9154. The antenna's fidelity is calculated for 3 more directions in the far field: θ = 0°/ϕ = 45°, θ = 45°/ϕ = 45°, and θ = 45°/ϕ = 0°. The results are 0.9222, 0.9383, and 0.9349, respectively, which indicate that this L-probe fed U-slot patch antenna design has high fidelity and is suitable for UWB pulse applications.

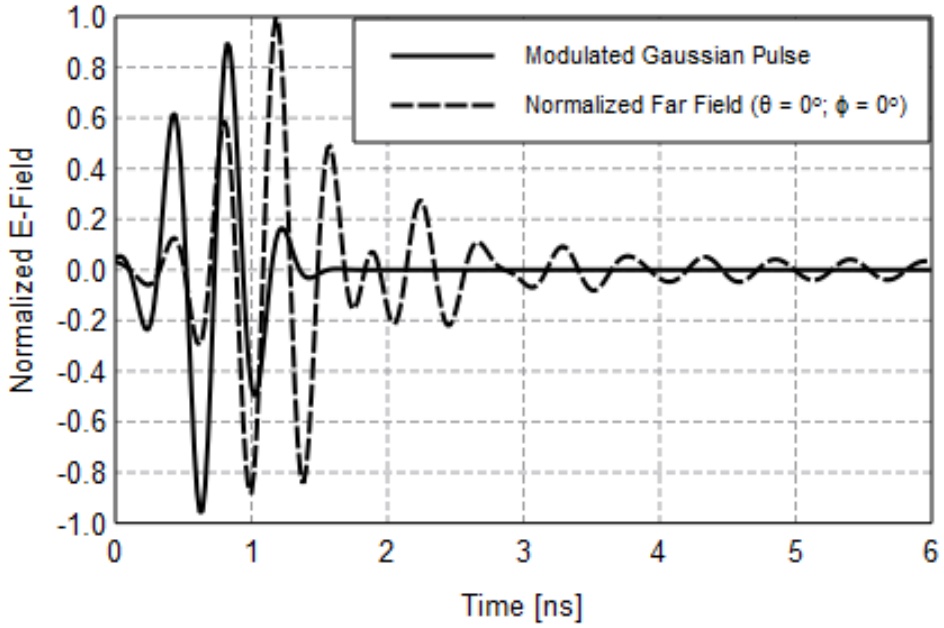

Fig. 2.17. Excitation Gaussian pulse and the radiated time response in the far field

2.4 Empirical Design Technique for L-Probe Feed

In this section, the ideal L-probe dimension information presented in figures 2.4, 2.7, 2.11, and 2.14 is utilized to extrapolate the ideal L-probe dimensions on substrates with different dielectric constants to generate optimum impedance bandwidth. Figure 2.1 shows the U-slot patch antenna geometry and Table 2.3 shows the antenna dimensions for three substrate materials realized using the aforementioned method of dimensional invariance for a 2.4 GHz design frequency. The three substrate materials are: the *Rogers TMM 3* substrate material with $\varepsilon_r = 3.27$ and $\tan(\delta) = 0.002$, the *Rogers TMM 6* substrate material with $\varepsilon_r = 6.0$ and $\tan(\delta) = 0.0023$, and the *Rogers TMM 10* substrate material with $\varepsilon_r = 9.2$ and $\tan(\delta) = 0.0022$. The optimized L-probe position values, x_p and y_p, are shown in parenthesis in Table 2.3, and the optimized vertical probe x_p and y_p values are outside the parenthesis.

Using FEKO MoM, FEKO FEM, and HFSS FEM solvers, the three antennas are simulated with a conventional vertical probe and an L-probe feed. The horizontal length of the L-probe feed for the ε_r = 3.27 substrate is realized by taking the average of the L_h/λ_o value with maximum bandwidth for ε_r = 2.2 substrate in Fig. 2.4 and the L_h/λ_o value with maximum bandwidth for ε_r = 4.5 substrate in Fig. 2.11, which equals to approximately $0.05\lambda_o$ or 6mm. Simulation results using the L_h/λ_o value with maximum bandwidth for ε_r = 2.2 and 4.5, instead of using the average between the two showed bandwidths of 10% and 48%, respectively, compared to over 55% when using the average value. Similarly, the vertical length of the L-probe feed for the ε_r = 3.27 substrate is realized by taking the average of the L_v/λ_o value with maximum bandwidth for ε_r = 2.2 substrate in Fig. 2.7 and the L_v/λ_o value with maximum bandwidth for ε_r = 4.5 substrate in Fig. 2.14, which equals to $0.08\lambda_o$ or 10mm. For the ε_r = 6.0 and 9.2 substrates, the horizontal and vertical lengths of the L-probe feed are realized by taking the L_h/λ_o value with maximum bandwidth for ε_r = 4.5 substrate in Fig. 2.11, which equals to $0.02\lambda_o$ or 2.5mm, and the L_v/λ_o value with maximum bandwidth for ε_r = 4.5 substrate in Fig. 2.14, which equals to $0.08\lambda_o$ or 10mm.

VSWR results in Fig. 2.18(a) show that, for ε_r = 3.27 substrate, using the first-pass L-probe design over the vertical probe, the bandwidth improved from 9% to over 55%. Similarly, VSWR results in Fig. 2.18(b) show that, for ε_r = 6.0 substrate, using the designed L-probe over the vertical probe, the bandwidth improved from 13% to over 60%. VSWR results in Fig. 2.18(c) show that, for ε_r = 9.2 substrate, using the designed L-probe over the vertical probe, the bandwidth improved from 33% to over 53%. FEKO FEM and HFSS FEM results for the L-probe are in agreement in the three plots.

Table 2.3: U-slot microstrip patch antenna dimensions for various substrates [45] (© 2016 ACES)

	ε_r = **3.27**	ε_r = **6.0**	ε_r = **9.2**
a	4.24	3.14	2.44
b	4.24	3.14	2.44
W	38.17	28.18	21.88
L	27.56	20.34	15.8
L_s	19.08	14.06	10.94
t	2.14	1.58	1.22
W_s	14.83	10.95	8.5
r_p	1	1	1
x_p	0 (10.78)	6 (7.17)	4(5.9)
y_p	0 (-2)	-3 (-3)	-5(-5)
d	3	3	3
h	13	12	12

*All values are in mm.

The antenna gain for the ε_r = 3.27, 6.0, and 9.2 substrate design examples is illustrated in Fig. 2.19. As expected, the antenna gain for the low permittivity 3.27 substrate is the highest with around 2-3dB in most of the VSWR $\leq$ 2 bandwidth.

The co- and cross-polar radiation patterns in the ϕ = 0° and ϕ = 90° planes for the ε_r = 3.27 substrate design example are shown in Fig. 2.20. It is observed that cross-polar levels

are lower in the $\phi = 0°$ plane in comparison with the $\phi = 90°$ plane. This is expected and is due to the asymmetric current distribution in the $\phi = 90°$ plane.

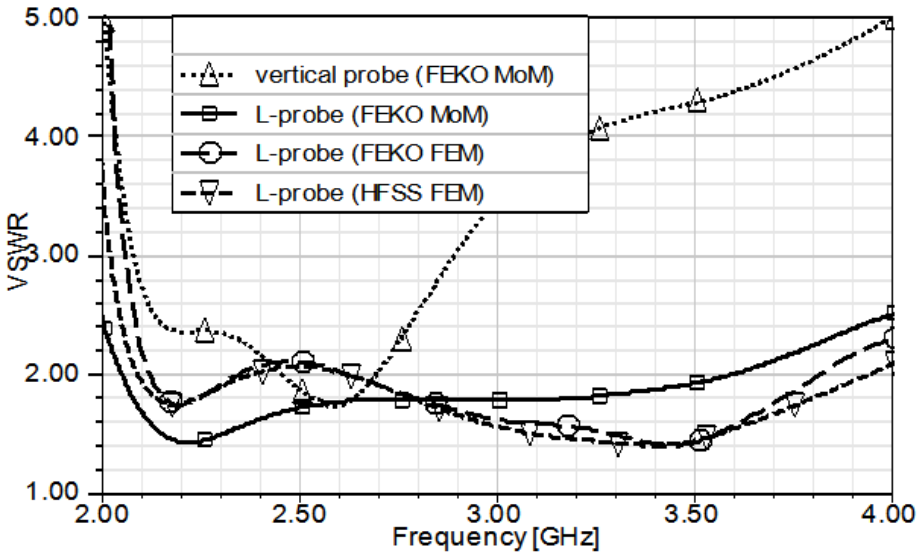

(a)

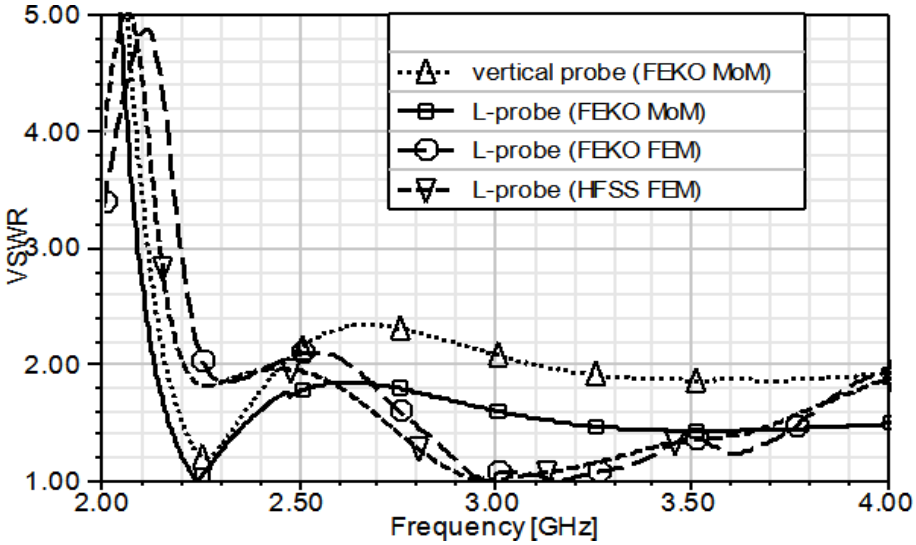

(b)

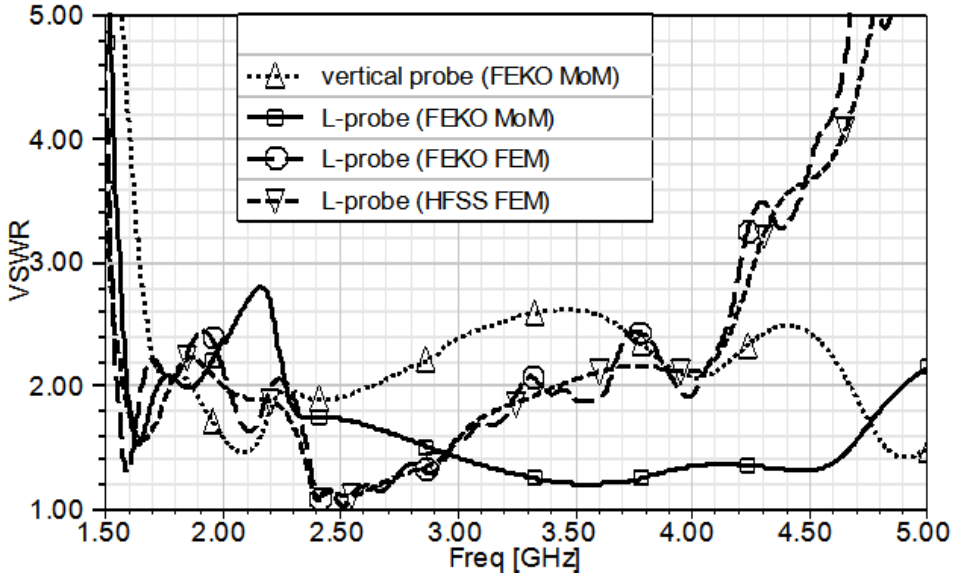

(c)

Fig. 2.18. VSWR with vertical probe and L-probe for substrates (a) $\varepsilon_r = 3.27$ (b) $\varepsilon_r = 6.0$ (c) $\varepsilon_r = 9.2$ [45] (© 2016 ACES)

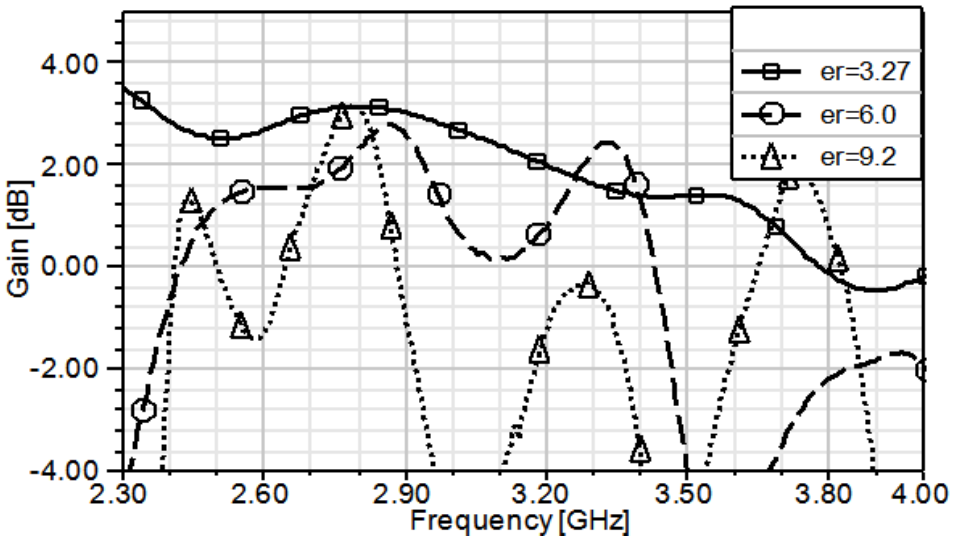

Fig. 2.19. FEKO FEM Gain for $\varepsilon_r = 3.27$, 6.0, and 9.2 substrates [45] (© 2016 ACES)

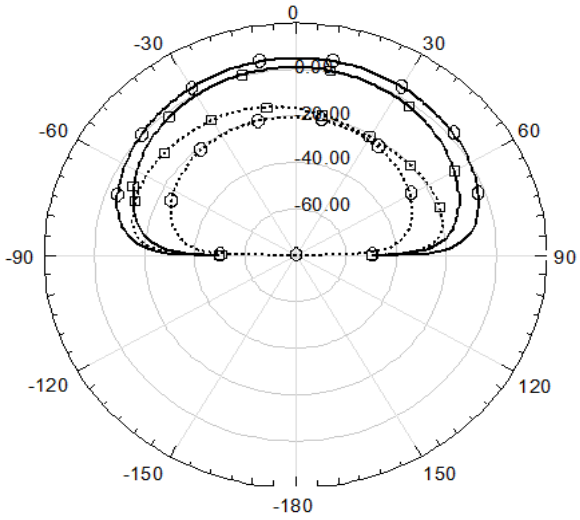

(a)

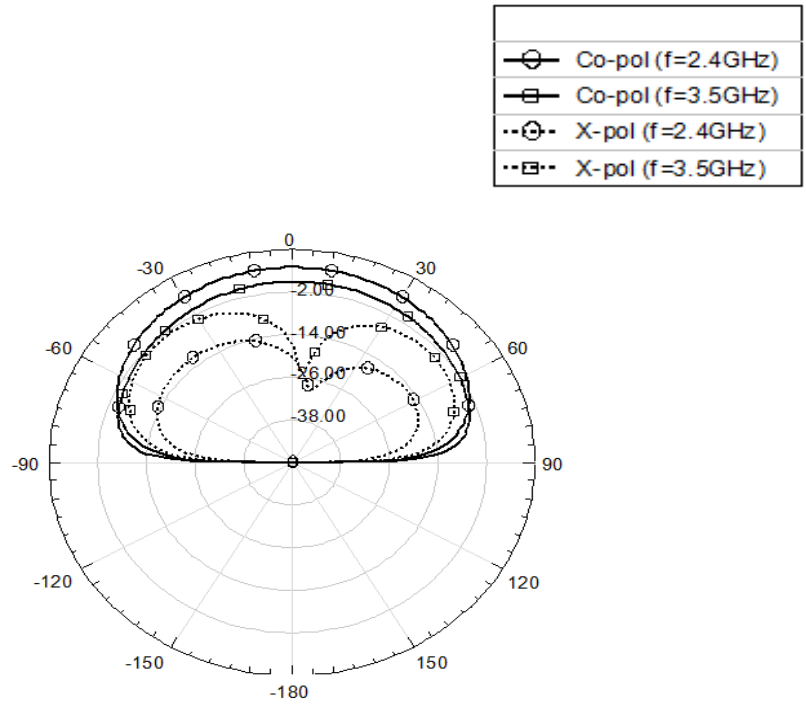

(b)

Fig. 2.20. FEKO MoM Co-polar and cross-polar patterns for the L-probe fed U-slot patch design for $\varepsilon_r = 3.27$ substrate at 2.4 GHz and 3.5 GHz (a) $\phi = 0°$ (b) $\phi = 90°$ [45] (© 2016 ACES)

The empirical design technique for the L-probe feed developed above can be summarized as follows:

(a) For $\varepsilon_r = 2.2$ substrates, use initial first-pass values of $L_h = 0.08\lambda_o$ and $L_v = 0.08\lambda_o$. For further optimization, use values of $0.08\lambda_o \leq L_h \leq 0.11\lambda_o$.

(b) For $2.2 < \varepsilon_r < 4.5$ substrates, use initial first-pass values of $L_h = 0.05\lambda_o$ and $L_v = 0.08\lambda_o$. For further optimization, use values of $0.05\lambda_o \leq L_h \leq 0.08\lambda_o$.

(c) For $4.5 \leq \varepsilon_r \leq 9.2$ substrates, use initial first-pass values of $L_h = 0.02\lambda_o$ and $L_v = 0.08\lambda_o$. For further optimization, use values of $0.02\lambda_o \leq L_h \leq 0.04\lambda_o$ and $0.05\lambda_o \leq L_v \leq 0.08\lambda_o$.

The design procedure assumes the substrate height, h, is greater than the vertical length of the L-probe, L_v, namely $0.10\lambda_o \leq h \leq 0.12\lambda_o$. Also, the design procedure assumes the probe diameter, $2r_p$, is less than the horizontal length of the L-probe, L_h, otherwise further optimization to either probe diameter or L_h is needed. The design procedure is applicable for $\varepsilon_r = 2.2$-9.2 substrates only.

2.5 Summary

In this chapter, an initial, low-profile, wideband U-slot patch design is realized using the method of dimensional invariance. Ideal L-probe feed dimensions are established through extensive parametric study on $\varepsilon_r = 2.2$ and 4.5 substrates to propose empirical guidelines for the design of L-probe feeds which yield first-pass optimum impedance bandwidth. The established ideal L-probe dimensions, after further extrapolation, are used

successfully on other substrates, ε_r = 3.27, 6.0 and 9.2, for the design of first-pass L-probe feeds which yield impedance bandwidth over 55%, 60%, and 53%, respectively.

Results show good agreement between the three EM solvers. FEKO FEM and HFSS FEM results, in particular, show closer agreement. This is to be expected since the same geometry and underlying computational electromagnetic method are used in the two solvers.

CHAPTER 3

MUTUAL COUPLING CHARACTERIZATION OF UWB U-SLOT ANTENNA ARRAY

UWB scanning phased arrays are finding increasing use in wireless communication and medical applications [48-50]. Scan blindness due to surface wave excitations could reduce the scan bandwidth range [29]. By reducing the mutual coupling between array elements, the scan blindness effects will be reduced [29]. In this chapter, the mutual coupling of a UWB U-slot microstrip patch 2-element array is investigated to find the patch orientation and U-slot topology with the least mutual coupling.

Research work on mutual coupling between microstrip patch antenna arrays is found in the literature [51-54]. Previous work [43, 55] analyzed the mutual coupling between the U-slot microstrip array elements using the vertical probe feeding structure. The study in [56] aimed to characterize the mutual coupling of a U-slot microstrip 2-element array for the L-probe feeding structure compared to the vertical probe feeding structure using different U-slot topologies for $\varepsilon_r = 2.2$ substrate. This chapter aims to characterize the mutual coupling of an L-probe-fed U-slot microstrip 2-element array using different patch orientations and U-slot topologies for $\varepsilon_r = 2.2$ substrate.

3.1 Geometry of a 2-Element U-slot Microstrip Array

The U-slot microstrip patch antenna array is simulated and analyzed using the FEKO MoM solver and validated by the HFSS FEM solver. The simulated U-slot microstrip patch antenna geometry is shown in Fig. 2.1. The RT/Duroid 5880 substrate material with $\varepsilon_r = 2.2$ and $\tan(\delta) = 0.0009$ is used. The method of dimensional invariance described in [41] is used to realize the U-slot antenna patch dimensions, shown in Table 3.1, for a 2.4 GHz design

frequency. Experimental validation of the method of dimensional invariance is reported in [43].

Several simulation optimization runs were performed to arrive at the substrate height and probe position which yield best bandwidth. In FEKO, infinite substrate and ground is assumed. In HFSS, the substrate and ground (W_g and L_g) dimensions are extended by $\lambda/2$, where λ corresponds to lower bandwidth frequency, from the edge of the patch to simulate an infinite substrate and ground. In HFSS, a radiation air box boundary which is $\lambda/2$, where λ corresponds to the lower bandwidth frequency, above the patch is used. A 50-ohm coaxial feed line is used to feed the L-probe. The different 2-element patch orientations and U-slot topologies simulated are shown in Fig. 3.1. The inter-element spacing between the patch edges is taken to be approximately $\lambda/4$. For the diamond patch orientations, the patches are rotated by 45°.

Table 3.1: U-slot microstrip patch antenna dimensions [57] (© 2016 ACES)

a	5.17 mm	**W_s**	18.09 mm
b	5.17 mm	**r_p**	1 mm
W	46.53 mm	**x_p**	13.8 mm
L	33.6 mm	**y_p**	-1 mm
t	2.6 mm	**L_v**	10 mm
d	3 mm	**L_h**	12 mm
h	14 mm		

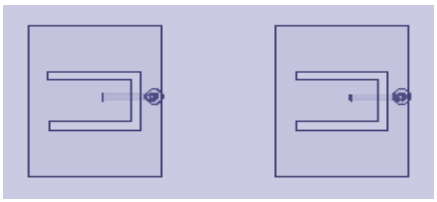

(a)

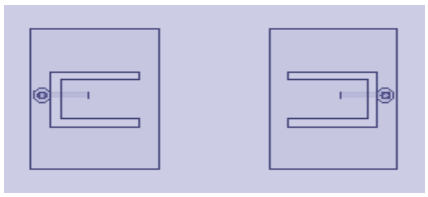

(b)

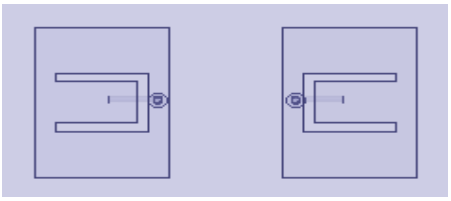

(c)

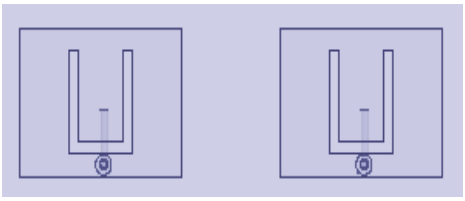

(d)

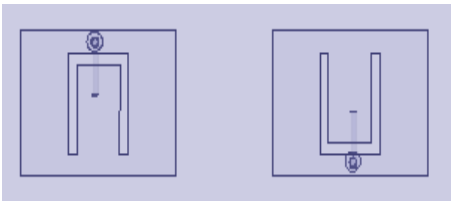

(e)

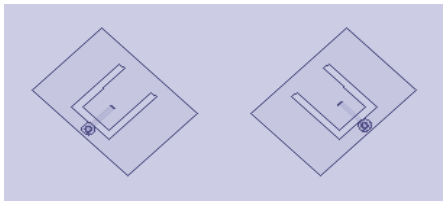

(f)

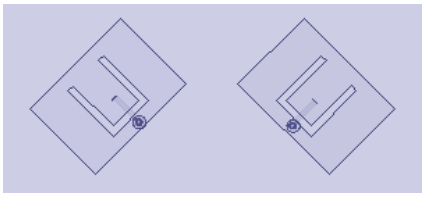

(g)

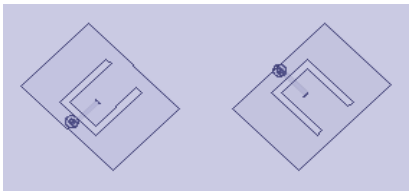

(h)

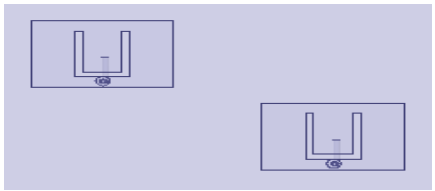

(i)

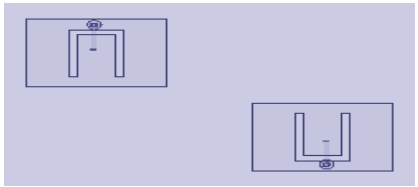

(j)

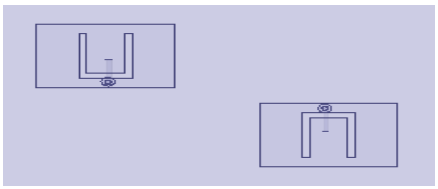

(k)

Fig. 3.1. Variations of U-slot topologies and patch orientations in a 2-element array. (a-c) E-plane patch orientation. (d-e) H-plane patch orientation. (f-h) Diamond patch orientation. (i-k) Diagonal patch orientation [57] (© 2016 ACES)

3.2 Mutual Coupling of a 2-Element U-slot Microstrip Array

3.2.1 For $\varepsilon_r = 2.2$ substrate

In [45], the bandwidth for a single-element L-probe-fed U-slot microstrip patch antenna with $\varepsilon_r = 2.2$ substrate was found to be between 1.8GHz and 3GHz. Figure 3.2(a) shows the E-plane coupling between two L-probe-fed U-slot patch elements for 3 different U-slot topologies over the 2-3GHz bandwidth. HFSS and FEKO simulation results indicate that topology (a) has the lowest mutual coupling in the 20-27dB range, and topology (c) has the highest mutual coupling. Figure 3.2(b) shows the H-plane coupling between two L-probe-fed U-slot patch elements for 2 different U-slot topologies. Results indicate that topology (e) has the lowest mutual coupling in the 20-25dB range. Figure 3.2(c) shows the diamond patch orientation coupling between two L-probe-fed U-slot patch elements for 3 different U-slot topologies. Results indicate that the opposite U-slot topology (h) has the lowest mutual coupling in the 25-45dB range, and topology (g) has the highest mutual coupling. Figure 3.2(d) shows the diagonal patch orientation coupling between two L-probe-fed U-slot patch elements for 3 different U-slot topologies. Results indicate that no

particular topology has the highest or lowest mutual coupling throughout the entire bandwidth, however, topology (j) has the lowest mutual coupling in half of the bandwidth in the 20-40dB range. HFSS and FEKO results show good agreement in Fig. 3.2.

Figures 3.3 and 3.4 show the current density distribution at 2.4 GHz for the U-slot topology (h) with the least mutual coupling and the U-slot topology (c) with the highest mutual coupling, respectively. As shown in both figures more current density is concentrated around the base side of the U-slot, underneath which the L-probe feed is located. In Fig. 3.3, the two U-slot bases are farther apart from each other than in Fig. 3.4. This explains the lower mutual coupling in U-slot topology (h). Similarly, it is observed in the H-plane patch orientation that the U-slot topology (e) has less mutual coupling than U-slot topology (d) mainly because the U-slot base sides, where more current density is present, are farther apart in the case of U-slot topology (e). Also, in the diamond patch orientation, the U-slot topology (g) has the highest mutual coupling because the two U-slot base sides are closest to each other.

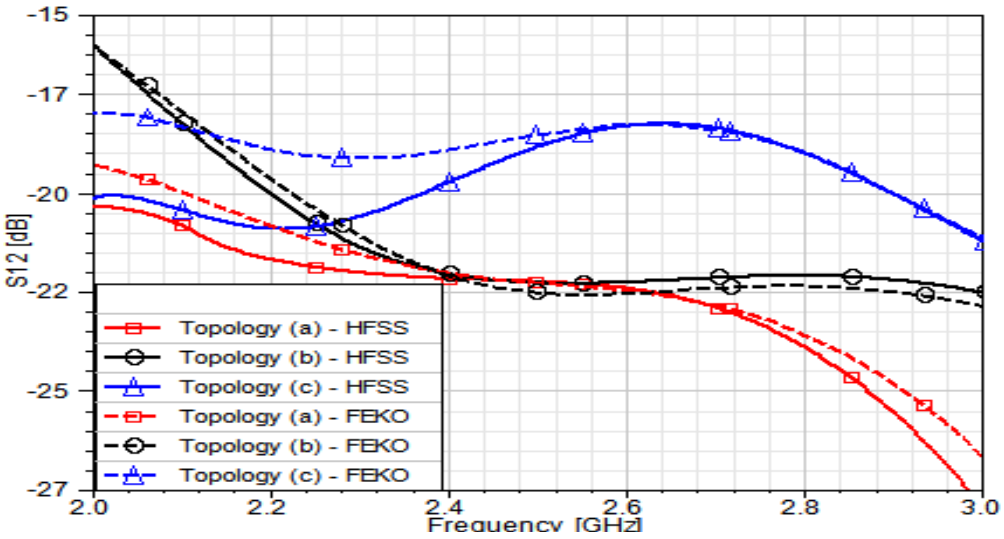

(a)

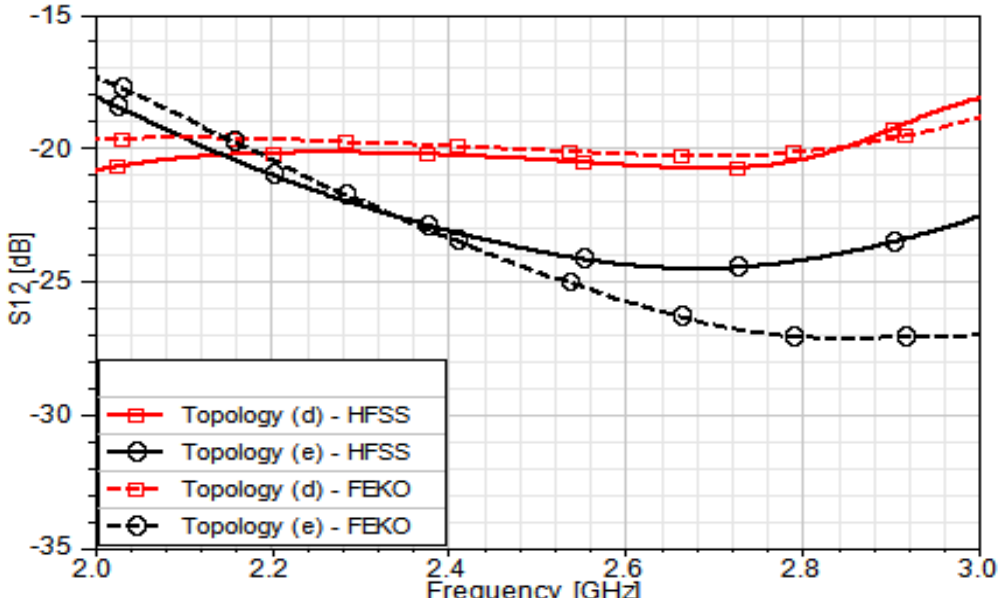
-15
-20
-25
-30
-35
S12 [dB]
2.0
2.2
2.4
2.6
2.8
3.0
Frequency [GHz]
Topology (d) - HFSS
Topology (e) - HFSS
Topology (d) - FEKO
Topology (e) - FEKO

(b)

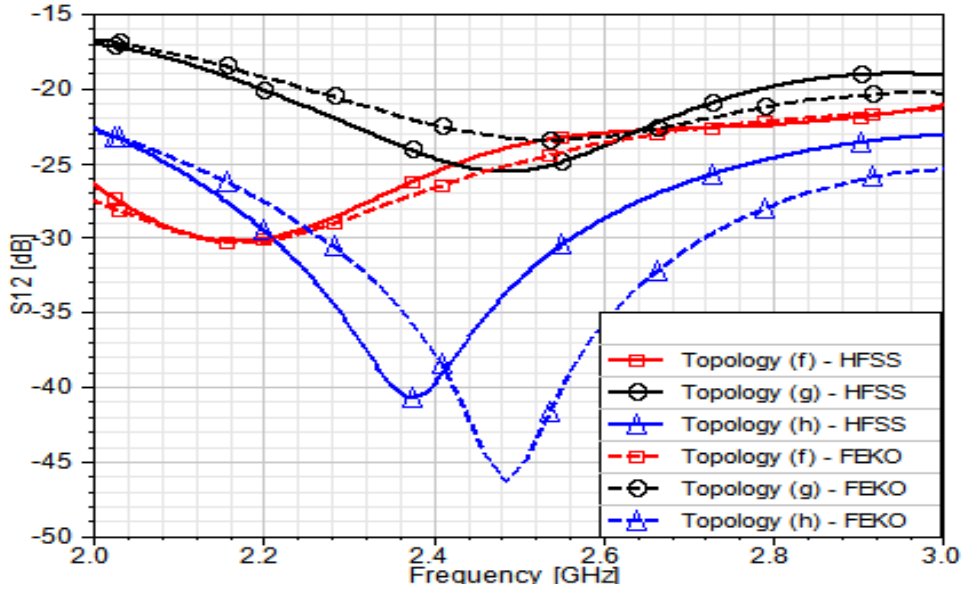
-15
-20
-25
-30
-35
-40
-45
-50
S12 [dB]
2.0
2.2
2.4
2.6
2.8
3.0
Frequency [GHz]
Topology (f) - HFSS
Topology (g) - HFSS
Topology (h) - HFSS
Topology (f) - FEKO
Topology (g) - FEKO
Topology (h) - FEKO

(c)

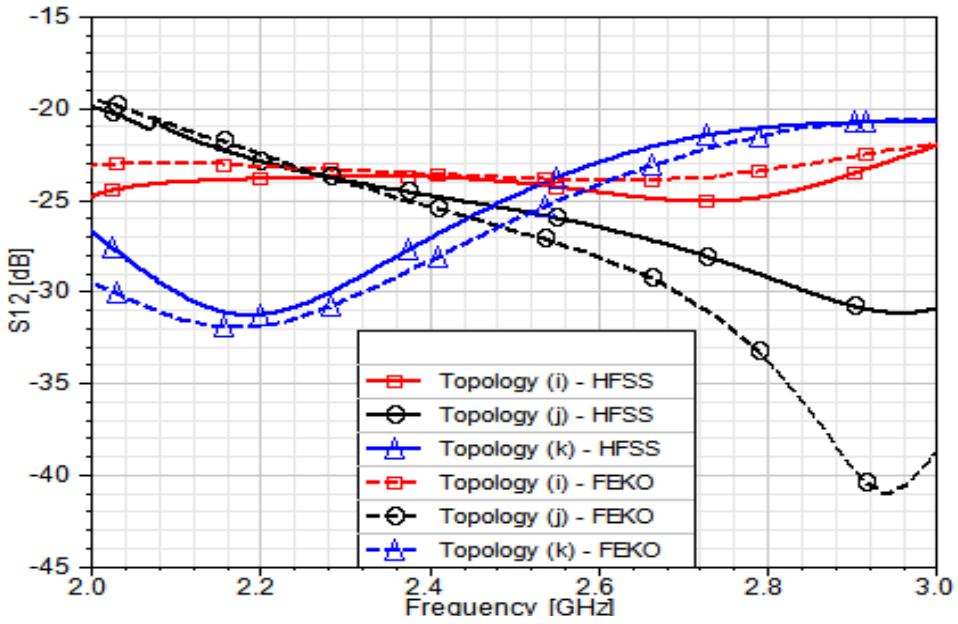

(d)

Fig. 3.2. Mutual Coupling for different U-slot topologies and patch orientations and $\varepsilon_r = 2.2$ substrate. (a) E-plane patch orientation (b) H-plane patch orientation (c) Diamond patch orientation (d) Diagonal patch orientation [57] (© 2016 ACES)

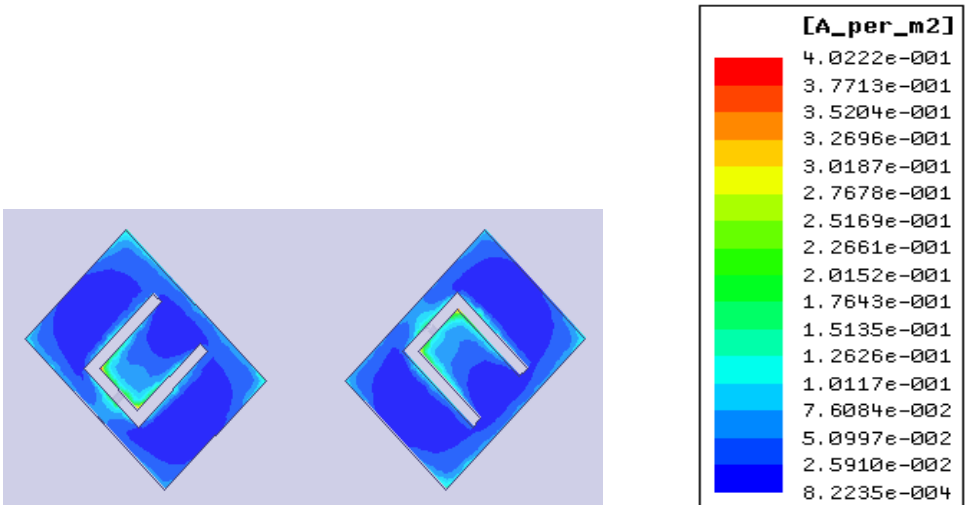

Fig. 3.3. Current density distribution in Diamond patch orientation for U-slot topology (h) at 2.4 GHz [57] (© 2016 ACES)

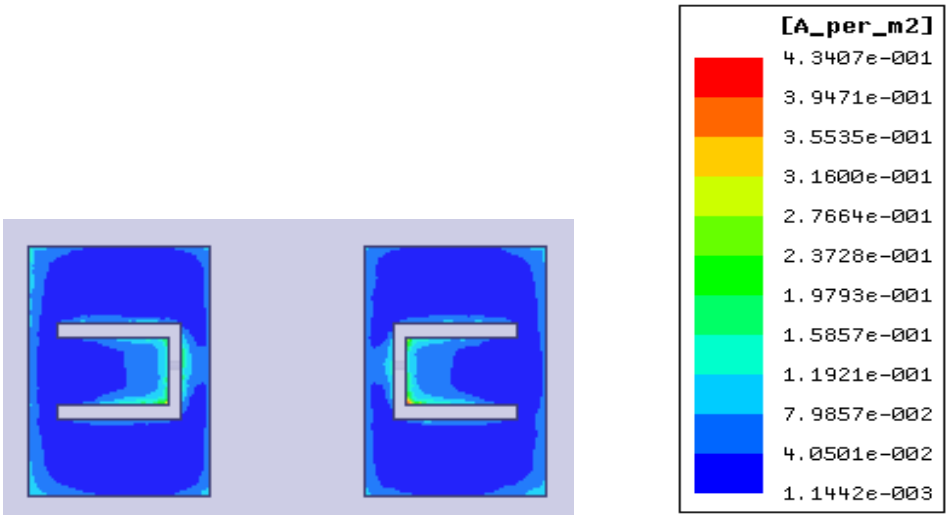

Fig. 3.4. Current density distribution in E-plane patch orientation for U-slot topology (c) at 2.4 GHz [57] (© 2016 ACES)

3.2.2 For ε_r = 4.5 substrate

In [45], the bandwidth for a L-probe-fed U-slot microstrip antenna with ε_r = 4.5 substrate was found to be ~ 2.5-4.5 GHz. Figure 3.5(a) shows the E-plane patch orientation coupling between two L-probe-fed U-slot patch elements for 3 different U-slot topologies. Similar to ε_r = 2.2 substrate, HFSS and FEKO simulation results indicate that topology (a) has the lowest mutual coupling and topology (c) has the highest mutual coupling. Figure 3.5(b) shows the H-plane patch orientation coupling between two L-probe-fed U-slot patch elements for 2 different U-slot topologies. Similar to ε_r = 2.2 substrate, results indicate that topology (e) has less mutual coupling than topology (d). Figure 3.5(c) shows the diamond patch orientation coupling between two L-probe-fed U-slot patch elements for 3 different U-slot topologies. Similar to ε_r = 2.2 substrate, results indicate that topology (h) has the lowest mutual coupling and topology (f) has the highest mutual coupling. Figure 3.5(d) shows the

diagonal patch orientation coupling between two L-probe-fed U-slot patch elements for 3 different U-slot topologies. Results indicate that through most of the bandwidth, topology (j) has the lowest mutual coupling. HFSS and FEKO results show good agreement in Fig. 3.5.

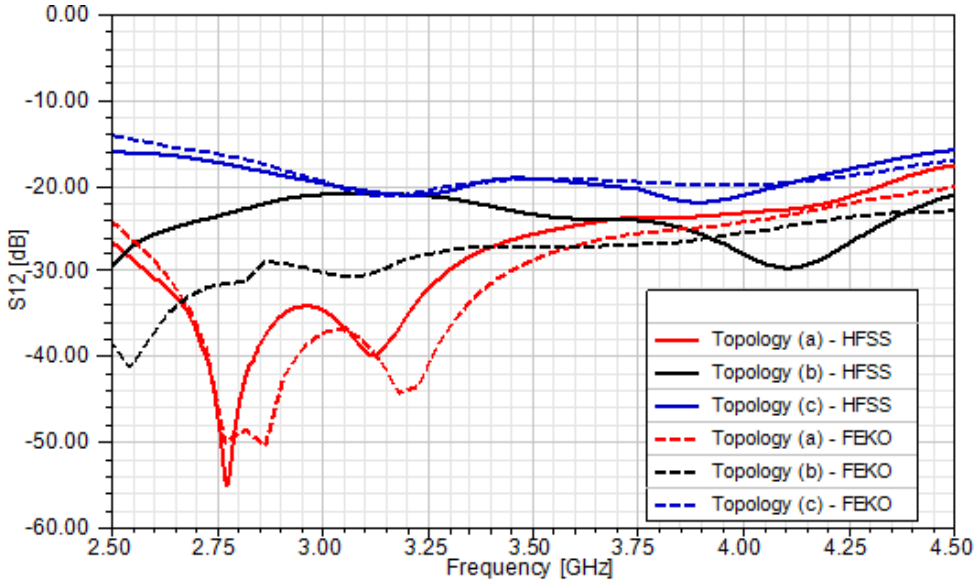

(a)

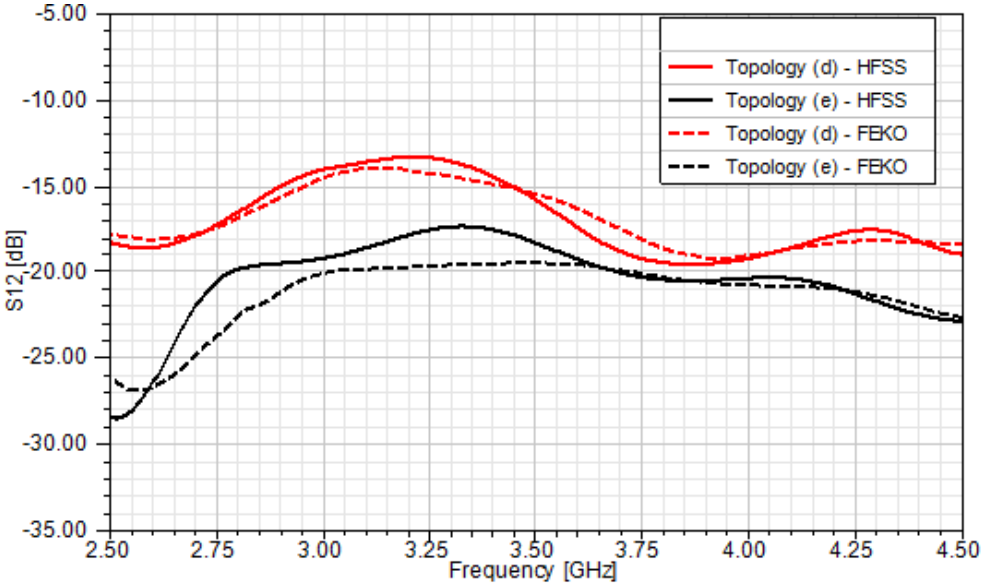

(b)

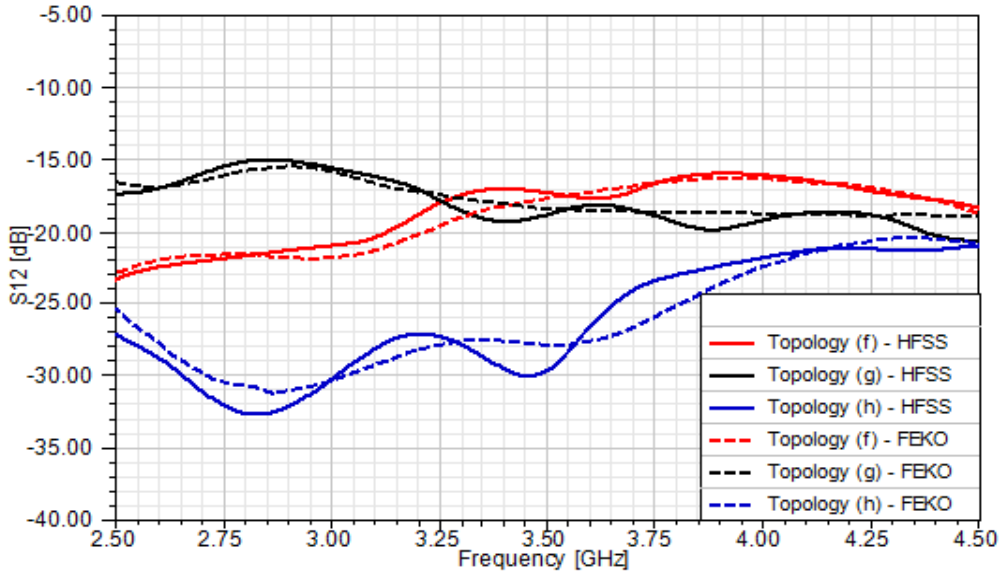

(c)

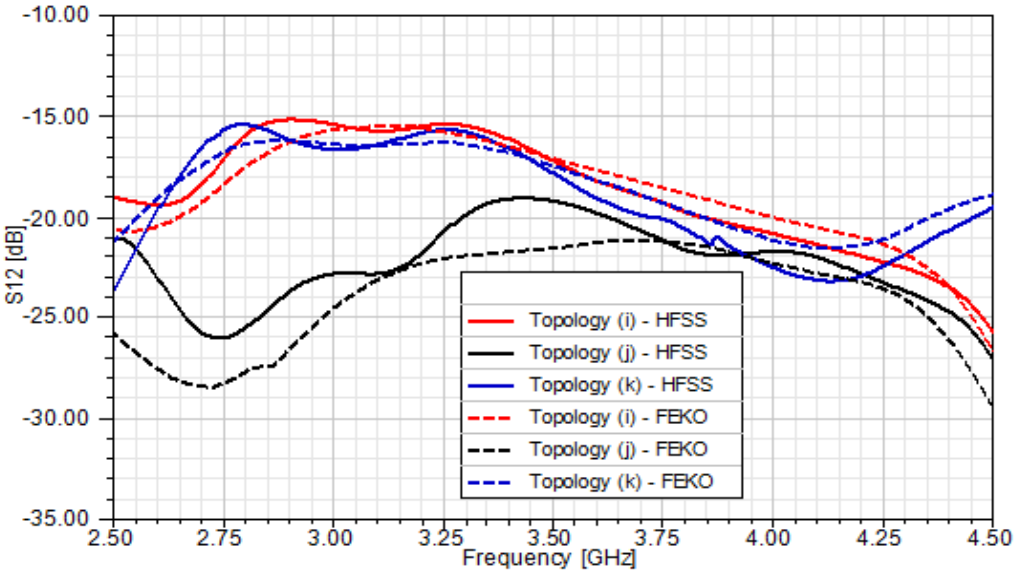

(d)

Fig. 3.5. Mutual Coupling for different U-slot topologies and patch orientations and $\varepsilon_r = 4.5$ substrate. (a) E-plane patch orientation (b) H-plane patch orientation (c) Diamond patch orientation (d) Diagonal patch orientation

3.3 Summary

In this chapter, the evaluation of the mutual coupling of an L-probe-fed U-slot microstrip patch 2-element array using different patch orientations and U-slot topologies for ε_r = 2.2 and 4.5 substrates is presented. HFSS and FEKO simulation results show good agreement and indicate that the current density distribution on the microstrip patch has an effect on mutual coupling between the array elements.

Results also indicate that, for ε_r = 2.2 substrate, the diamond patch orientation with U-slot topology (h) has the least coupling between the array elements, and for ε_r = 4.5 substrate, the E-plane patch orientation with U-slot topology (a) has the least coupling.

CHAPTER 4

SCAN BEHAVIOR OF MICROSTRIP PHASED ARRAY ANTENNAS

UWB scanning phased arrays [58, 59] can be found in wireless communication and medical applications [48-50]. Scan blindness due to surface wave excitations could reduce the scan bandwidth range. By reducing the mutual coupling between array elements, the scan blindness effects will be reduced [29]. In this chapter, the scan element pattern of a 5x5 planar phased array using the diamond patch orientation with least mutual coupling and E-plane patch orientations with highest mutual coupling found in chapter 3 is examined.

Also, the presence of sidelobes and grating lobes can greatly degrade the phased array's performance and power efficiency. Significant research [60-63] has been dedicated to reduce the sidelobe levels and minimize the effect of grating lobes in phased arrays. In this chapter, the effect of nonuniform excitation and inter-element spacing on the sidelobe reduction of a wideband U-slot microstrip patch phased arrays is examined.

4.1 Scan Element Pattern of a Planar Microstrip Phased Array Antenna with Different Patch Orientations and U-slot Topologies

The objective of this section is to characterize the scan element pattern of a 5x5 planar phased array on ε_r = 2.2 substrate using the diamond patch and E-plane patch orientations in chapter 3. The U-slot microstrip patch antenna design and geometry is described in chapter 3. For the E-plane patch orientation, the inter-element spacing between the patch edges is taken to be ~$\lambda/4$ (where λ corresponds to the 2.4 GHz design frequency). For the diamond patch orientation, the patches are rotated by 45° and the inter-element spacing is ~$\lambda/7$ between the patch corners.

The 5x5 U-slot microstrip patch antenna array shown in Fig. 4.1 models the diamond patch orientation in U-slot topology (h) in Fig. 3.1, which shows the lowest mutual coupling. In Fig. 4.2, the VSWR bandwidth of the isolated U-slot element is compared with the VSWR bandwidth of the center elements in the array, namely 3, 8, and 13. The VSWR bandwidth of each of the elements is calculated by exciting only one element and loading all the other elements. Figure 4.2 shows good agreement between the VSWR bandwidth of the isolated element and elements 3, 8, and 13 in the frequency range of 2-3 GHz indicating that adjacent elements do not impact the VSWR result in the bandwidth of interest.

Figures 4.3 (a) and (b) show the scan element patterns at different frequencies within the 2-3 GHz bandwidth for element 3 at $\varphi=0°$ and $\varphi=90°$, respectively. As shown in both figures, no significant blind spots, where gain drops to zero, are observed as the array scans away from broadside. It is acceptable for gain to drop to zero at the higher scanning angles because impedance mismatch increases as the array is scanned away from broadside.

Figures 4.4 (a) and (b) show the scan element patterns at different frequencies for element 8 at $\varphi=0°$ and $\varphi=90°$, respectively. As shown in both figures, no significant blind spots are observed as the array scans away from broadside. Figures 4.5 (a) and (b) show the scan element patterns at different frequencies for element 13 at $\varphi=0°$ and $\varphi=90°$, respectively. As shown in Fig. 4.5 (a), blind spots are observed at scan angles 35° and 55° marked by dotted black circles. No significant blind spots are observed in Fig. 4.5 (b) as the array scans away from broadside.

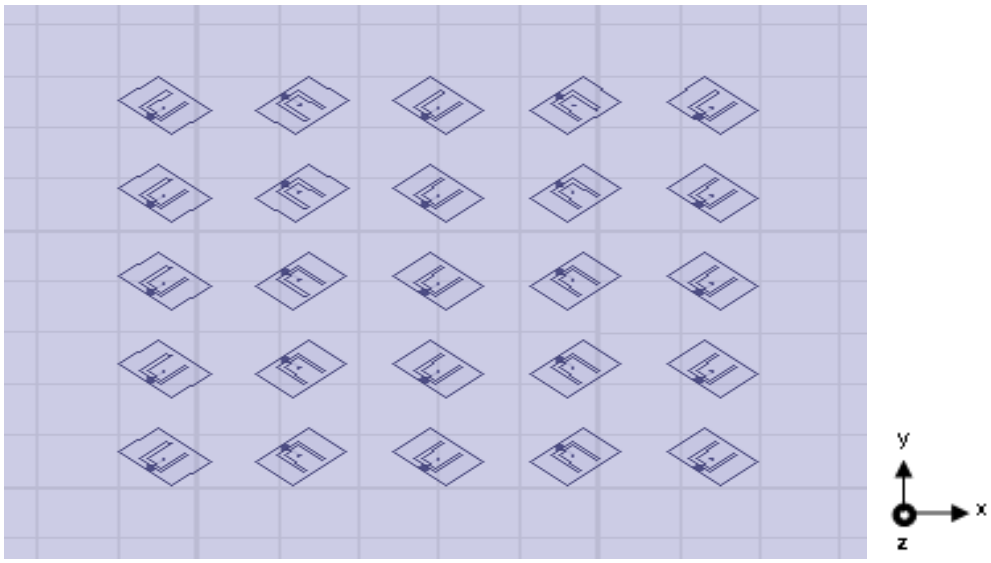

Fig. 4.1. 5x5 U-slot array with Diamond patch orientation [64] (© 2014 IEEE)

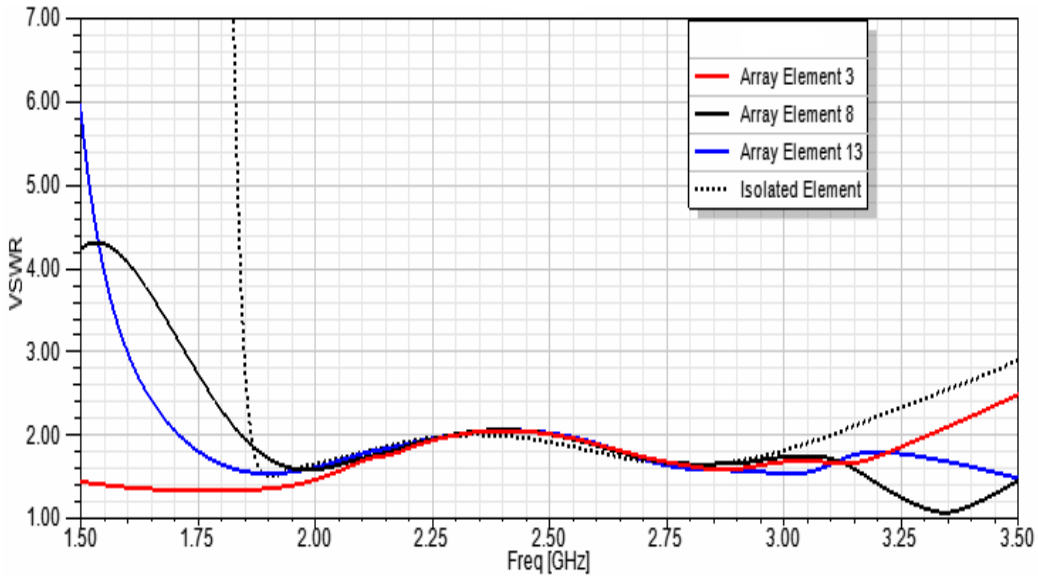

Fig. 4.2. VSWR for selected elements in 5x5 U-slot array with Diamond patch orientation

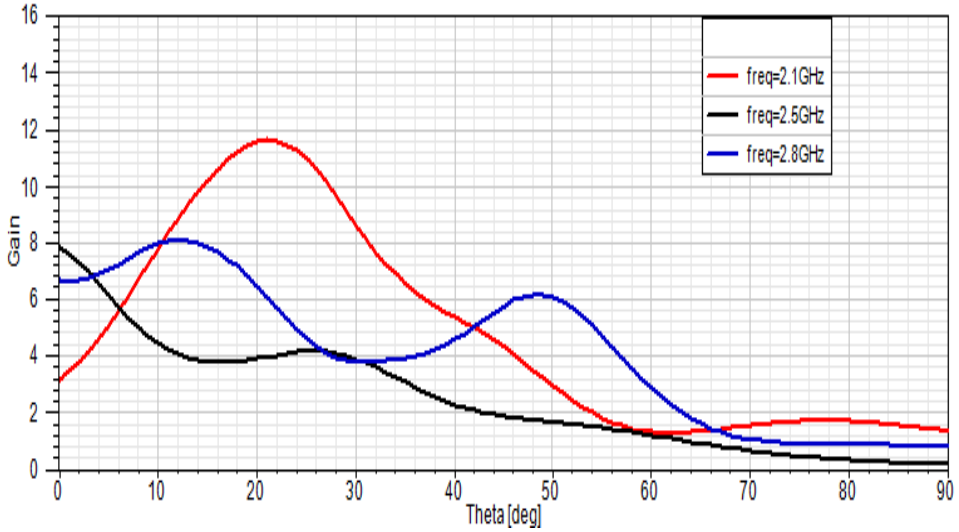

(a)

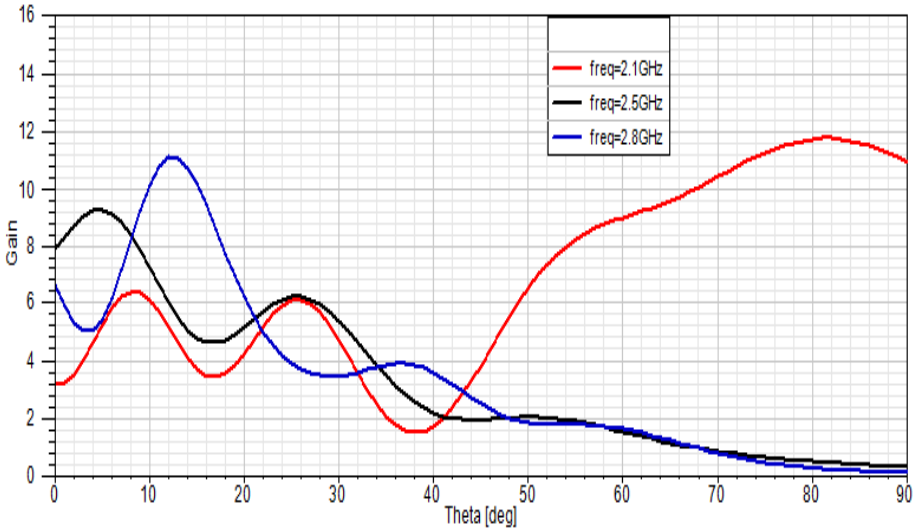

(b)

Fig. 4.3. Scan element pattern for Element 3 in 5x5 U-slot array with Diamond patch orientation at (a) φ=0° and (b) φ=90°

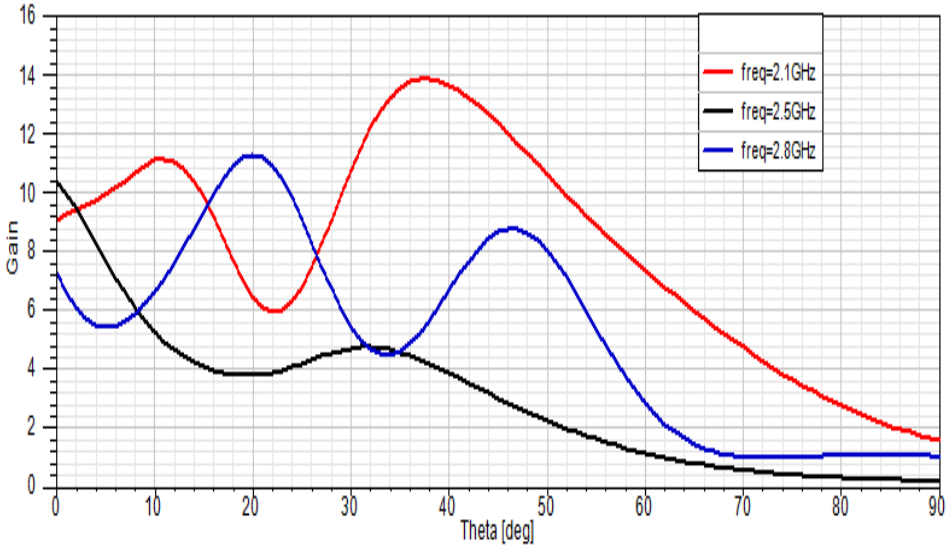

(a)

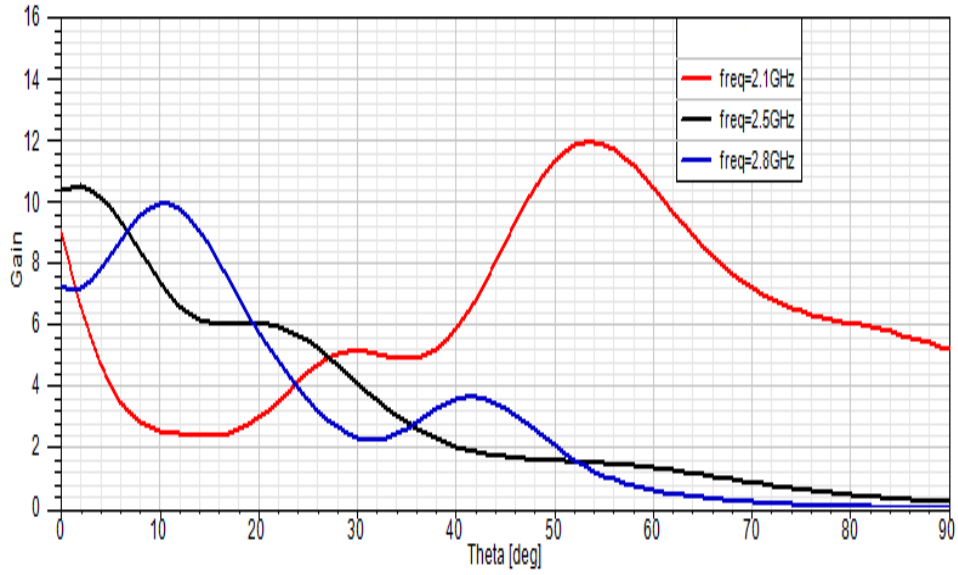

(b)

Fig. 4.4. Scan element pattern for Element 8 in 5x5 U-slot array with Diamond patch orientation at (a) φ=0° and (b) φ=90°

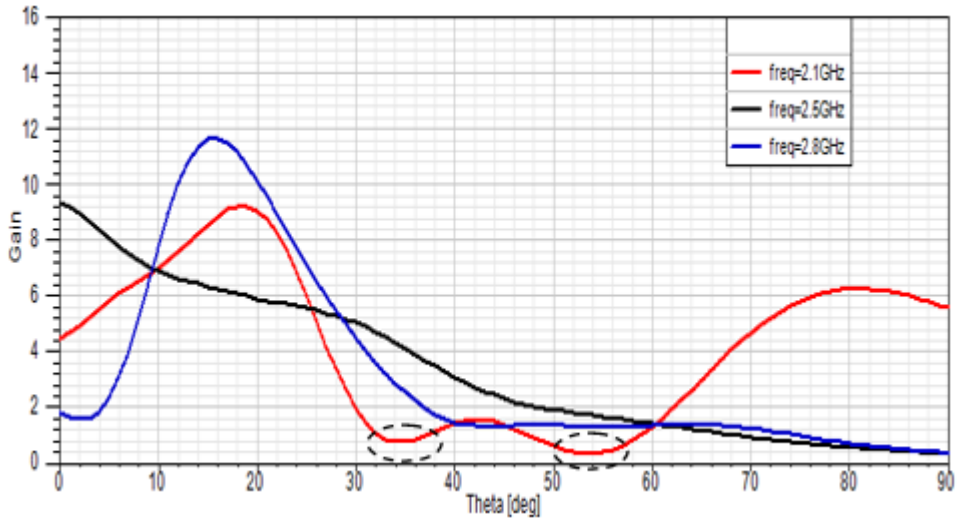

(a)

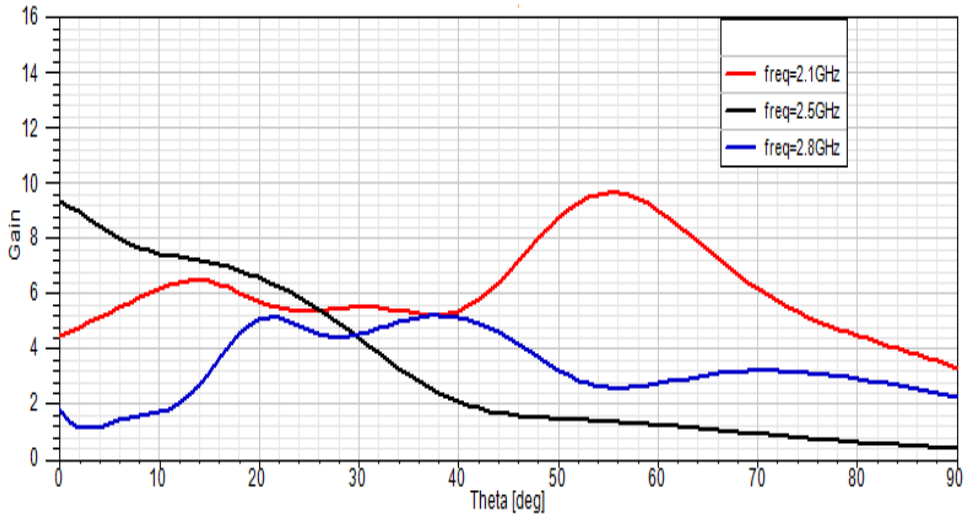

(b)

Fig. 4.5. Scan element pattern for Element 13 in 5x5 U-slot array with Diamond patch orientation at (a) φ=0° and (b) φ=90°

The 5x5 U-slot microstrip patch antenna array shown in Fig. 4.6 models the E-plane patch orientation in U-slot topology (c) in Fig. 3, which shows the most mutual coupling. In Fig. 4.7, the VSWR bandwidth of the isolated U-slot element is compared with the VSWR bandwidth of the center elements in the array, namely 3, 8, and 13. Figure 4.7 shows good agreement between the VSWR bandwidth of the isolated element and elements 3, 8, and 13 in the frequency range of 2-3 GHz indicating that adjacent elements do not impact the VSWR result in the bandwidth of interest.

Figures 4.8 (a) and (b) show the scan element patterns at different frequencies within the 2-3 GHz bandwidth for element 3 at φ=0° and φ=90°, respectively. As shown in Fig. 4.8 (a), a blind spot is observed at scan angle 40°. Figure 4.8 (b) shows blind spots at scan angles 40° to 70°. Figures 4.9 (a) and (b) show the scan element patterns at different frequencies for element 8 at φ=0° and φ=90°, respectively. As shown in Fig. 4.9 (a), a blind spot is observed at scan angle 35°. Figure 4.9 (b) shows blind spots at scan angles 40° to 70°. Figures 4.10 (a) and (b) show the scan element patterns at different frequencies for element 13 at φ=0° and φ=90°, respectively. No blind spots are observed in Fig. 4.10 (a). Figure 4.10 (b) shows blind spots at scan angles 25°, 35°, and 55°.

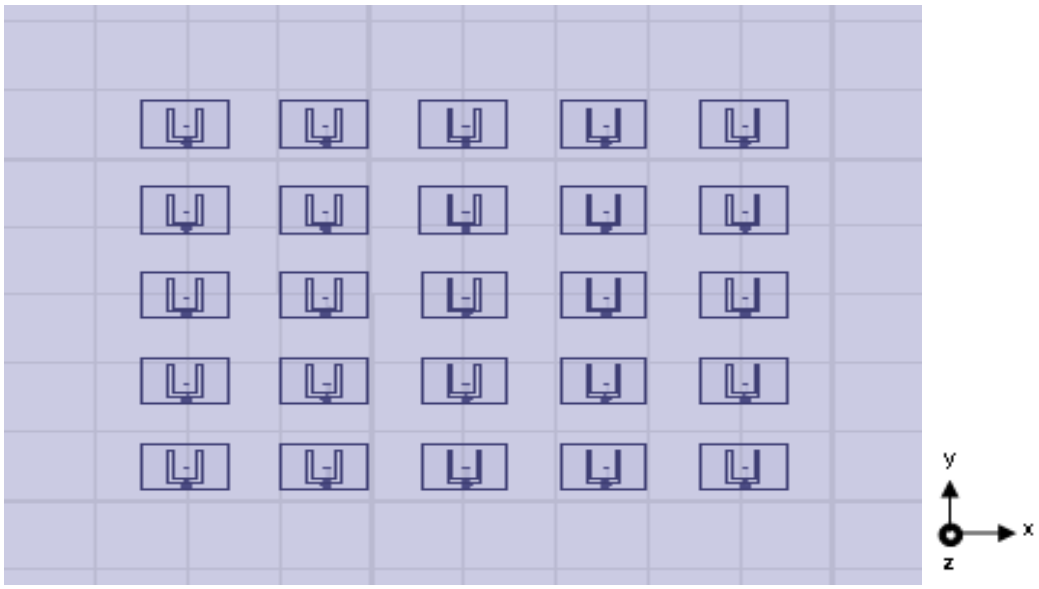

Fig. 4.6. 5x5 U-slot array with E-plane patch orientation [64] (© 2014 IEEE)

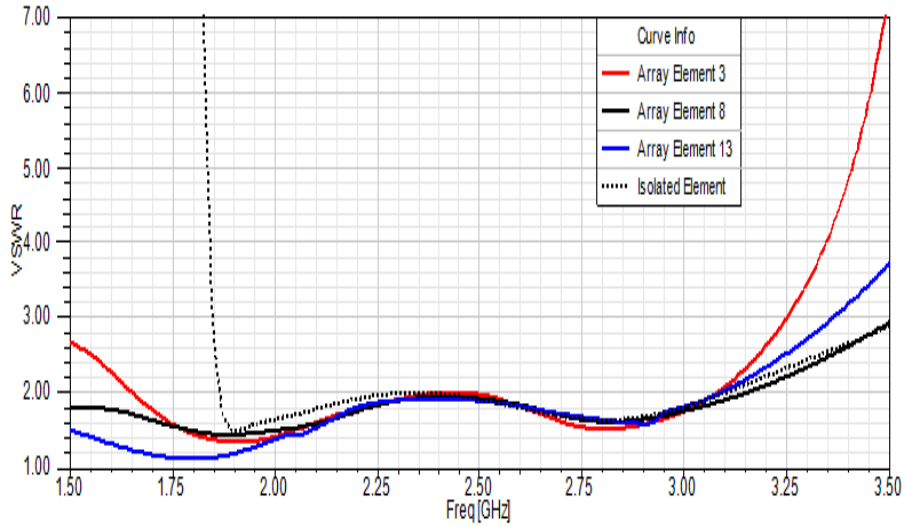

Fig. 4.7. VSWR for selected elements in 5x5 U-slot array with E-plane patch orientation

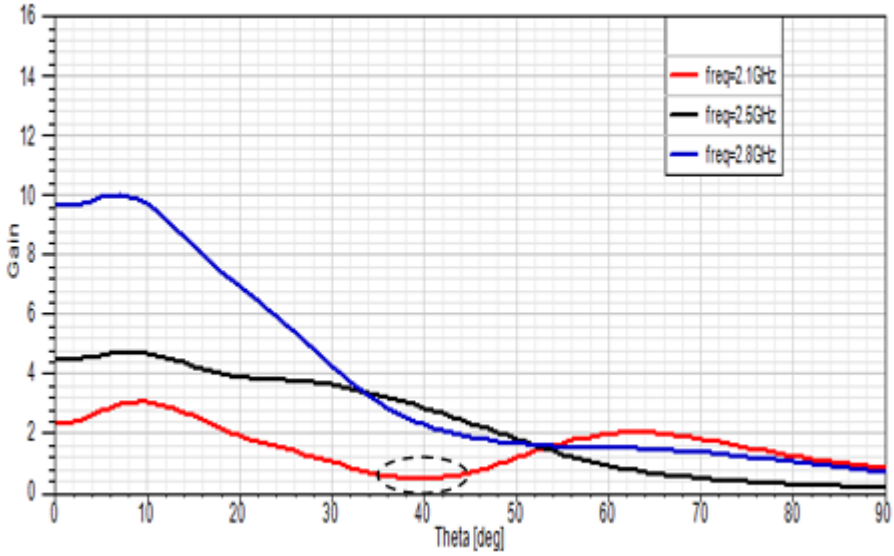

(a)

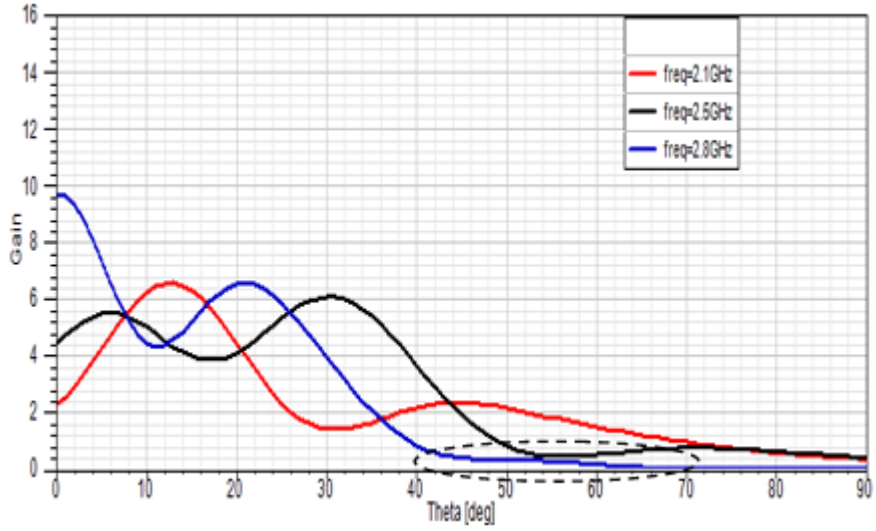

(b)

Fig. 4.8. Scan element pattern for Element 3 in 5x5 U-slot array with E-plane patch orientation at (a) φ=0° and (b) φ=90°

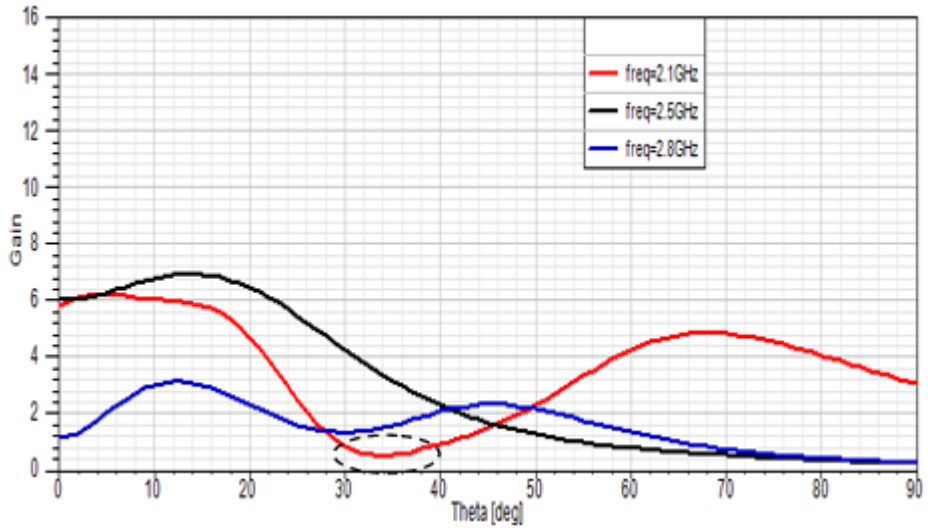

(a)

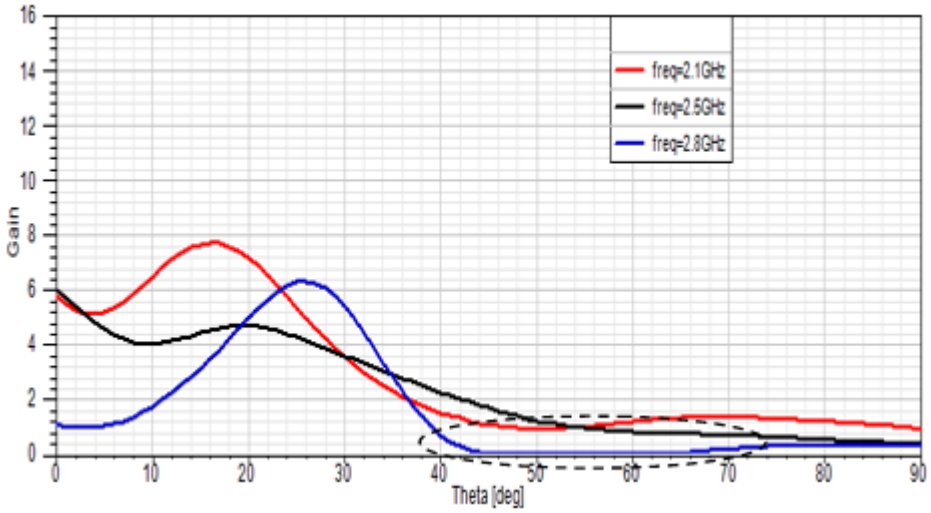

(b)

Fig. 4.9. Scan element pattern for Element 8 in 5x5 U-slot array with E-plane patch orientation at (a) φ=0° and (b) φ=90°

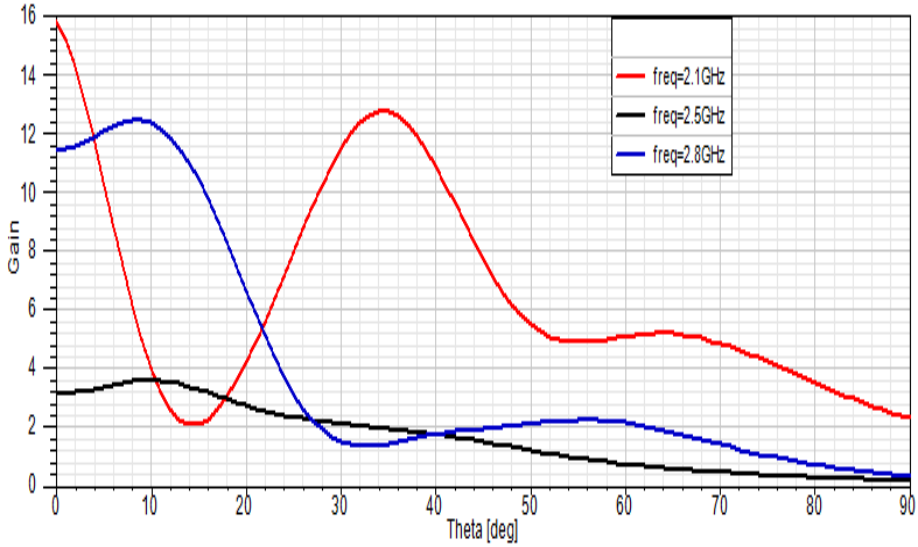

(a)

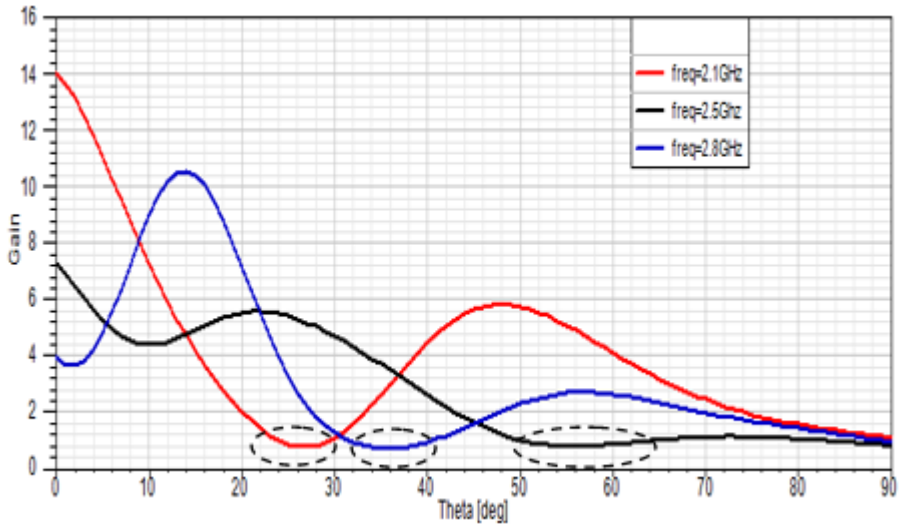

(b)

Fig. 4.10. Scan element pattern for Element 13 in 5x5 U-slot array with E-plane patch orientation at (a) φ=0° and (b) φ=90°

4.2 Nonuniform Excitation and Element Spacing in Sidelobe Reduction of a Linear Microstrip Phased Array Antenna

In this section, the effect of nonuniform excitation and inter-element spacing on the sidelobe reduction of a wideband U-slot microstrip patch phased arrays is examined. To achieve this, a study was performed on a 17-element L-probe-fed U-slot microstrip linear phased array in which the array patterns were examined at different combinations of uniform and nonuniform excitation with uniform and nonuniform inter-element spacing as the array scanned 60° away from broadside.

The 17-element L-probe-fed U-slot microstrip linear phased array model with E-plane and H-plane patch orientations is shown in Fig. 4.11. The array model is simulated and analyzed using the HFSS FEM solver.

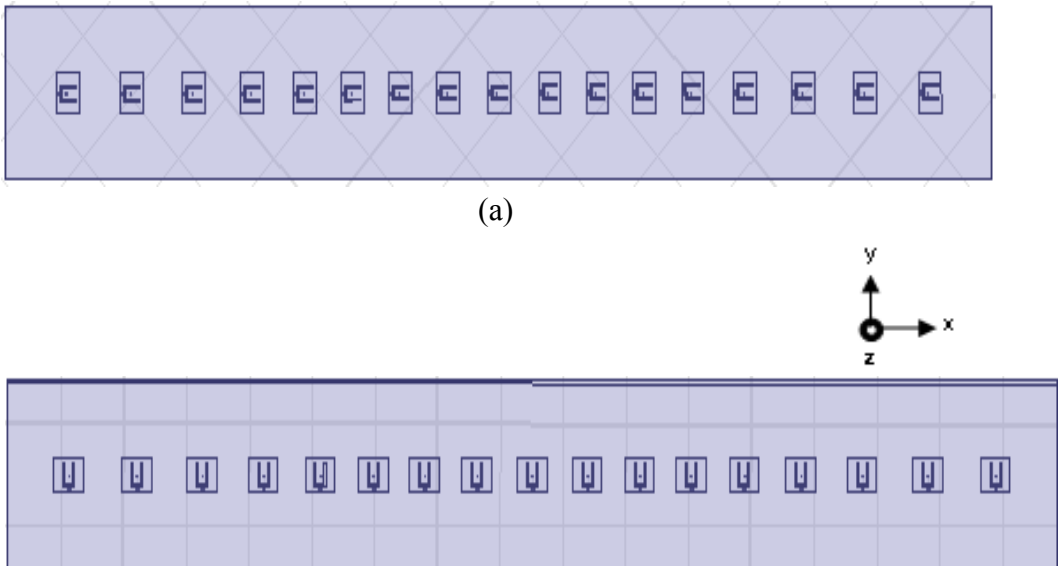

(a)

(b)

Fig. 4.11. 17-element L-probe-fed U-slot array. (a) E-plane patch orientation (b) H-plane patch orientation [65] (© 2015 IEEE)

The U-slot microstrip patch antenna design and geometry is described in chapter 3. The impedance bandwidth for the L-probe-fed U-slot microstrip antenna with ε_r = 2.2 substrate was found to be between 2-3 GHz and the mutual coupling between two elements was found to be around -20dB. The inter-element spacing between the patch edges is taken to be 0.39λ (where λ corresponds to the 2.4 GHz design frequency) for uniform spacing. For nonuniform spacing, Eq. 4.1, from [60], is used to calculate the correction factor, ε_n, by which the inter-element spacing of the uniform spacing will be increased or decreased.

$$\epsilon_n = 2A\left(\frac{N}{\pi}\right)^3 \sum_{k=1}^{K} (-1)^k \frac{\sin\dfrac{n\pi}{2N}(2k+1)}{(2k+1)^2} \tag{4.1}$$

In Eq. 4.1, N is the number of elements in the array, K is the number of sidelobes reduced, and A is the amount of reduction. After several optimization runs, K=1 and A=0.00786, which corresponds to -42dB, were chosen. MATLAB code (see Appendix A.3) is used to solve Eq. 4.1 to calculate the correction factor. For nonuniform excitation, a -35dB Taylor current distribution pattern is used to excite the elements. A progressive phase shift is used to steer the main beam.

In the broadside array patterns shown in Figs. 4.12(a) and 4.13(a), it is observed that the nonuniform inter-element spacing slightly reduces the sidelobes adjacent to the main beam as discussed in [60]. Comparing the nonuniform spacing results with the nonuniform excitation results in the same figures, the nonuniform excitation results present far better reduction in sidelobe levels. However, as the array scans away from broadside towards

θ=60°, as shown in Figs. 4.12(b) and 4.13(b), dramatic increase in the sidelobe levels for the nonuniform excitation and uniform spacing case is observed. In Fig. 4.12(b), a 0dB grating lobe is visible at -90° and in Fig. 4.13(b), a -12dB sidelobe is visible at -90°. Comparing the nonuniform excitation and uniform spacing results in Fig. 4.12(b) with the nonuniform spacing results, there is a grating lobe reduction by -7dB in the case of uniform excitation and nonuniform spacing and a grating lobe reduction by -14dB in the case of nonuniform excitation and spacing. Similarly, comparing the nonuniform excitation and uniform spacing results in Fig. 4.13(b) with the nonuniform spacing results, there is a sidelobe reduction by -2dB in the case of uniform excitation and nonuniform spacing and a sidelobe reduction by -10dB in the case of nonuniform excitation and spacing. The grating lobe reduction by nonuniform element spacing is mainly due to the disruption of the periodic spatial aliasing effect phenomena, which causes some sidelobes to become substantially large in amplitude approaching the level of the main lobe.

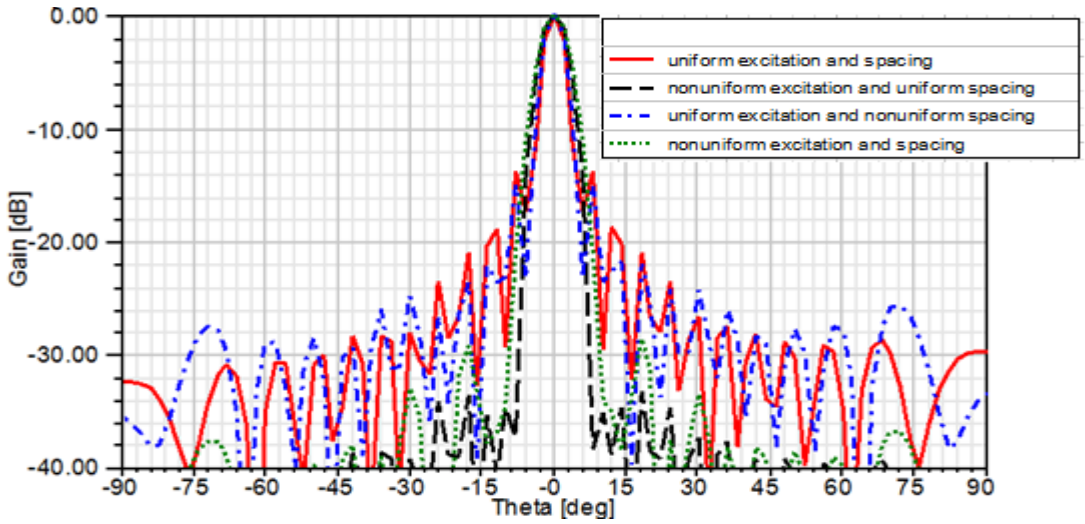

(a)

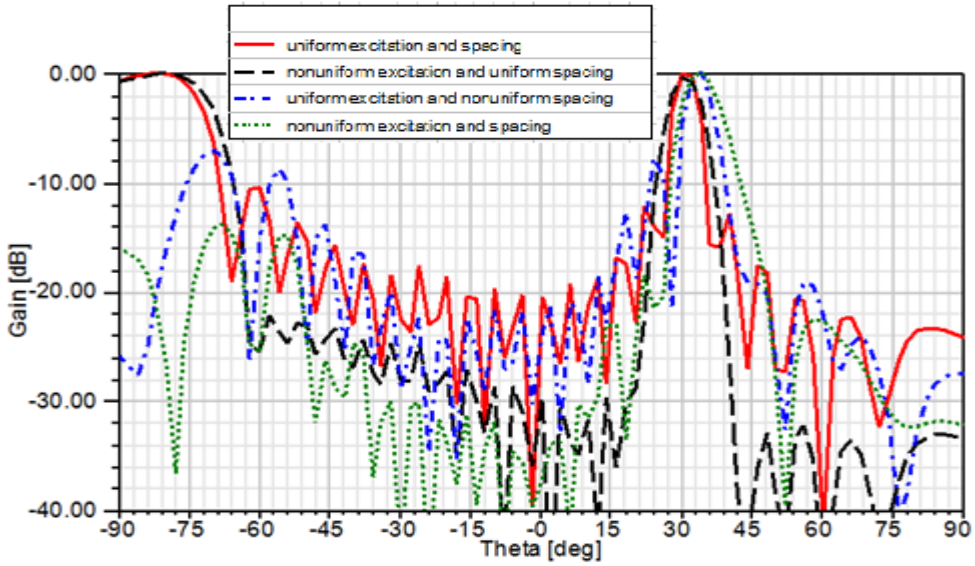

(b)

Fig. 4.12. E-plane array pattern at 2.4GHz at (a) broadside (b) scan angle θ=60° [65] (© 2015 IEEE)

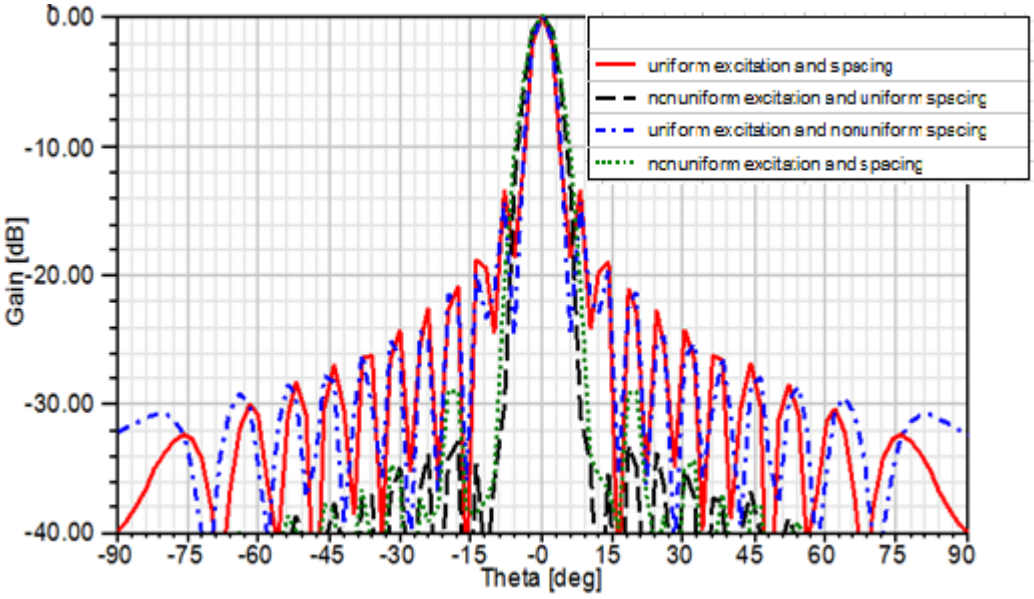

(a)

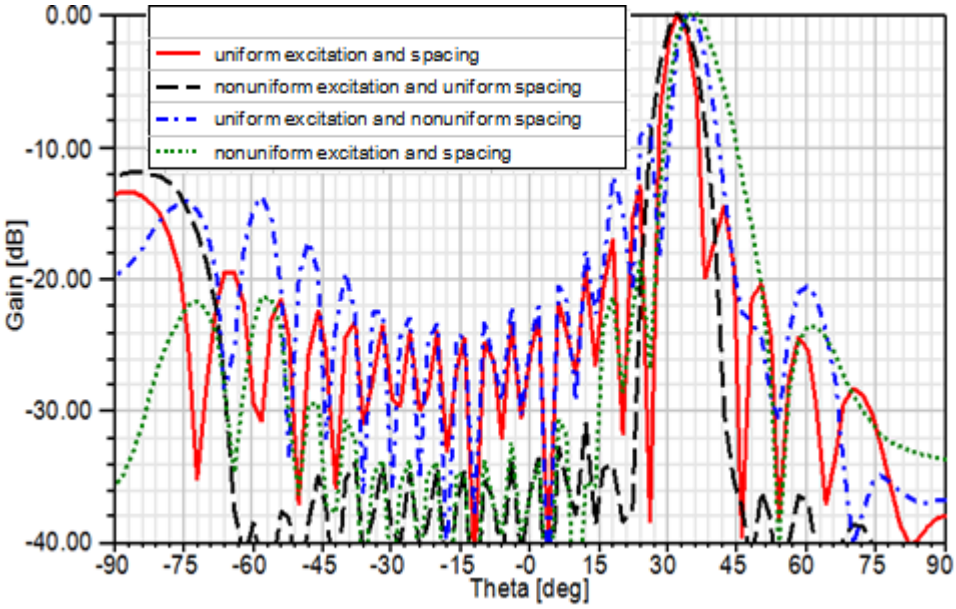

(b)

Fig. 4.13. H-plane array pattern at 2.0GHz at (a) broadside (b) scan angle θ=60° [65] (© 2015 IEEE)

4.3 Summary

In this chapter, the scan element pattern of a 5x5 planar phased array on ε_r = 2.2 substrate using the diamond patch and E-plane patch orientations in chapter 3 is characterized. Results show blind spots are more prevalent in the E-plane patch orientation which has the most mutual coupling between the array elements and less prevalent in the diamond patch orientation with the least mutual coupling. Hence, the diamond patch orientation will be the ideal orientation to use in a phased array design.

Sidelobe reduction using nonuniform excitation and inter-element spacing in a wideband U-slot microstrip patch phased arrays is examined. Results show a sidelobe reduction by at least -10dB when nonuniform excitation and nonuniform inter-element

spacing are used as opposed to using nonuniform excitation only or nonuniform spacing only.

CHAPTER 5

UWB ENHANCEMENT OF MICROSTRIP PATCH ANTENNA USING THE THEORY CHARACTERSITIC MODES

The need for antennas with high bandwidth is continuing to fuel a lot of research especially in the fields of radar, wireless communication and medical imaging. Microstrip patch antennas are a class of antennas that exhibit low-profile, compact, conformal, cost-effective, and easy-to-fabricate designs. Despite these advantages, microstrip patch antennas suffer from a major drawback which is narrow bandwidth. For the past couple of decades extensive research has been dedicated to the area of bandwidth broadening and miniaturization techniques of microstrip patch antennas. Some of these bandwidth broadening techniques are by means of introduction of parasitic elements and patch slots, which introduce additional resonances in addition to the main patch resonance. Another technique is by means of thick substrates of low permittivity, which will have the side effect of introducing higher inductive reactance due to the longer coaxial feed probe. Some of the patch slot geometries found in the literature are: Square, rectangular, triangular, circular, elliptical, U-slot, V-slot [66], E-slot [67], and more. Although it is generally understood that patch slots introduce new resonances that contribute to broadening the bandwidth, it is not well understood why some patch slots present better bandwidth than others. Some of the miniaturization techniques are by means of smaller ground planes, which will have the side effect of having low impedance bandwidth. Although it is generally understood that larger ground planes contribute to bandwidth broadening, their resonant behavior is not well understood. One valuable tool that is helping antenna designers gain better understanding and physical insight of the radiating nature and resonant behavior of the microstrip patch

antenna is the Theory of Characteristic Modes (TCM) [68-90]. By understanding the resonant behavior of the different patch slot geometries and other antenna elements using TCM, novel antenna designs with the most resonant structures can be proposed to achieve the most radiation and impedance bandwidth.

In this chapter, TCM is utilized to characterize the resonant behavior of different patch shapes, patch slot geometries, substrate permittivities, ground plane sizes, and excitation feed probes to identify the individual antenna structures which are more resonant and hence contribute significantly to the radiated fields.

5.1 Overview of the Theory of Characteristic Modes

Characteristic modes represent a set of orthogonal real currents on the surface of a conducting body. They depend only on the shape and size of structure and are independent of the excitation feed [68]. The characteristic modes are obtained by solving the following eigenvalue equation [68]:

$$[X]\vec{J}_n = \lambda_n[R]\vec{J}_n \qquad (5.1)$$

where J_n are the characteristic currents, λ_n are the eigenvalues, R and X are the real and imaginary parts of the impedance matrix Z of the structure, which is obtained from the Method of Moments solution.

Eigenvalues where $\lambda_n < 0$ indicate the mode contributes to storing electric energy. Eigenvalues where $\lambda_n > 0$ indicate the mode contributes to storing magnetic energy.

Eigenvalues where $\lambda_n = 0$ are desirable and indicate the mode is at resonance and radiates efficiently.

A more convenient way to plot the eigenvalues is by plotting the normalized amplitude of the current modes or the *modal significance* expressed as [69]:

$$\text{Modal Significance} = \left| \frac{1}{1 + j\lambda_n} \right| \tag{5.2}$$

Modes where the modal significance is close to 1 indicate that they contribute significantly to radiation, whereas modes with modal significance close to 0 indicate they do not. Therefore, modal significance gives the antenna designer physical insight on the resonant behavior of an antenna structure independent of the source excitation.

To determine which modes will be excited by the source feed, the *modal excitation coefficient* is defined as [69]:

$$V_n^I = \oiint \boldsymbol{J}_n^* \bullet \boldsymbol{E}^I \, dS \tag{5.3}$$

The modal excitation coefficient models the coupling of the excitation field, E^I, and the n^{th} mode, J_n, thus providing a physical insight on which modes are excited by the source feed and which source feed excites the most modes that contribute to radiation.

The ARPACK eigensolver within the commercially available 3D electromagnetic field solver, FEKO, is used to solve the eigenvalue problem defined in Eq. 5.1 and compute

the characteristic modes and corresponding modal significance of each mode.

5.2 Modal Analysis of Patch Shapes

Figure 5.1 illustrates four different patch shapes to be analyzed using TCM. The patches are analyzed alone without any substrate, ground or excitation source to compare their different resonant behavior. All the patches have the same area of 296 m^2. The rectangular patch dimensions are 20.25mm by 14.62mm. The equilateral triangular patch's side equals 26.15mm. The circular patch's radius equals 9.71mm, and the square patch's side equals 17.21mm.

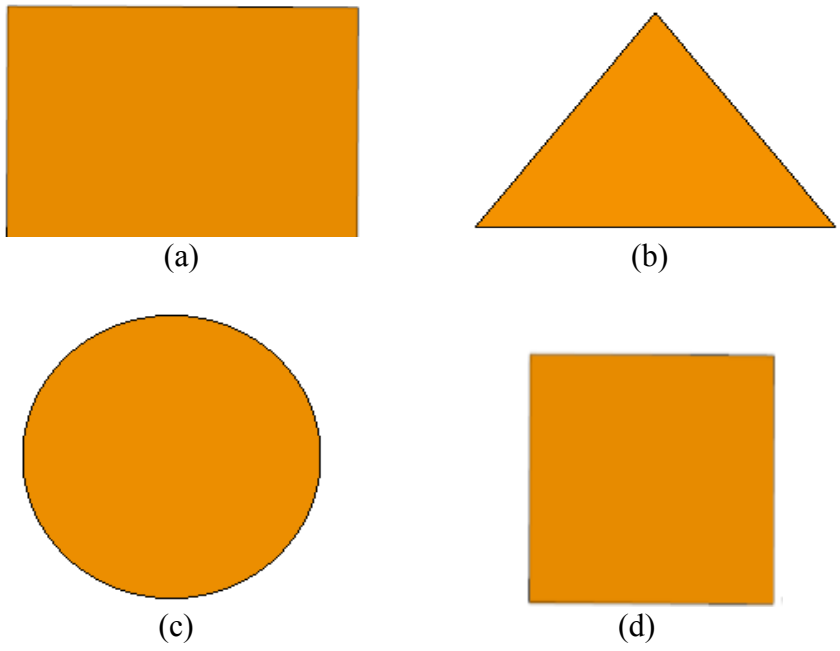

Fig. 5.1. Patch shapes. (a) Rectangular patch (b) Equilateral triangular patch (c) Circular patch (d) Square patch

Figure 5.2 shows the modal significance of the top 5 significant eigenmodes for the 4 different patch shapes. The modal significance is analyzed over the selected frequency range between 2.5 GHz and 8.5 GHz and is computed using the 3D field solver, FEKO. Modes with modal significance values above 0.8 are considered good radiators. In Fig. 5.2(a), modes 1 and 2 are the good radiators in the frequency range 5.2-8.5 GHz with mode 2 contributing minimally to radiation. In Fig. 5.2(b), modes 1 and 2 are good radiators in the frequency range 5.3-8.5 GHz with both modes contributing equally to radiation. In Fig. 5.2(c), modes 1 and 2 are good radiators in the frequency range 6.7-8.5 GHz with both modes contributing equally to radiation. In Fig. 5.2(d), modes 1 and 2 are good radiators in the frequency range 6.3-8.5 GHz with both modes contributing equally to radiation.

The above modal analysis demonstrates that both the rectangular and equilateral triangular patches are good radiators with the rectangular patch having a slightly wider frequency range.

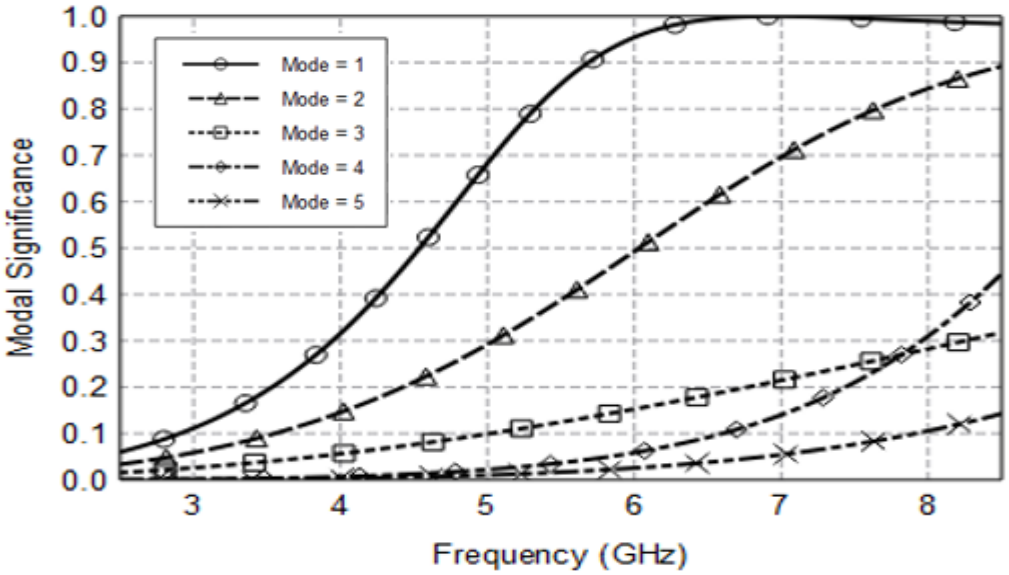

(a)

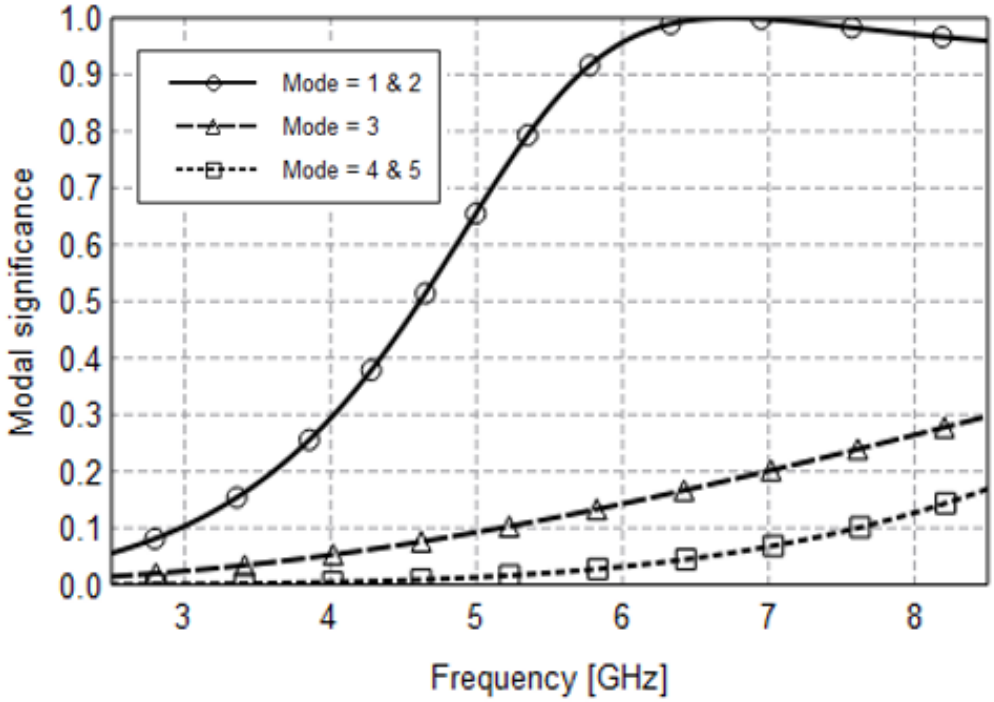
Modal significance
Frequency [GHz]
Mode = 1 & 2
Mode = 3
Mode = 4 & 5
1.0
0.9
0.8
0.7
0.6
0.5
0.4
0.3
0.2
0.1
0.0
3
4
5
6
7
8

(b)

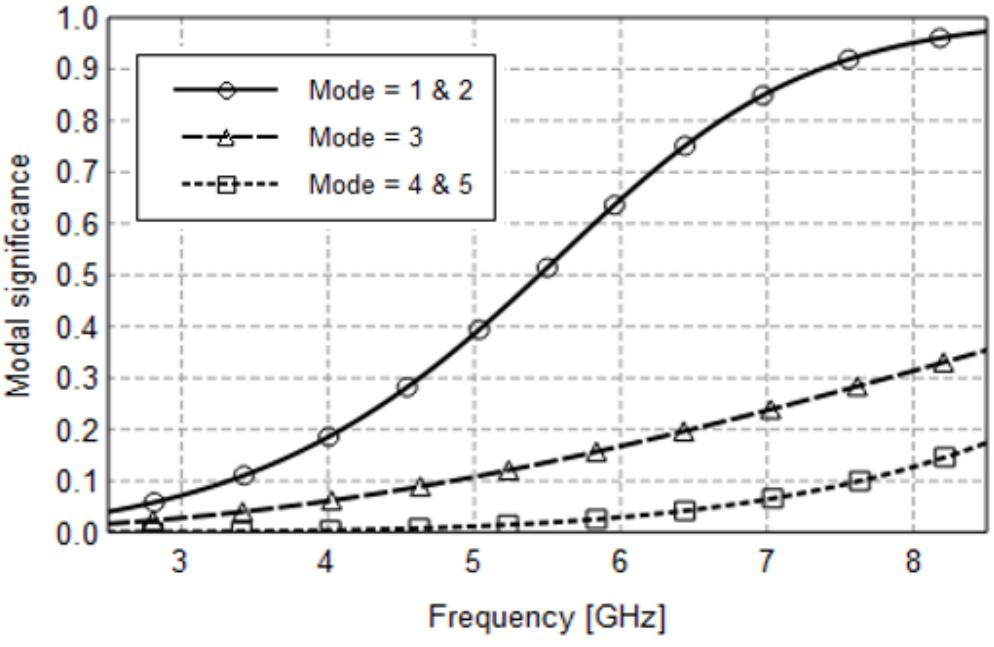
Modal significance
Frequency [GHz]
Mode = 1 & 2
Mode = 3
Mode = 4 & 5
1.0
0.9
0.8
0.7
0.6
0.5
0.4
0.3
0.2
0.1
0.0
3
4
5
6
7
8

(c)

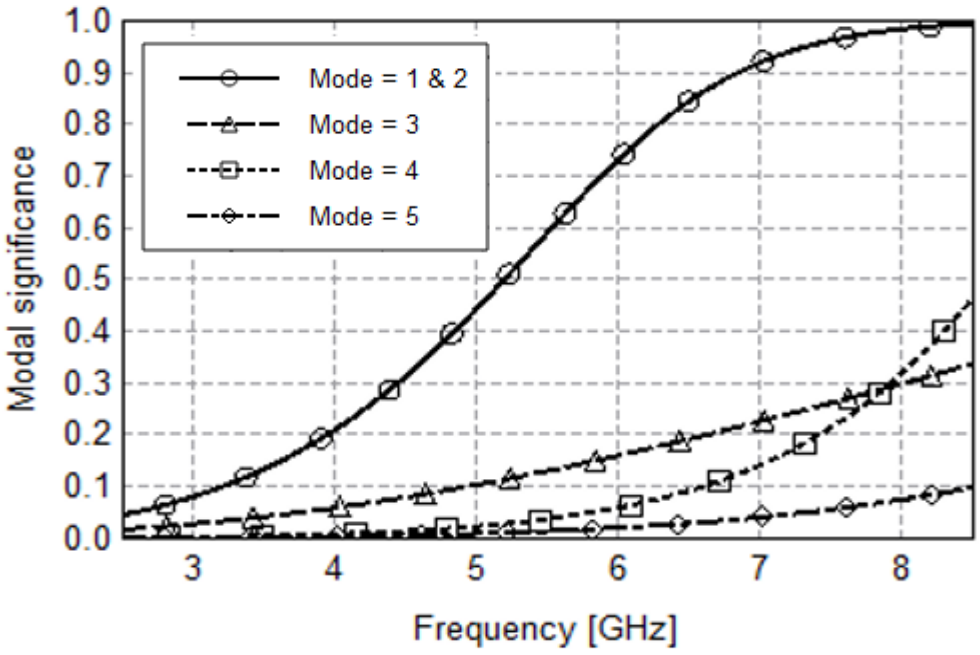

(d)

Fig. 5.2. Modal Significance of different patch shapes. (a) Rectangular patch (b) Equilateral triangular patch (c) Circular patch (d) Square patch

5.3 Modal Analysis of Patch Slot Geometries

Figure 5.3 illustrates six different patch slot geometries to be analyzed using TCM. The patches are analyzed alone without any substrate, ground or excitation source to compare their different resonant behavior. The first rectangular patch in Fig. 5.3(a) has no slots. The U-slot patch is shown in Fig. 5.3(b). The other patches in Fig. 5.3 are variations of the U-slot patch. For the II-slot patch in Fig. 5.3(c), the bottom side of the U-slot was removed. For the O-slot patch in Fig. 5.3(d), an extra top slot was added to the U-slot. For the E-slot patch in Fig. 5.3(e), an extra slot was added in the middle of the U-slot. For the V-slot patch in Fig. 5.3(f), the U-slot arms were shifted outwards by 25°.

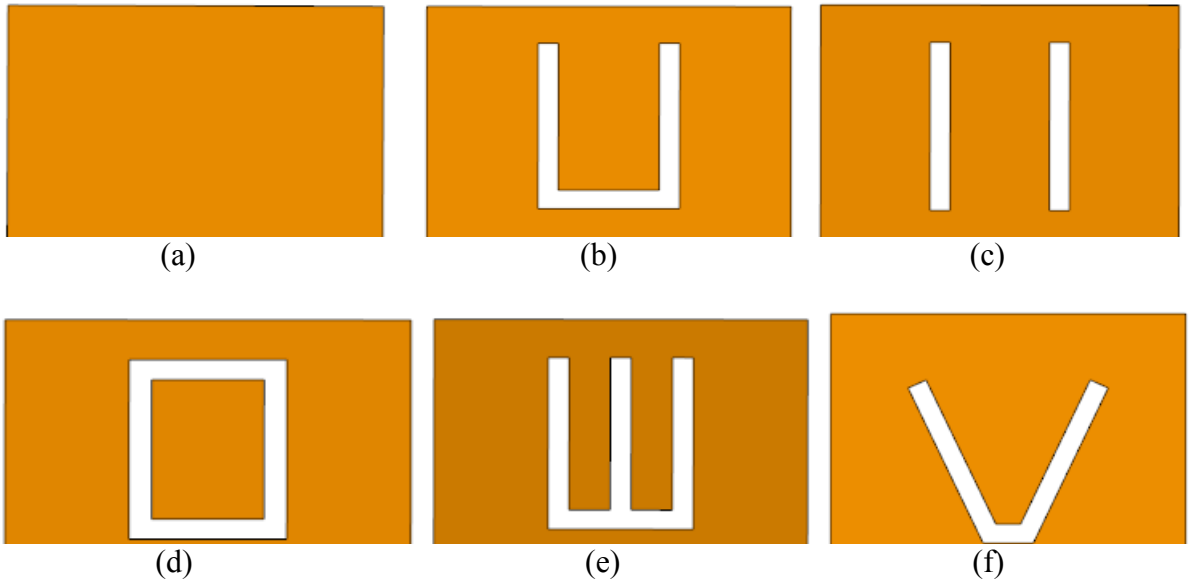

Fig. 5.3. Patch slot geometries. (a) Rectangular patch (b) U-slot patch (c) II-slot patch (d) O-slot patch (e) E-slot patch (f) V-slot patch [85] (© 2016 ACES)

Figure 5.4 shows the modal significance of the top 5 significant eigenmodes for the 6 different patch slot geometries. The modal significance is analyzed over the selected frequency range between 2.5 GHz and 8.5 GHz and is computed using the 3D field solver, FEKO. Modes with modal significance values above 0.8 are considered good radiators. In Fig. 5.4(a), modes 1 and 2 are the good radiators in the frequency range 5.2-8.5 GHz with mode 2 contributing minimally to radiation. In Fig. 5.4(b), modes 1, 2, and 5 are the good radiators in the frequency range 4.9-8.5 GHz with modes 2 and 5 contributing minimally to radiation. In Fig. 5.4(c), modes 1 and 2 are the good radiators in the frequency range 5.0-8.5 GHz with mode 2 contributing minimally to radiation. In Fig. 5.4(d), modes 1 and 2 are the good radiators in the frequency range 4.8-8.5 GHz with both modes contributing equally to radiation. In Fig. 5.4(e), modes 1, 2, and 5 are the good radiators in the frequency range 4.8-

8.5 GHz with modes 2 and 5 contributing minimally to radiation. Additionally, mode 1 experiences a band notch close to 7.2 GHz. This is an expected behavior of the E-slot patch antenna as the extra slot in the middle acts as a band notch. In Fig. 5.4(f), modes 1 and 2 are good radiators in the frequency range 5.0-8.5 GHz with both modes contributing equally to radiation.

The above modal analysis demonstrates that the U-slot and E-slot have both the most number of modes that are good radiators in the frequency range 4.9-8.5 GHz, however, the E-slot does not cover the entire frequency range due to its band notch around 7.2 GHz. Therefore, it is concluded that the U-slot has the shape with the most resonant behavior and hence will be a good candidate to achieve the highest impedance bandwidth.

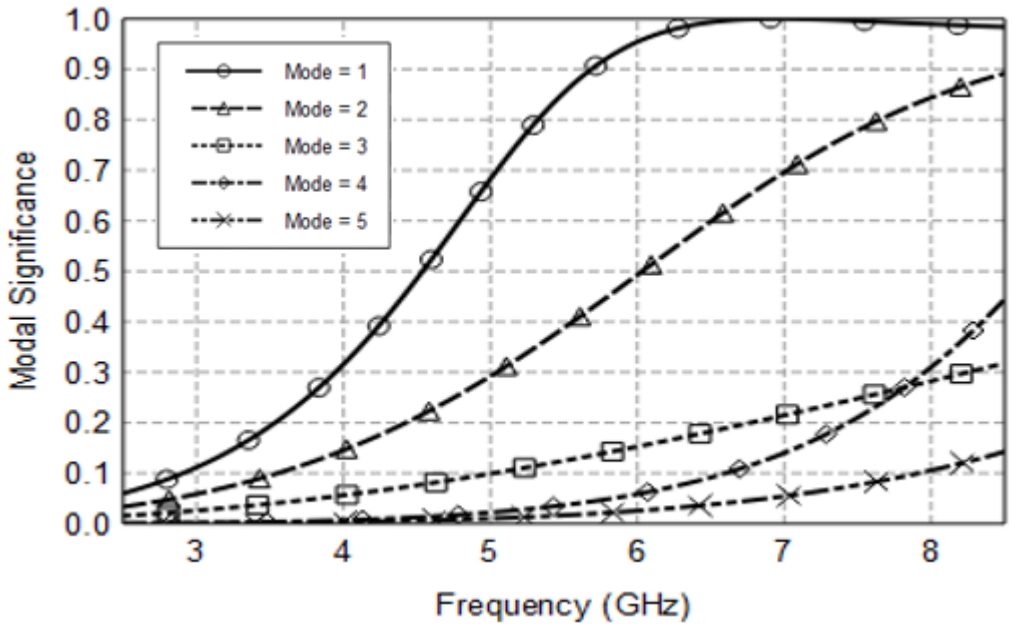

(a)

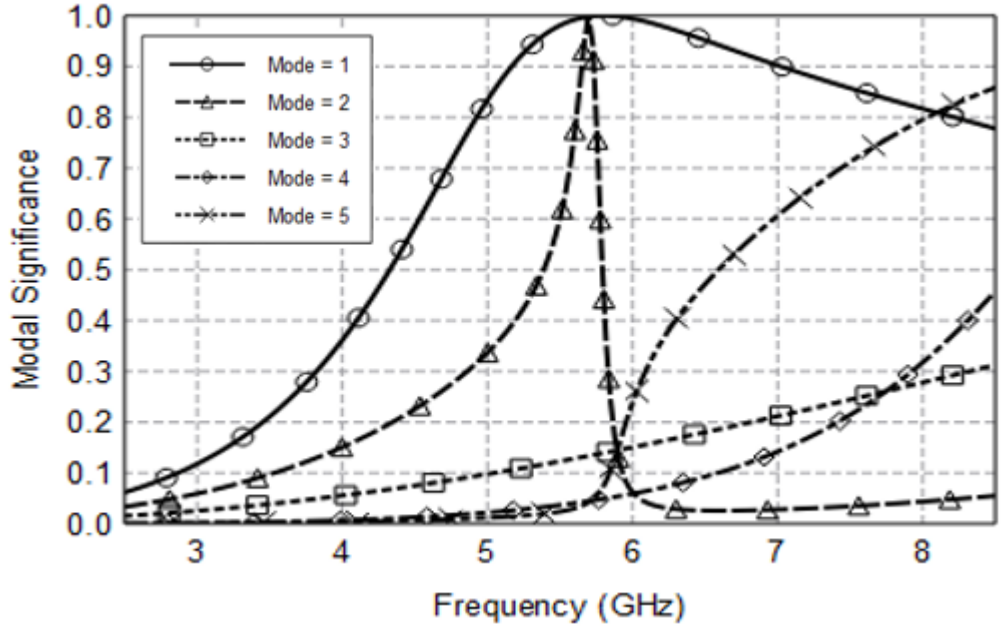
Modal Significance
Frequency (GHz)
Mode = 1
Mode = 2
Mode = 3
Mode = 4
Mode = 5
1.0
0.9
0.8
0.7
0.6
0.5
0.4
0.3
0.2
0.1
0.0
3
4
5
6
7
8

(b)

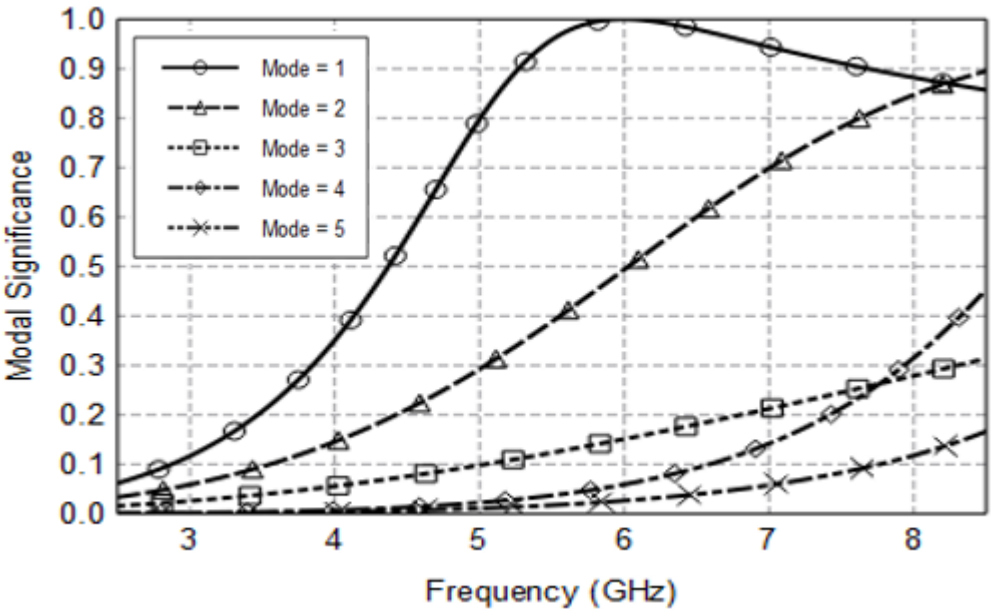
Modal Significance
Frequency (GHz)
Mode = 1
Mode = 2
Mode = 3
Mode = 4
Mode = 5
1.0
0.9
0.8
0.7
0.6
0.5
0.4
0.3
0.2
0.1
0.0
3
4
5
6
7
8

(c)

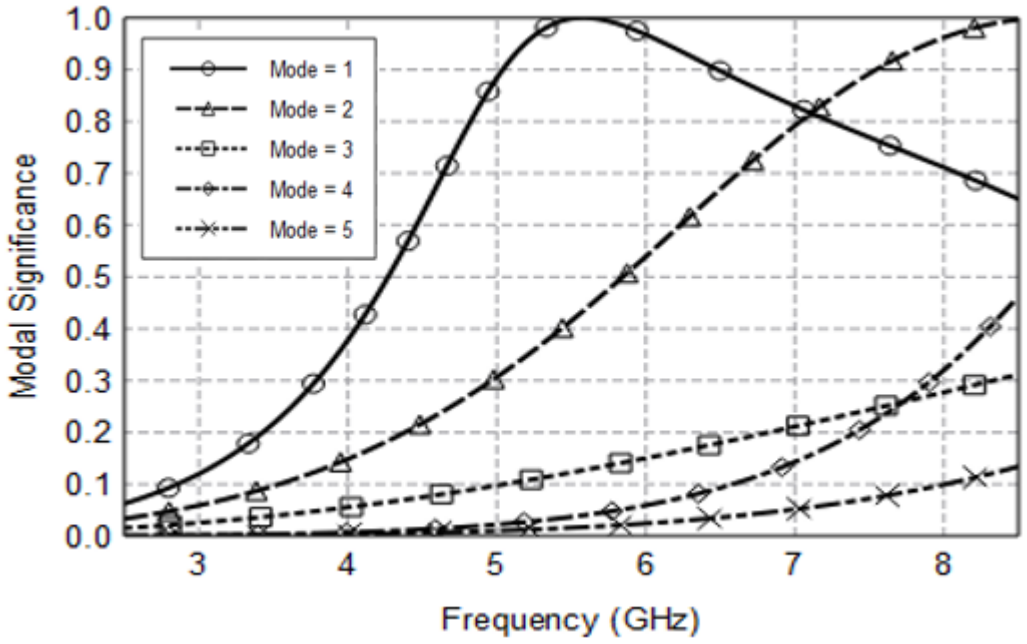
Modal Significance
Frequency (GHz)
Mode = 1
Mode = 2
Mode = 3
Mode = 4
Mode = 5
1.0
0.9
0.8
0.7
0.6
0.5
0.4
0.3
0.2
0.1
0.0
3
4
5
6
7
8

(d)

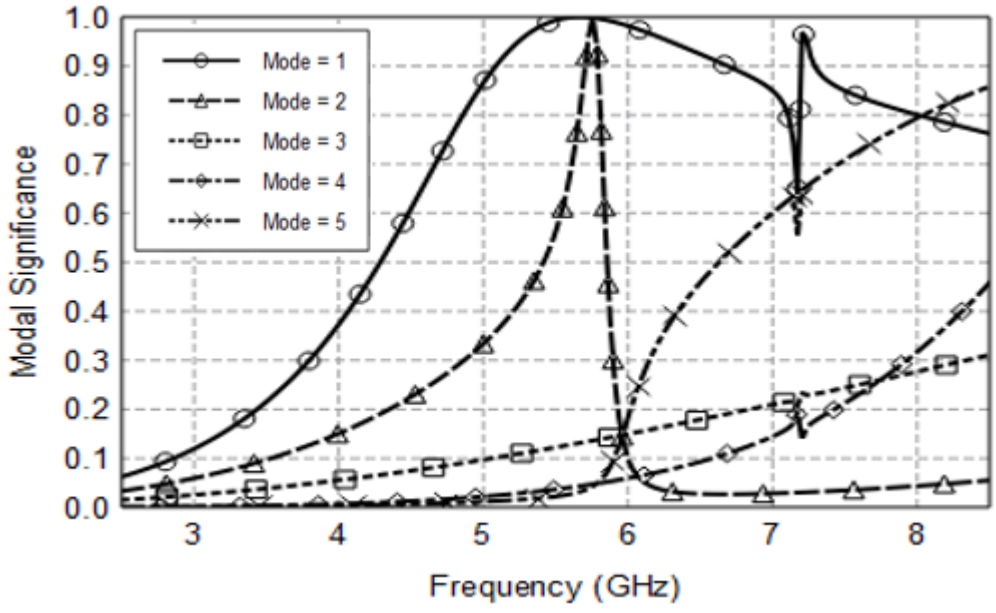
Modal Significance
Frequency (GHz)
Mode = 1
Mode = 2
Mode = 3
Mode = 4
Mode = 5
1.0
0.9
0.8
0.7
0.6
0.5
0.4
0.3
0.2
0.1
0.0
3
4
5
6
7
8

(e)

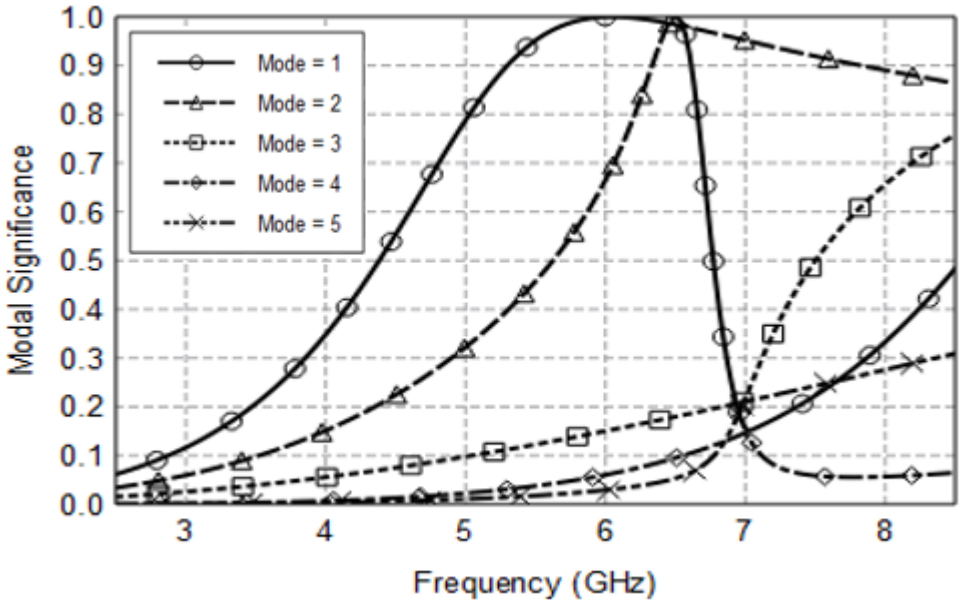

(f)

Fig. 5.4. Modal Significance of different patch slot geometries. (a) Rectangular patch (b) U-slot patch (c) II-slot patch (d) O-slot patch (e) E-slot patch (f) V-slot patch [85] (© 2016 ACES)

5.4 Modal Analysis of Substrate Permittivities

To analyze the characteristic modes for different substrate permittivities, a rectangular patch with 20.25mm width and 14.62mm length is modeled. The rectangular patch is analyzed with infinite substrate and ground and without excitation source. The substrate height is 7.62mm. The resonant behavior of 3 different commercially available substrate materials with low, medium and high permittivities is compared. These are: the *Rogers RT/Duroid 5880* substrate material with $\varepsilon_r = 2.2$ and $\tan(\delta) = 0.0009$, the *FR-4 Epoxy* substrate material with $\varepsilon_r = 4.4$ and $\tan(\delta) = 0.02$, and the *Rogers TMM 10i* substrate

material with $\varepsilon_r = 9.8$ and $\tan(\delta) = 0.002$.

Figure 5.5 shows the modal significance of the top 5 significant eigenmodes for the 3 different substrate permittivities. The modal significance is analyzed over the selected frequency range between 2.5 GHz and 8.5 GHz and is computed using the 3D field solver, FEKO. Modes with modal significance values above 0.8 are considered good radiators.

As shown in Fig. 5.5(a), modes 1, 2, and 4 are the good radiators in the frequency range 3.8-8.5 GHz. In Fig. 5.5(b), modes 1, 2, 3, and 4 are the good radiators in the frequency range 2.8-8.5 GHz. In Fig. 5.5(c), modes 2, 3, 4, 5 and 6 are the good radiators in the frequency range 3.1-8.5 GHz with mode 5 contributing minimally to radiation. The $\varepsilon_r = 9.8$ substrate has the most number of modes radiating, however the frequency bandwidth covered by the $\varepsilon_r = 4.4$ substrate is larger by 0.3 GHz and most importantly the modal significance of its radiating modes is very close to 1 which indicate that they are very good radiators compared to the other substrates. Therefore, the $\varepsilon_r = 4.4$ substrate with $\tan(\delta) = 0.02$ is the most resonant dielectric and will be a good candidate to achieve the highest impedance bandwidth. This is an expected conclusion since the $\varepsilon_r = 4.4$ substrate has the highest loss tangent of 0.02 compared to the other substrates which leads to a lower Q Factor, which in turn leads to a higher bandwidth.

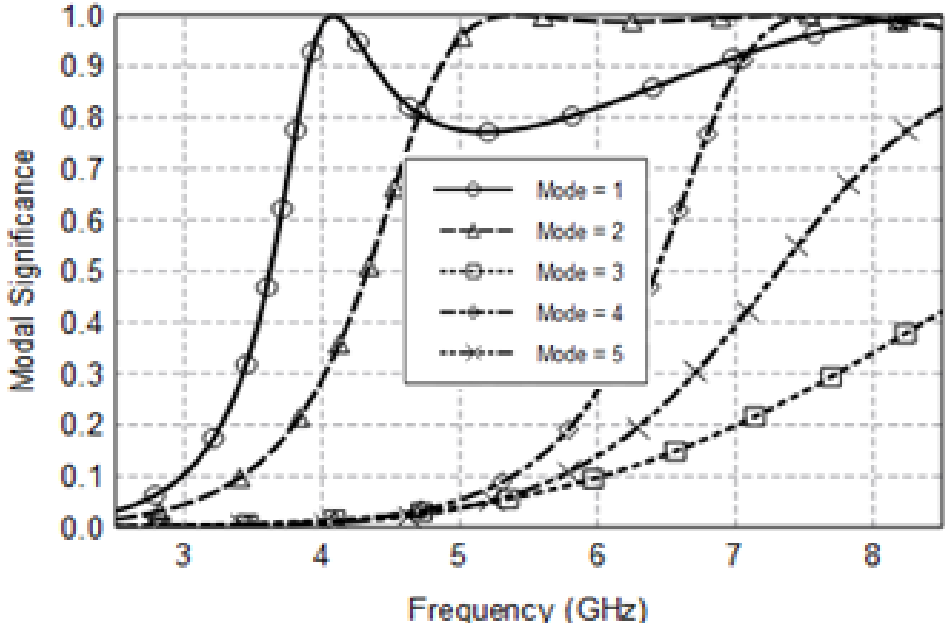
Modal Significance
Frequency (GHz)
Mode = 1
Mode = 2
Mode = 3
Mode = 4
Mode = 5

(a)

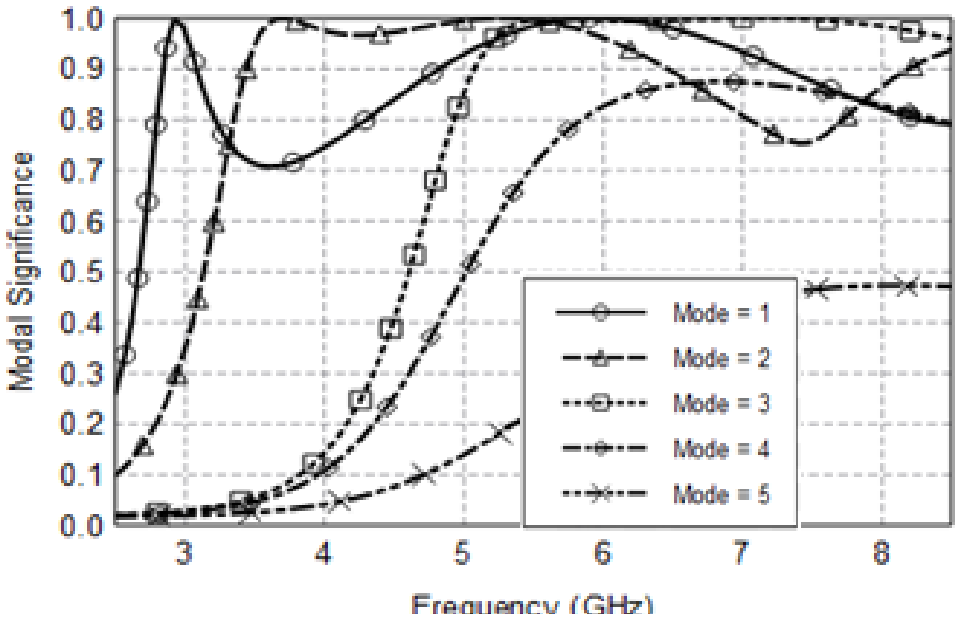
Modal Significance
Frequency (GHz)
Mode = 1
Mode = 2
Mode = 3
Mode = 4
Mode = 5

(b)

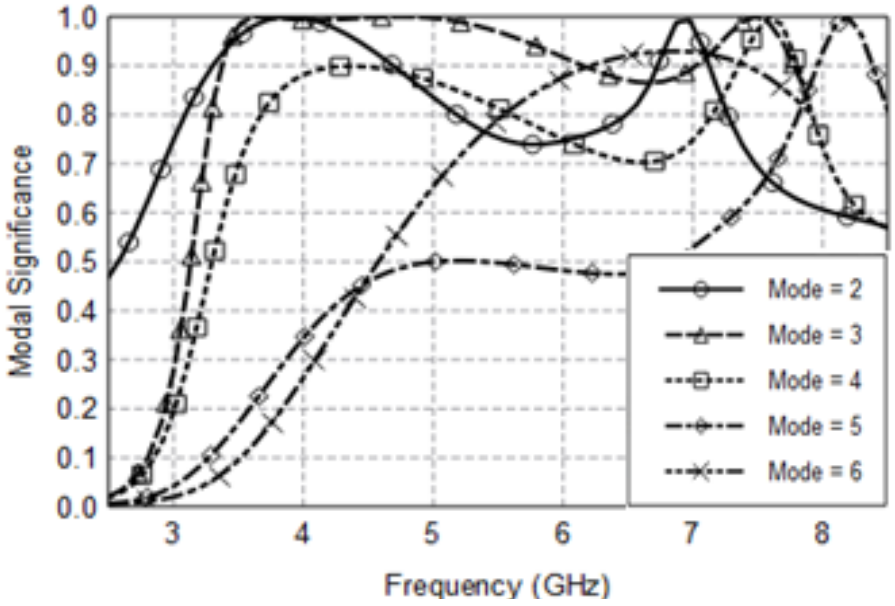

(c)

Fig. 5.5. Modal Significance of rectangular patch with different substrate permittivities. (a) $\varepsilon_r = 2.2$ and $\tan(\delta) = 0.0009$ (b) $\varepsilon_r = 4.4$ and $\tan(\delta) = 0.02$ (c) $\varepsilon_r = 9.8$ and $\tan(\delta) = 0.002$ [86]

5.5 Modal Analysis of Ground Plane Sizes

To analyze the characteristic modes for different ground plane sizes, a rectangular patch with different ground plane dimensions is modeled. The rectangular patch is analyzed with finite substrate and ground plane and without excitation source. A smaller rectangular patch and substrate height is chosen to reduce the computation time. The resonant behavior of 3 different ground plane sizes is compared. The sizes are shown in the legend for Fig. 5.6.

Figure 5.6 shows the modal significance of the top significant eigenmodes for the 3 different ground plane sizes. The modal significance is analyzed over the selected frequency range between 5.0 GHz and 11.0 GHz. Only the modal significance results between 0.9 and

1.0 are shown to zoom in on this region so better visual comparison between the modal significance results for the 3 different ground plane sizes can be made.

As shown in Fig. 5.6(a), the modal significance for only modes 1 and 3 is nearing unity, however this is only true in a small part of the frequency range 5.0-11.0 GHz. Similarly, in Fig. 5.6(b), the modal significance for modes 2, 4, 5 and 9 is nearing unity, however this is only true in a small part of the frequency range 5.0-11.0 GHz. In Fig. 5.6(c), the modal significance for modes 1, 3, 5 and 9 is nearing unity over the entire frequency range 5.0-11.0 GHz.

Figure 5.6 clearly demonstrates that as the ground plane size is increased, eigenmodes become more resonant. This is to be expected since smaller ground plane is susceptible to substrate edge diffractions which results in deterioration of the impedance bandwidth. Therefore, a relatively large substrate and ground plane should be sought to achieve higher impedance bandwidth.

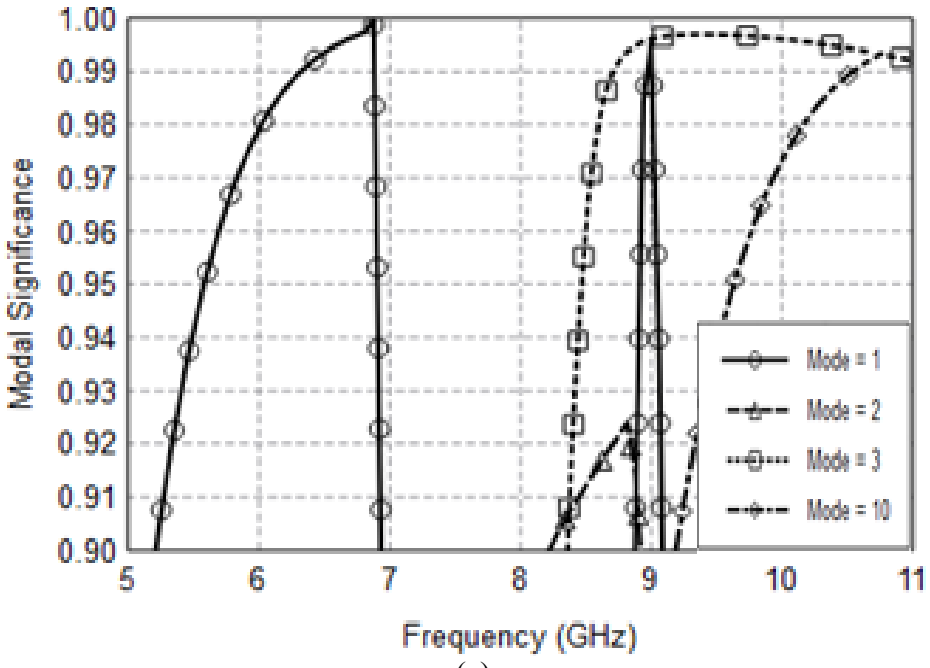

(a)

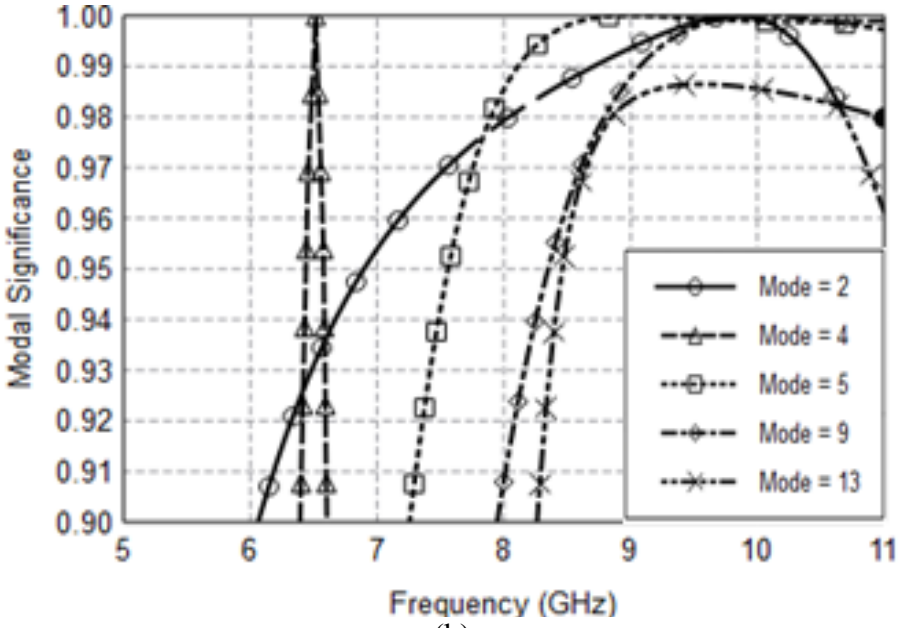

(b)

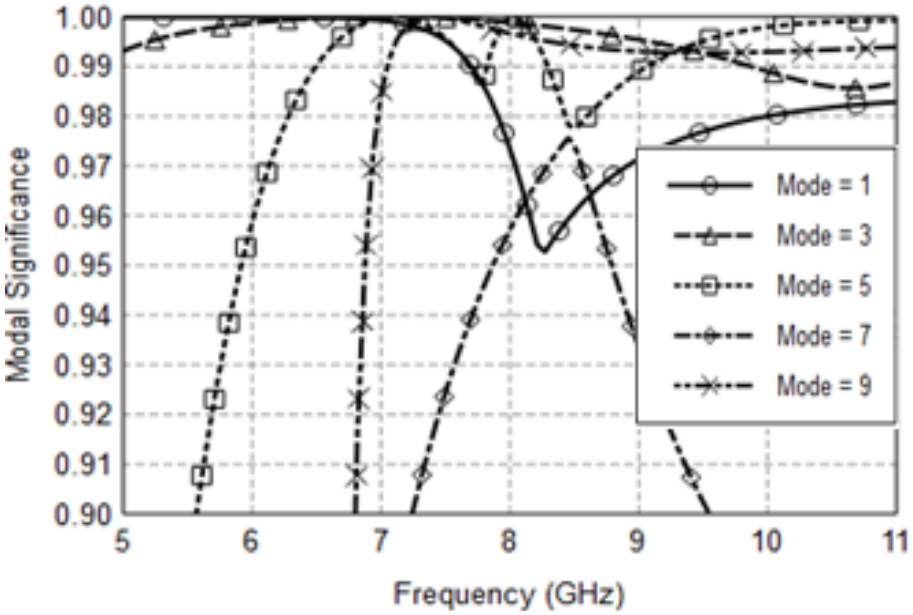

(c)

Fig. 5.6. Modal Significance of rectangular patch with different rectangular ground plane sizes. (a) 11.07mm x 8.33mm (b) 13.87mm x 11.13mm (c) 21.86mm x 19.12mm [87] (© 2016 IEEE)

5.6 Modal Analysis of Excitation Feed Probes

Modal analysis in sections 5.2-5.4 concludes that the U-slot rectangular patch on ε_r = 4.4 substrate is a highly radiating structure. Before modeling this structure with an excitation feed, the eigenmodes resonating on this structure need to be investigated first. In Fig. 5.7, the modal significance of the top 6 significant eigenmodes is shown. It is shown that modes 1, 3, and 4 contribute the most to radiation since their modal significance is close to 1 over the frequency range 2.5-8.5GHz. Higher order modes 5 and 6 contribute minimally in the higher frequencies. So, prospective excitation sources will aim to excite all or some of the resonating eigenmodes (1, 3, and 4) in the antenna structure.

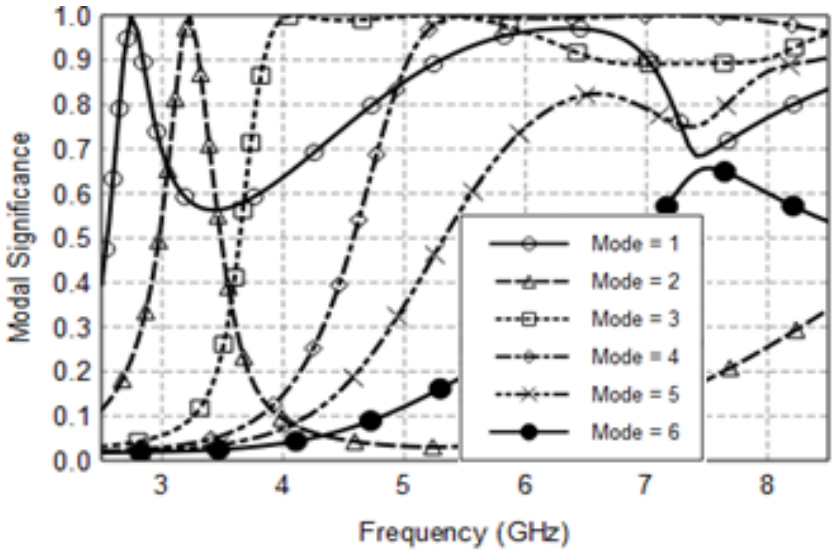

Fig. 5.7. Modal Significance for U-slot patch antenna with ε_r = 4.4 substrate [88] (© 2016 ACES)

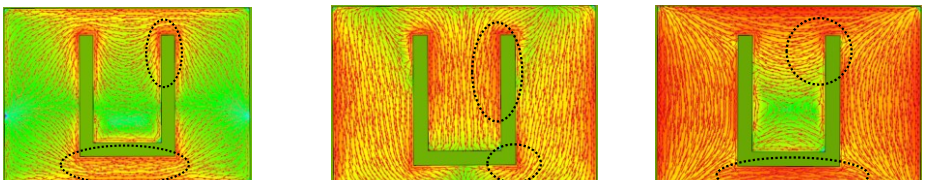

(a) (b) (c)

Fig. 5.8. Characteristic currents of U-slot rectangular patch antenna on $\varepsilon_r = 4.4$ substrate at 5.0 GHz for (a) mode 1 (b) mode 3 (c) mode 4 [88] (© 2016 ACES)

Figure 5.8 shows the characteristic currents for modes 1, 3, and 4 at 5.0 GHz. The location of maximum current distribution, where it is desirable to excite the patch, is denoted by the concentrated red color in Fig. 5.8. The common location for maximum current distribution between all three modes is marked by the dotted black circles in Fig. 5.8 and is found to be at the base of the U-slot and the inner edge of the U-slot arm.

To find an ideal source feed which will excite the most modes, the U-slot rectangular patch antenna, shown in Fig. 2.1, on the $\varepsilon_r = 4.4$ substrate with $\tan(\delta) = 0.02$ is excited with 3 different probe feeds. These are the conventional vertical probe, the L-probe, and the T-probe. The U-slot patch antenna and probe dimensions, designed for a 3.9 GHz design frequency, are shown in Table 5.1 for each of the probes. The probe radius is defined as r_p. The x- and y-axis positions of the probe are defined as x_p and y_p, respectively. The horizontal and vertical arms of the L-probe and T-probe are defined as L_h and L_v, respectively. The horizontal arm of the T-probe is symmetric, i.e. its length on the left side of vertical arm is equal to its length on the right side of vertical arm, which is equal to 3.84mm.

The modal excitation coefficient in Eq. (5.3) is calculated via FEKO solver for each

of the probe feeds. Figure 5.9 shows the modal excitation coefficient of the top modes excited by the 3 different feed probes. The modal excitation coefficient is analyzed over the selected frequency range between 2.5 GHz and 8.5 GHz. Modes with the highest modal excitation coefficient value are the main modes excited by the feed probe. As shown in Fig. 5.9(a), mode 3 is the main mode excited by the conventional vertical probe in the frequency range 2.5-5.7 GHz. In Fig. 5.9(b), mode 3 is the main mode excited by the L-probe in the frequency range 2.5-6.1 GHz. In Fig. 5.9(c), modes 3, 4, and 6 are the main modes excited by the T-probe in the frequency range 2.5-7.0 GHz. Therefore, it is concluded that the T-probe excites the most number of modes over the largest frequency range and hence is expected to achieve the highest impedance bandwidth.

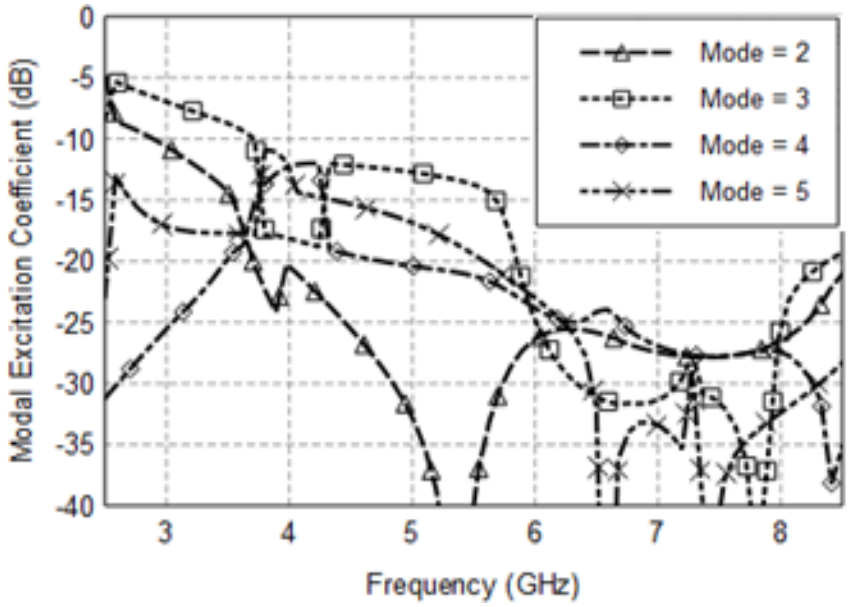

(a)

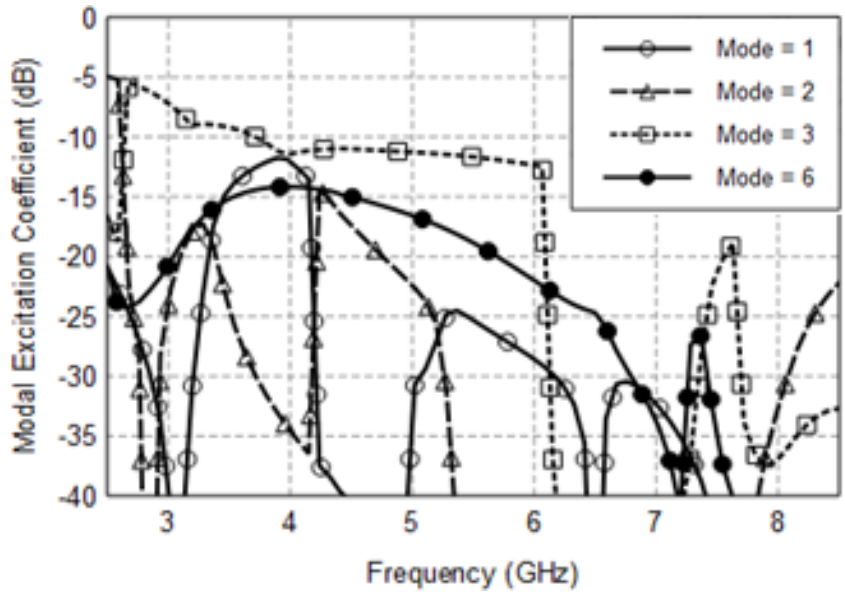

(b)

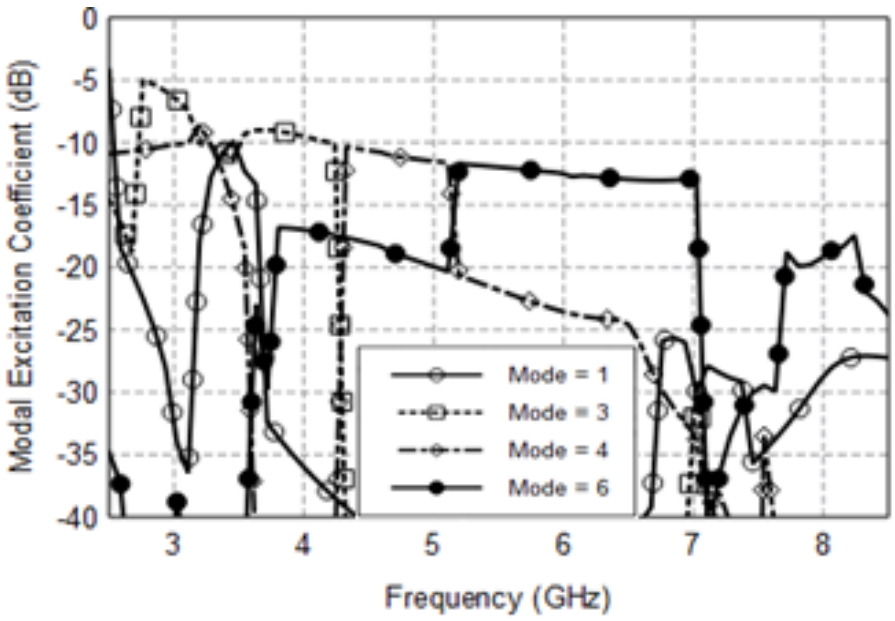

(c)

Fig. 5.9. Modal Excitation Coefficient of U-slot patch antenna with $\varepsilon_r = 4.4$ substrate and different excitation feeds. (a) Conventional vertical feed (b) L-probe feed (c) T-probe feed [89] (© 2016 IEEE)

In Fig. 5.10, the modal significance of each of the three probes is shown. The probe structures are modeled independent of the other antenna elements, i.e. the U-slot patch, substrate, and ground plane. For the vertical probe, in Fig. 5.10(a), mode 1 is the contributing mode maxing out at modal significance equal to 0.08. For the L-probe, in Fig. 5.10(b), mode 1 is the contributing mode maxing out at modal significance close to 0.16. For the T-probe, in Fig. 5.10(c), modes 1 and 2 are the contributing modes maxing out at modal significance close to 0.20. Compared to the other two probes, the T-probe has more modes with higher modal significance which indicates that it is the least reactive feeding structure. This is a desirable feeding structure feature and also explains why the T-probe is expected to achieve the highest impedance bandwidth. The fact that the modal significance of all the probes is relatively low at less than 0.20 indicates that they will not radiate much, which is another desirable feature in feeding structures.

Table 5.1: U-slot patch antenna dimensions in mm for different feed probe designs [88] (© 2016 ACES)

	Vertical Probe (Simulated)	L-Probe (Simulated)	T-Probe (Simulated)	T-Probe (Fabricated)
a	2.25	2.25	2.25	4.38
b	2.25	2.25	2.25	4.38
W	20.25	20.25	20.25	39.48
L	14.62	14.62	14.62	28.51
L_s	10.14	10.14	10.14	19.78
t	1.13	1.13	1.13	2.21
W_s	7.87	7.87	7.87	15.35
W_g	140.17	140.17	140.17	139.41
L_g	134.54	134.54	134.54	128.44
h	7.62	7.62	7.62	15.35
r_p	1	1	1	0.65
x_p	6	4.81	4	10.95

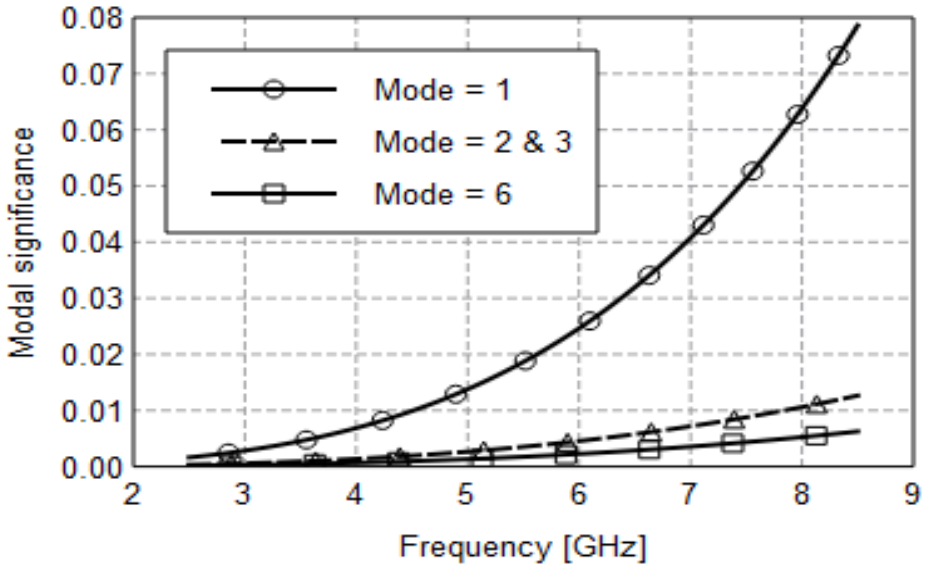
Modal significance
Frequency [GHz]
Mode = 1
Mode = 2 & 3
Mode = 6
0.00
0.01
0.02
0.03
0.04
0.05
0.06
0.07
0.08
2
3
4
5
6
7
8
9

(a)

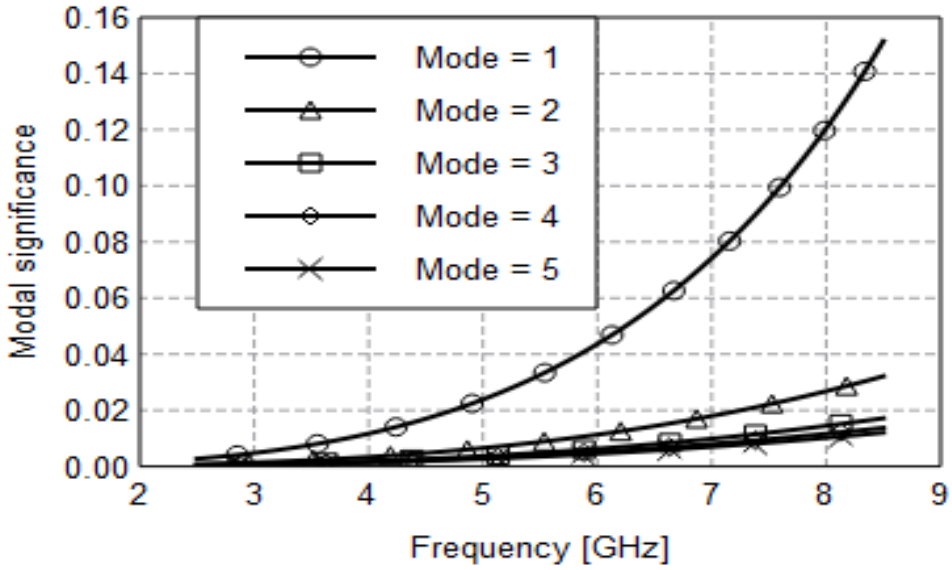
Modal significance
Frequency [GHz]
Mode = 1
Mode = 2
Mode = 3
Mode = 4
Mode = 5
0.00
0.02
0.04
0.06
0.08
0.10
0.12
0.14
0.16
2
3
4
5
6
7
8
9

(b)

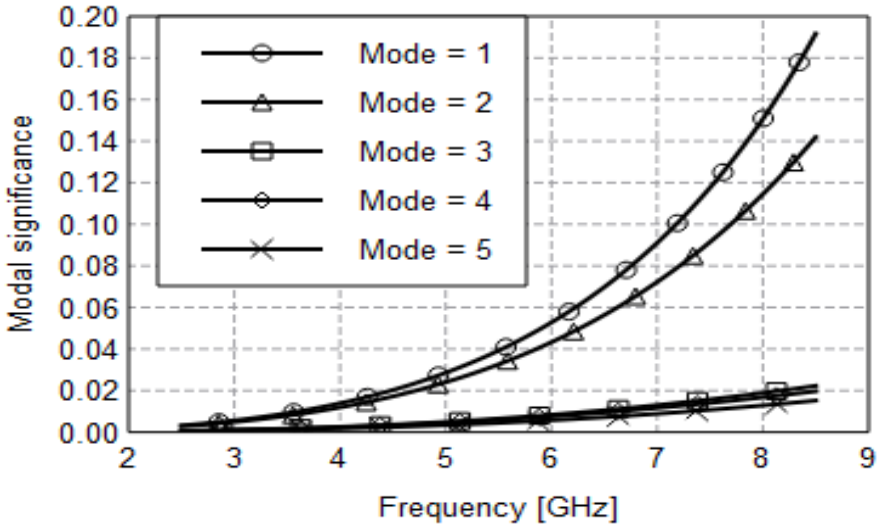

(c)

Fig. 5.10. Modal Significance of different excitation feeds. (a) Conventional vertical feed (b) L-probe feed (c) T-probe feed [88] (© 2016 ACES)

5.7 Optimized Impedance Bandwidth of U-slot Patch Antenna

Figure 5.11 shows the VSWR bandwidth for each of the 3 probes. Results from 3 electromagnetic solvers, namely FEKO MoM, FEKO FEM, and HFSS FEM, are shown for validation purposes. The conventional feed in Fig. 5.11(a) shows VSWR ≤ 2 bandwidth of 21% between 3.55 GHz and 4.38 GHz. The L-probe feed in Fig. 5.11(b) shows VSWR ≤ 2 bandwidth of 82% between 2.74 GHz and 6.58 GHz, and the T-probe feed in Fig. 5.11(c) shows VSWR ≤ 2 bandwidth of 96% between 2.86 GHz and 8.16 GHz. It should be noted that infinite substrate and ground is assumed for the FEKO MoM simulation, whereas finite substrate and ground is assumed for the FEKO FEM and HFSS FEM simulations. This accounts for the slight discrepancy between the MoM and FEM results, otherwise the simulation results of the 3 solvers are in good agreement.

The small substrate thickness of 7.62mm used in the T-probe fed antenna design simulation of Fig. 5.11(c) was not available for fabrication. Also, the horizontal probe arm of the T-probe was modeled as a rectangular PEC sheet sandwiched between two substrate layers due to lack of proper instrumentation to fabricate a T-shaped probe. Therefore, a bigger patch antenna with thicker multilayered substrate, shown in Fig. 5.12, was fabricated for a 2.0 GHz design frequency, instead. The dimensions of the fabricated T-probe fed U-slot patch antenna are shown in the rightmost column of Table 5.1. In Fig. 5.13, measured VSWR bandwidth of over 71% between 1.8 GHz and 3.8 GHz is realized, though bandwidth can be improved between 2.2 and 2.4 GHz. As shown in Fig. 5.13, a higher VSWR bandwidth between 1.8 and 4.8 GHz could be realized if it was not for the oscillations around 2.3, 3.9, and 4.5 GHz. These oscillations are mainly due to the thicker substrate used in fabrication which introduces more surface waves that scatter at substrate edges. Measured and simulated results, in Fig. 5.13, of the fabricated antenna are in good agreement.

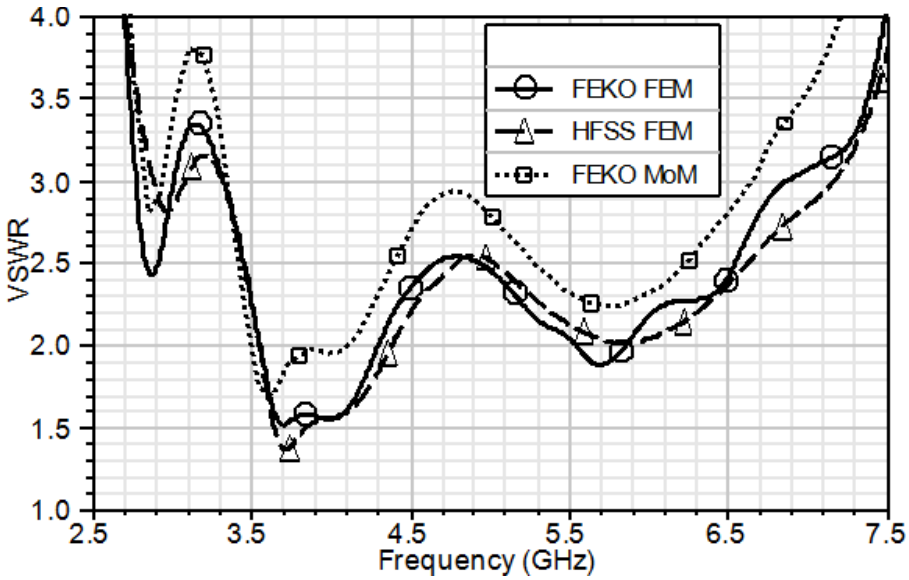

(a)

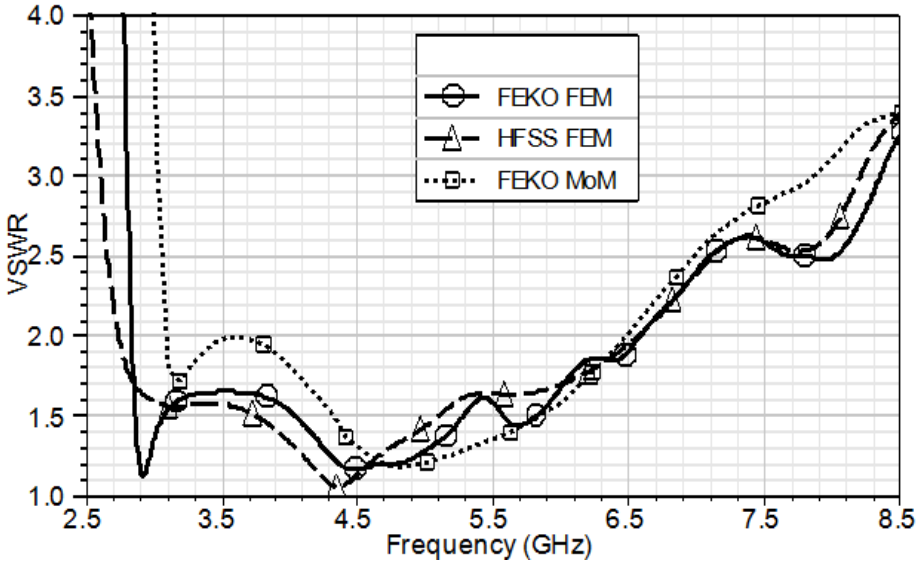

(b)

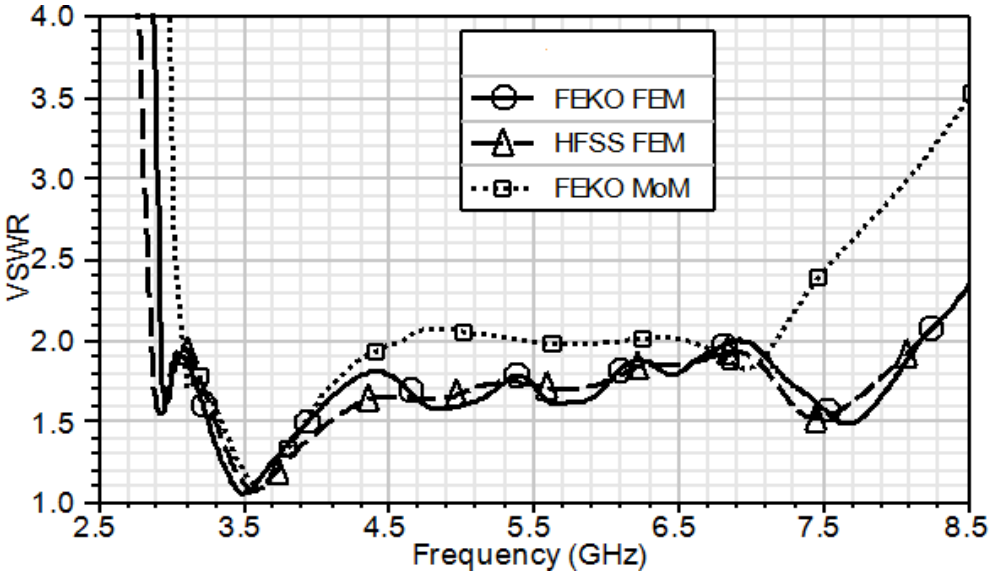

(c)

Fig. 5.11. Simulated VSWR for U-slot patch antenna with different excitation feeds. (a) Conventional vertical feed (b) L-probe feed (c) T-probe feed [88] (© 2016 ACES)

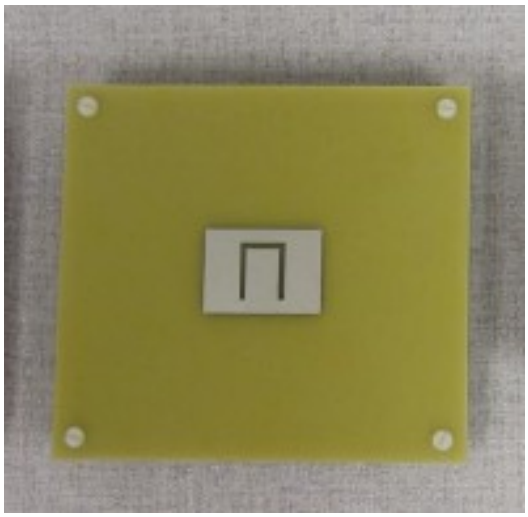

Fig. 5.12. Image of fabricated T-probe fed, U-slot microstrip patch antenna with $\varepsilon_r = 4.4$ substrate [88] (© 2016 ACES)

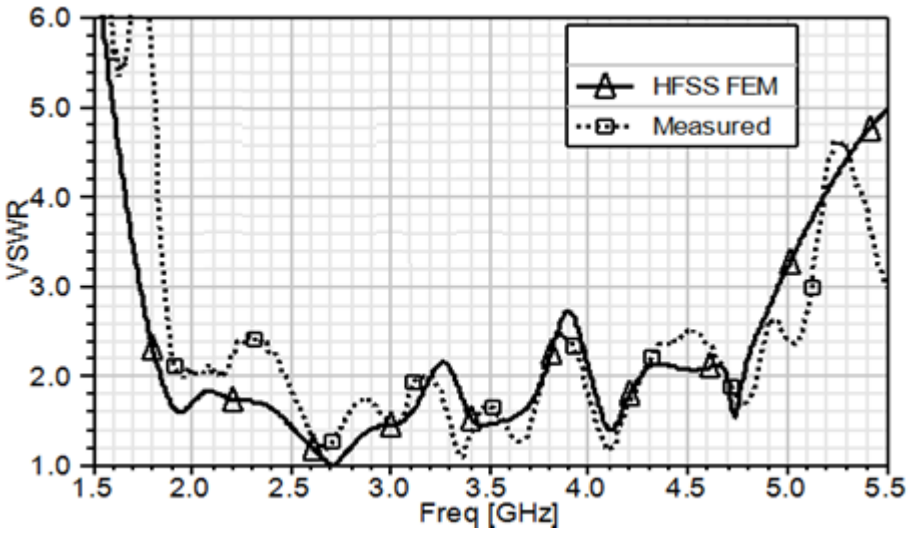

Fig. 5.13. Measured vs simulated VSWR of T-probe fed, U-slot microstrip patch antenna with $\varepsilon_r = 4.4$ substrate [88] (© 2016 ACES)

5.8 Summary

In this chapter, TCM has been used to analyze the resonant behavior of different patch shapes, patch slot geometries, substrate permittivities, ground plane sizes, and excitation feed probes to identify the most resonant structures which contribute significantly to the radiated fields. The analysis concludes that the U-slot rectangular patch on $\varepsilon_r = 4.4$ substrate presents the highest radiating structure. Also, the analysis concludes that larger ground planes contribute more to the resonance behavior of the antenna structure and hence will contribute to achieving higher impedance bandwidth.

Finally, TCM has been used to find the ideal excitation feed to excite the highly radiating structure of the single-layer U-slot rectangular patch on $\varepsilon_r = 4.4$ substrate to achieve the most radiation and impedance bandwidth. Modal analysis of this single-layer structure with different single feed excitations concludes that VSWR ≤ 2 impedance bandwidth in the order of 96% can be achieved with a single T-probe feed. Experimental results show VSWR ≤ 2 impedance bandwidth in the order of 71%.

CHAPTER 6

CONCLUSION AND FUTURE WORK

In this dissertation, ideal L-probe feed dimensions are established through extensive parametric study on ε_r = 2.2 and 4.5 substrates to propose empirical guidelines for the design of L-probe feeds which yield first-pass optimum impedance bandwidth. The established ideal L-probe dimensions are used successfully on other substrates for the design of first-pass L-probe feeds which yield impedance bandwidth over 50%.

Second, the evaluation of the mutual coupling of an L-probe-fed U-slot microstrip patch 2-element array using different patch orientations and U-slot topologies for ε_r = 2.2 and 4.5 substrates is presented. For ε_r = 2.2 substrate, the diamond patch orientation has the least coupling between the array elements, and for ε_r = 4.5 substrate, the E-plane patch orientation has the least coupling. Results indicate that the current density distribution on the microstrip patch has an effect on mutual coupling between the array elements.

Third, the scan element pattern of a 5x5 planar phased array on ε_r = 2.2 substrate using the diamond patch and E-plane patch orientations is characterized. Results show that the diamond patch orientation is the ideal orientation to use in a phased array design since blind spots are less prevalent in the diamond patch orientation with the least mutual coupling and more prevalent in the E-plane patch orientation which has the most mutual coupling between the array elements.

Fourth, sidelobe reduction using nonuniform excitation and inter-element spacing in a wideband U-slot microstrip patch phased arrays is examined. Results show a sidelobe reduction by at least -10dB when nonuniform excitation and nonuniform inter-element

spacing are used as opposed to using nonuniform excitation only or nonuniform spacing only.

Lastly, the Theory of Characteristic Modes has been used to analyze the resonant behavior of different patch shapes, patch slot geometries, substrate permittivities, ground plane sizes, and excitation feed probes to identify the most resonant structures which contribute significantly to the radiated fields. The modal analysis concludes that the U-slot rectangular patch on $\varepsilon_r = 4.4$ substrate presents the highest radiating structure. Also, the analysis concludes that larger ground planes contribute more to the resonance behavior of the antenna structure and hence will contribute to achieving higher impedance bandwidth. Modal analysis of this single-layer structure with different single feed excitations realizes impedance bandwidth of 96% with a single T-probe feed. Experimental results show impedance bandwidth of 71%.

Future work will explore the following research areas:

1. Establish ideal dimensions for other microstrip patch antenna feeds using the same parametric approach used in this dissertation.
2. Explore other means to reduce the scan blindness and sidelobes in a phased array.
3. Utilize the Theory of Characteristic Modes to analyze the resonant behavior of other microstrip patch shapes, patch slot geometries, and excitation feeds.
4. Apply the same methodology used on microstrip patch antennas on other antenna types by identifying their individual resonant structures, using the Theory of Characteristic Modes, which when combined with other identified resonant structures will yield high impedance bandwidth antennas.

APPENDIX A

A. MATLAB CODE

This appendix presents the MATLAB code used to calculate the dimensions of the U-slot rectangular microstrip patch antenna using the method of dimensional invariance. Also, the MATLAB code used to calculate the antenna's fidelity in section 2.3 is presented. Finally, the MATLAB code used to calculate the nonuniform element spacing in the 17-element linear array in section 4.2 is presented.

A.1. MATLAB Code for the Method of Dimensional Invariance [41]

```
%%%%Input Parameters%%%%%
eps_r = 4.4;                    % substrate permittivity
f_r = 8.0*(10^9);               % design frequency
h = 1.0;                        % substrate thickness
pi = 3.14159;
c = 2.99*10^11;
f_r0 = (1.25*f_r);
lam = c/f_r;
C = h/lam;
L = c/(2*f_r0*sqrt(eps_r));     % rectangular patch length
W = 1.385*L;                    % rectangular patch width
W_out = ((eps_r + 1)/2)+((eps_r - 1)/(2*sqrt(1+(10*h/W))));
L_out = ((eps_r + 1)/2)+((eps_r - 1)/(2*sqrt(1+(10*h/L))));
del_L = ((0.412*h)*(W_out+0.3)*((W/h) + 0.264))/((W_out-0.258)*((W/h)+0.8));
f_H = c/(2*(L+del_L)*sqrt(eps_r))
x = ((h/L)*(0.882+(0.164*(eps_r-
1)/(eps_r*eps_r))))+(((eps_r+1)/(pi*eps_r))*(0.758+log(1.88+L/h)));
f_J = (f_r0*eps_r)/((1+x)*sqrt(W_out*L_out))

% Calculation of the upper and lower limits of the design frequency
while ((f_r >= min(f_H,f_J)) && (f_r <= max(f_H,f_J))) == 0
   fprintf('entered while\n');
   if f_r < min(f_H,f_J)
      fprintf('entered f_r < min(f_H,f_J)');
      f_r0 = f_r0-(0.05*f_r);
      L = c/(2*f_r0*sqrt(eps_r));
      W = 1.385*L;
      W_out = ((eps_r + 1)/2)+((eps_r - 1)/(2*sqrt(1+(10*h/W))));
      L_out = ((eps_r + 1)/2)+((eps_r - 1)/(2*sqrt(1+(10*h/L))));
```

```
        del_L = ((0.412*h)*(W_out+0.3)*((W/h) + 0.264))/((W_out-0.258)*((W/h)+0.8));
        f_H = c/(2*(L+del_L)*sqrt(eps_r))
        x = ((h/L)*(0.882+(0.164*(eps_r-
1)/(eps_r*eps_r))))+(((eps_r+1)/(pi*eps_r))*(0.758+log(1.88+L/h)));
        f_J = (f_r0*eps_r)/((1+x)*sqrt(W_out*L_out))
    elseif (f_r > max(f_H,f_J))
        fprintf('entered f_r > max(f_H,f_J)');
        f_r0 = f_r0+(0.05*f_r);
        L = c/(2*f_r0*sqrt(eps_r));
        W = 1.385*L;
        W_out = ((eps_r + 1)/2)+((eps_r - 1)/(2*sqrt(1+(10*h/W))));
        L_out = ((eps_r + 1)/2)+((eps_r - 1)/(2*sqrt(1+(10*h/L))));
        del_L = ((0.412*h)*(W_out+0.3)*((W/h) + 0.264))/((W_out-0.258)*((W/h)+0.8));
        f_H = c/(2*(L+del_L)*sqrt(eps_r))
        x = ((h/L)*(0.882+(0.164*(eps_r-
1)/(eps_r*eps_r))))+(((eps_r+1)/(pi*eps_r))*(0.758+log(1.88+L/h)));
        f_J = (f_r0*eps_r)/((1+x)*sqrt(W_out*L_out))
    end
end
L_1= L;

%%%%%%%%%% Dimensions of the U-slot %%%%%%%%%%%
if eps_r <= 1
    W_s = W/3.203;
    L_s = W_s/0.835;
    t = W_s*0.13;
    b = L_s/4.237;
elseif eps_r > 1 && eps_r <= 3
    W_s = W/2.573;
    L_s = W_s/0.777;
    t = W_s*0.144;
    b = L_s/4.5;
elseif eps_r > 3 && eps_r <= 5
    W_s = W/2.573;
    L_s = W_s/0.776;
    t = W_s*0.144;
    b = L_s/4.51;
else
    W_s = W/2.574;
    L_s = W_s/0.777;
    t = W_s*0.144;
    b = L_s/4.48;
end
F = L/2;
```

A.2 MATLAB Code for Cross-correlation Calculation of Pulse Signals

```
% The cross-correlation of the pulse signals to evaluate the antenna fidelity
resp = resp_theta_45_phi_90;

pulse2 = pulse/sqrt(sum(pulse.^2));
resp2 = resp/sqrt(sum(resp.^2));
cross_corr = xcorr(pulse2,resp2);


disp('cross_corr ='); disp(cross_corr);
disp('max ='); disp(max(cross_corr));

figure (1); plot (pulse);
figure (2); plot (resp);
figure (3); plot (cross_corr);
```

A.3 MATLAB Code for Nonuniform Element Spacing Calculation

main.m:

```
N = 24;                 % number of elements
K = 4;                  % number of sidelobes reduced
A = 0.00786;            % amount of reduction          A=0.00786 for 24-element (-42dB)

for n=1:2:N-1
  eta_n = 2*A*((N/pi)^3)*sll_summ(n, K, N);
  disp('eta'); disp(n); disp(eta_n);
end
```

sll_summ.m:

```
function [sll_sum] = sll_summ(n, K, N)

sll_sum = 0;

for k=1:K
    a = (-1)^k;
    b = (2*k)+1;
    c = sin((n*pi)/(2*N)*b);
    d = c/(b^2);
    sll_sum = sll_sum + (a*d);
end
```

REFERENCES

[1] B. Allen, M. Dohler, E. E. Okon, W. Q. Malik, A. K. Brown and D. J. Edwards, *Ultra-wideband antennas and propagation*, Wiley, New York, pp. 1-5, 2007.

[2] R. S. Kshetrimayum, "An introduction to UWB communication systems," *IEEE Potentials*, vol. 28, no. 2, pp. 9-13, March-April, 2009.

[3] S. H. Choi, J. K. Park, S. K. Kim, and J. Y. Park , "A new ultra-wideband antenna for UWB applications," *Microwave and Optical Technology Letters*, vol. 40, no. 5, pp. 399-401, March 5, 2004.

[4] L. Guo, S. Wang, X. Chen, and C. G. Parini, "Study of compact antenna for UWB applications," *Electronics Letters*, vol. 46, no. 2, pp. 115-116, January 21, 2010.

[5] C. Sim, W. Chung, and C. Lee, "Compact slot antenna for UWB applications," *IEEE Antennas and Wireless Propagation Letters*, vol. 9, pp. 63-66, 2010.

[6] A. A. L. Neyestanak, "Ultra wideband rose leaf microstrip patch antenna," *Progress In Electromagnetics Research*, vol. 86, pp. 155-168, 2008.

[7] M. N. Shakib, M. T. Islam and N. Misran, "Stacked patch antenna with folded patch feed for ultrawideband application," *IET Microwave Antennas and Propagation*, vol. 4, no. 10, pp. 1456-1461, 2010.

[8] R. Zaker and A. Abdipour, "A very compact ultrawideband printed omnidirectional monopole antenna," *IEEE Antenna and Wireless Propagation Letters*, vol. 9, pp. 471-473, June 2010.

[9] Q. Wu, R. Jin, J. Geng, and M. Ding, "Printed omni-directional UWB monopole antenna with very compact size," *IEEE Transactions on Antennas and Propagation*, vol. 56, no. 3, pp. 896–899, Mar. 2008.

[10] J. Jung, W. Choi, and J. Choi, "A small wideband microstrip-fed monopole antenna," *IEEE Microwave Wireless Components Letters*, vol. 15, no. 10, pp. 703–705, Oct. 2005.

[11] R. Azim, M.T. Islam, and N. Misran, "Compact tapered-shape slot antenna for UWB applications," *IEEE Antennas Wireless Propagation Letters*, vol. 10, pp. 1190–1193, 2011.

[12] N. Chahat, M. Zhadobov, R. Sauleau, and K. Ito, "A compact UWB antenna for on-body applications," *IEEE Transactions on Antennas and Propagation*, vol. 59, no. 4, pp. 1123–1131, April 2011.

[13] S. A. Hosseini, Z. Atlasbaf, and K. Forooraghi, "A compact ultra wide band (UWB) planar antenna using glass as substrate," *Journal of Electromagnetic Waves and Applications*, vol. 22, no. 1, pp. 47 59, Jan. 2008.

[14] G. A. Deschamps, "Microstrip microwave antennas," *Proc. 3rd USAF Symposium on Antennas*, 1953.

[15] R. E. Munson, "Conformal microstrip antennas and microstrip phased arrays," *IEEE Transactions on Antennas and Propagation*, vol. AP-22, pp. 74-78, 1974.

[16] J. Q. Howell, "Microstrip antennas," *IEEE Transactions on Antennas and Propagation*, vol. AP-23, pp. 90-93, January 1975.

[17] R. Garg, P. Bhartia, I. Bahl, A. Ittipiboon, *Microstrip Antenna Design Handbook*, Artech House, Norwood, MA, 2001.

[18] D. Gibbins, M. Klemm, I.J. Craddock, J.A. Leendertz, A. Preece, and R. Benjamin, "A comparison of a wide-slot and a stacked patch antenna for the purpose of breast cancer

detection," *IEEE Transactions on Antennas and Propagation*, vol. 58, no. 3, pp. 665-674, March 2010.

[19] M. Bassi, M. Caruso, M.S. Khan, A. Bevilacqua, A.D. Capobianco, and A. Neviani, "An integrated microwave imaging radar with planar antennas for breast cancer detection," *IEEE Transactions on Microwave Theory and Techniques*, vol. 61, no. 5, pp. 2108-2118, May 2013.

[20] H. M. Jafari, W. Liu, S. Hranilovic, and M. J. Deen, "Ultrawideband radar imaging system for biomedical applications," *Journal of Vacuum Science & Technology*, vol. 24, no. 3, pp. 752-757, May 2006.

[21] W. Liu, H.M. Jafari, S. Hranilovic, and M.J. Deen, "Time domain analysis of UWB breast cancer detection," *IEEE 23rd Biennial Symposium on Communications*, pp. 336-339, 2006.

[22] X. Zhuge, M. Hajian, A. G. Yarovoy, and L. P. Ligthart, "Ultra-wideband imaging for detection of early-stage breast cancer," *IEEE Proceedings of the European Radar Conference (EuRAD)*, pp. 39-42, October 10-12, 2007.

[23] E. C. Fear and M. A. Stuchly, "Microwave detection of breast cancer: a study of tumor response variations," *IEEE Proceedings of the 22nd Annual International Conference in Engineering in Medicine and Biology Society (EMBS)*, pp. 74-77, July 23-28, 2000.

[24] S. Adnan, "A compact UWB antenna design for breast cancer detection," *PIERS Online*, vol. 6, no. 2, pp. 129-132, 2010.

[25] R. Nilavalan, I.J. Craddock, A. Preece, J. Leendertz and R. Benjamin, "Wideband microstrip patch antenna design for breast cancer tumour detection," *IET Microwave Antennas Propagation*, vol. 1, no. 2, pp. 277-281, 2007.

[26] H. Kanj and M. Popovic, "A novel ultra-compact broadband antenna for microwave breast tumor detection," *Progress In Electromagnetics Research (PIER) vol. 86, pp. 169–198, 2008.*

[27] X. Chen, J. Liang, S. Wang, Z. Wang and C. Parini, "Small ultra wideband antennas for medical imaging," *2008 Loughborough Antennas & Propagation Conference*, pp. 28-31, 17-18 March 2008.

[28] G. Kumar and K. P. Ray, *Broadband Microstrip Antennas*, Artech House, Norwood, MA, 2003.

[29] W. L. Stutzman and G. A. Thiele, *Antenna Theory and Design*, 3rd Edition, Wiley, New York, 2013.

[30] Y. X. Guo, K. M. Luk and K. F. Lee, "U-slot circular patch antennas with L-probe feeding," *Electronics Letters*, vol. 35, no. 20, pp. 1694-1695, September 1999.

[31] Y.X. Guo, C.L. Mak, K.M. Luk and K.F. Lee, "Analysis and design of L-Probe proximity fed-patch antennas," *IEEE Transactions on Antennas and Propagation*, vol. 49, no. 2, pp. 145-149, February 2001.

[32] C. L. Mak, K. F. Lee, and K. M. Luk, "Broadband patch antenna with a T-shaped probe*," IEE Proceedings Microwaves Antennas and Propagation*, vol. 147, no. 2, pp. 73-76, 2000.

[33] R. Garg, *Analytical and Computational Methods in Electromagnetics*, Artech House, Norwood, MA, 2008.

[34] M. N. O. Sadiku, *Numerical Techniques in Electromagnetics with MATLAB*, 3rd Edition, CRC Press, Boca Raton, FL, 2009.

[35] A. Foudazi, H. R. Hassani, and S. M. Nezhad, "Small UWB planar monopole antenna with added GPS/GSM/WLAN bands," *IEEE Transactions on Antennas and Propagation*, vol. 60, no. 6, pp. 2987-2992, June 2012.

[36] H-D. Chen, C-Y-D. Sim, J-Y. Wu, and T-W. Chiu, "Broadband high-gain microstrip array antennas for WiMAX base station," *IEEE Transactions on Antennas and Propagation*, vol. 60, no. 8, pp. 3977-3980, August 2012.

[37] V. P. Sarin, N. Nassar, V. Deepu, C. K. Aanandan, P. Mohanan, and K. Vasudevan, "Wideband printed microstrip antenna for wireless communications," *IEEE Antennas and Wireless Propagation Letters*, vol. 8, pp.779-781, 2009.

[38] K. F. Lee, S. L. S. Yang, A. A. Kishk, and K. M. Luk, "The versatile U-slot patch antenna," *IEEE Antennas and Propagation Magazine*, vol. 52, no. 1, pp. 71-88, February 2010.

[39] K. F. Lee and K. M. Luk, *Microstrip Patch Antennas*, Imperial College Press, pp. 255-274, 2011.

[40] K. M. Luk, K. F. Lee, and H. W. Lai, "Development of wideband L-Probe couple patch antenna," *Applied Computational Electromagnetics Society (ACES) Journal*, vol. 22, no. 1, pp. 88-96, March 2007.

[41] V. Natarajan and D. Chatterjee, "An empirical approach for design of wideband, probe-fed, U-slot microstrip patch antennas on single-layer, infinite, grounded substrates," *Applied Computational Electromagnetics Society (ACES) Journal*, vol. 18, no. 3, pp. 191-201, November 2003.

[42] V. Natarajan and D. Chatterjee, "Comparative evaluation of some empirical design techniques for CAD optimization of wideband U-slot microstrip antennas," *Applied*

Computational Electromagnetics Society (ACES) Journal, vol. 20, no. 1, pp. 50-69, March 2005.

[43] R. D. Hofer, D. E. Oliver, and D. Chatterjee, "Analysis of U-slot, microstrip phased array radiator elements on electrically thick substrates," *IEEE Antennas and Propagation Society International Symposium*, pp. 3648-3651, June 9-15, 2007.

[44] M.M. Elsewe, V.K. Dandu, and D. Chatterjee, "Assessment of computational fidelity of MoM and FEM solvers for characterizing a class of UWB microstrip antennas: single-element case," *29th Annual Review of Progress in Applied Computational Electromagnetics*, Monterey, CA, pp. 393-398, March 24-28, 2013.

[45] M. M. Elsewe, V. K. Dandu, and D. Chatterjee, "Ultra-wideband low profile, U-slot microstrip patch antennas: L-probe feed design guidelines," *Applied Computational Electromagnetics Society (ACES) Journal*, vol. 31, no. 11, pp. 1322-1329, November 2016.

[46] FEKO. *Time Analysis of UWB Antennas*. [Online],Available: http://www.feko.info/applications/white- papers/time-analysis-of-UWB-antenna/uwb-monopole-antenna

[47] L. Bao-ping and W. Yang, "Characteristic investigation impulse radiation of two UWB antennas," *Proceedings of the Third International Symposium on Computer Science and Computational Technology*, Jiaozuo, P.R. China, pp. 116-119, August 14-15, 2010.

[48] C. Furse, "A survey of phased arrays for medical applications," Applied Computational Electromagnetics Society (ACES) Journal, vol. 21, no. 3, pp. 365-379, November 2006.

[49] P. T. Nguyen, A. Abbosh, and S. Crozier, "Microwave hyperthermia for breast cancer treatment using electromagnetic and thermal focusing tested on realistic breast models

and antenna arrays," *IEEE Transactions on Antennas and Propagation,* vol. 63, no. 10, pp. 4426-4434, October 2015.

[50] T. Lambard, O. Lafond, M. Himdi, H. Jeuland, S. Bolioli, L. Le Coq, "Ka-band phased array antenna for high-data-rate SATCOM," *IEEE Antennas and Wireless Propagation Letters*, vol. 11, pp. 256-259, 2012.

[51] C.M. Krowne, "E-plane coupling between two rectangular microstrip antennas," *Electronic Letters*, vol. 16, no. 16, pp. 635-636, 31 July 1980.

[52] R. Q. Lee, T. Talty, K. F. Lee, "Mutual coupling between electromagnetically coupled rectangular patch antennas," *Electronics Letters*, vol. 27, no. 6, pp. 532-533, 14 March 1991.

[53] T. Huynh, K. F. Lee, S. R. Chebolu, and R. Q. Lee, "Mutual coupling between rectangular microstrip patch antennas," Microwave and Optical Technology Letters, vol. 5, no. 11, pp. 572-576, October 1992.

[54] K. Hosseini and Z. Atlasbaf, "Mutual coupling between two Microstrip patch antennas on a singly curved surface," *IEEE Antennas and Wireless Propagation Letters*, vol. 12, pp. 313-316, 2013.

[55] D. Chatterjee, "Numerical modeling of scan behavior of finite planar arrays of wideband U-slot and rectangular microstrip patch elements," *Proceedings of IEEE International Symposium on Phased Array Systems and Technology*, Boston, MA, pp. 323-328, October 14-17, 2003.

[56] M. M. Elsewe, V. K. Dandu, and D. Chatterjee, "Assessment of computational fidelity of MoM and FEM solvers for characterizing a class of UWB microstrip antennas: 2-

element case," *29th Annual Review of Progress in Applied Computational Electromagnetics*, Monterey, CA, pp. 399-404, March 24-28, 2013.

[57] M. M. Elsewe and D. Chatterjee, "Mutual coupling characterization of ultra-wideband U-slot microstrip patch array antennas," *Applied Computational Electromagnetics Society (ACES) Express Journal*, vol. 1, no. 1, pp. 36-39, January 2016.

[58] R. C. Hansen, *Phased Array Antennas*, 2nd Edition, Wiley, New York, 2009.

[59] R. J. Mailloux, *Phased Array Antenna Handbook*, 2nd Edition, Artech House, Boston, 2005.

[60] R. F. Harrington, "Sidelobe reduction by nonuniform element spacing," *IEEE Transactions on Antennas and Propagation*, vol. AP-9, pp. 187-192, March 1961.

[61] F. H. Hodjat and S. A. Hovanessian, "Nonuniformly spaced linear and planar array antennas for sidelobe reduction," *IEEE Transactions on Antennas and Propagation,* vol. AP-26, no. 2, pp. 198-204, March 1978.

[62] B. P. Kumar and G. R. Branner, "Design of unequally spaced arrays for performance improvement," *IEEE Transactions on Antennas and Propagation*, vol. 47, no. 3, pp. 511-523, March 1999.

[63] A. Ishimaru, "Unequally spaced arrays based on the poisson sum formula," *IEEE Transactions on Antennas and Propagation*, vol. 62, no. 4, pp. 1549-1554, April 2014.

[64] M. M. Elsewe and D. Chatterjee, "Scan behavior of U-slot microstrip patch phased array antennas," *2014 IEEE Antennas and Propagation Society International Symposium (APSURSI)*, Memphis, TN, pp. 935-936, July 6-11, 2014.

[65] M. M. Elsewe and D. Chatterjee, "Analysis of nonuniform excitation and element spacing in sidelobe reduction of wideband U-slot microstrip patch phased array

antennas," *2015 IEEE International Symposium on Antennas and Propagation & USNC/URSI National Radio Science Meeting*, Vancouver, BC, pp. 1858-1859, July 19-24, 2015.

[66] G. Rafi and L. Shafai, "Broadband microstrip patch antenna with V-slot," *IEE Proceedings Microwaves Antennas and Propagation*, vol. 151, no. 5, pp. 435-440, 2004.

[67] R. J. Chitra, K. Jeyanthi, and V. Nagarajan, "Design of E slot rectangular microstrip slot antenna for WiMAX application," *IEEE Intl. Conf. on Comm. And Signal Processing,* India, pp. 1048-1052, Apr. 3-5, 2013.

[68] R. F. Harrington and J. R. Mautz, "Theory of characteristic modes for conducting bodies," *IEEE Transactions on Antennas and Propagation*, vol. AP-19, no. 5, pp. 622–628, Sept. 1971.

[69] M. Vogel, G. Gampala, D. Ludick, U. Jakobus, and C.J. Reddy, "Characteristic mode analysis: putting physics back into simulation," *IEEE Antennas Propagation Magazine*, vol. 57, no. 2, pp. 307-317, Apr. 2015.

[70] R. F. Harrington and J. R. Mautz, "Computation of characteristic modes for conducting bodies," *IEEE Transactions on Antennas and Propagation*, vol. AP-19, no. 5, pp. 629–639, Sep. 1971.

[71] R. J. Garbacz and D. M. Pozar, "Antenna shape synthesis using characteristic modes," *IEEE Transactions on Antennas and Propagation*, vol. 30, no. 3, pp. 340–350, May 1982.

[72] M. Cabedo-Fabres, E. Antonino-Daviu, A. Valero-Nogueira, and M. Ferrando-Bataller, "The theory of characteristic modes revisited: a contribution to the design of antennas

for modern applications," *IEEE Antennas Propagation Magazine*, vol. 49, no. 5, pp. 52–68, Oct. 2007.

[73] E. Antonino-Daviu, M. Cabedo-Fabres, M. Ferrando-Bataller, and V. M. R. Penarrocha, "Modal analysis and design of band-notched UWB planar monopole antennas," *IEEE Transactions on Antennas and Propagation*, vol. 58, no. 5, pp. 1457-1467, May 2010.

[74] M. Ferrando-Bataller, E. Antonino-Daviu, M. Cabedo-Fabres, and A. Valero-Nogueira, "UWB antenna design based on modal analysis," *3rd European Conference on Antennas and Propagation*, Berlin, pp. 3530–3534, Mar. 23-27, 2009.

[75] M. Capek, P. Hamouz, P. Hazdra, and J. Eichler, "Implementation of the Theory of Characteristic Modes in MATLAB," *IEEE Antennas Propagation Magazine*, vol. 55, no. 2, pp. 176-189, Apr. 2013.

[76] Y. Chen and C. Wang, "Characteristic-Mode-Based improvement of circularly polarized U-slot and E-Shaped patch antennas," *IEEE Antennas Propagation Letters*, vol. 11, pp. 1474-1477, 2012.

[77] Y. Chen and C. Wang, "Electrically small UAV antenna design using characteristic modes," *IEEE Transactions on Antennas and Propagation*, vol. 62, no. 2, pp. 535-545, Feb. 2014.

[78] A. Araghi and G. Dadashzadeh, "Detail-oriented design of a dual-mode antenna with orthogonal radiation patterns utilizing Theory of Characteristic Modes," *Applied Computational Electromagnetics Society (ACES) Journal*, vol. 28, no. 10, pp. 952-959, Oct. 2013.

[79] A. Araghi and G. Dadashzadeh, “Oriented design of an antenna for MIMO applications using Theory of Characteristic Modes,” *IEEE Antennas Wireless Propagation Letters*, vol. 11, pp. 1040–1043, Sep. 2012.

[80] B. A. Austin and K. P. Murray "The application of characteristic mode techniques to vehicle-mounted NVIS antennas", *IEEE Antennas Propagation Magazine*, vol. 40, no. 1, pp. 7 -21, 1998.

[81] M. Cabedo-Fabres, “Systematic design of antennas using the theory of characteristic modes,” *Ph.D. dissertation*, Univ. Politecnica de Valencia, Valencia, Spain, 2007.

[82] E. Antonino, C. A. Suarez, M. Cabedo, and M. Ferrando, “Wideband antenna for mobile terminals based on the handset PCB resonance,” *Microwave and Optical Technology Letters*, vol. 48, no. 7, pp. 1408–1411, Jul. 2006.

[83] M. Khan and D. Chatterjee, “Characteristic mode analysis of a class of empirical design techniques for probe-fed, U-slot microstrip patch antennas,” *IEEE Transactions on Antennas and Propagation*, vol. 64, no. 7, pp. 2758-2770, July 2016.

[84] A. El-Hajj, K. Y. Kabalan, and A. Rayes, "Characteristic mode formulation of multiple rectangular apertures in a conducting plane with a dielectric-filled cavity," *IEEE Transactions on Electromagnetic Compatibility*, vol. 40, no. 2, pp.89-93, May, 1998.

[85] M. M. Elsewe and D. Chatterjee, “Modal analysis of patch slot designs in microstrip patch antennas,” 2016 IEEE International Conference on Wireless Information Technology and Systems (ICWITS) and Applied Computational Electromagnetics (ACES), Honolulu, HI, pp. 1-2, March 13-17, 2016.

[86] M. M. Elsewe and D. Chatterjee, “Modal analysis of substrate permittivities in microstrip patch antennas,” 2016 IEEE International Conference on Wireless

Information Technology and Systems (ICWITS) and Applied Computational Electromagnetics (ACES), Honolulu, HI, pp. 1-2, March 13-17, 2016.

[87] M. M. Elsewe and D. Chatterjee, "Characteristic mode analysis of ground plane size in microstrip patch antennas," *2016 IEEE International Symposium on Antennas and Propagation & USNC/URSI National Radio Science Meeting*, Fajardo, Puerto Rico, pp. 429-430, June 26-July 1, 2016.

[88] M. M. Elsewe and D. Chatterjee, "Ultra-wide bandwidth enhancement of single-layer single-feed patch antenna using the Theory of Characteristic Modes," *Applied Computational Electromagnetics Society (ACES) Express Journal*, accepted November, 2016.

[89] M. M. Elsewe and D. Chatterjee, "Characteristic mode analysis of excitation feed probes in microstrip patch antennas," *2016 IEEE International Symposium on Antennas and Propagation & USNC/URSI National Radio Science Meeting*, Fajardo, Puerto Rico, pp. 33-34, June 26-July 1, 2016.

[90] Y. Chen and C. Wang, *Characteristic Modes: Theory and Applications in Antenna Engineering*. Hoboken, NJ, USA: Wiley, 2015.

VITA

Mohamed M. Elsewe was born on November 19, 1975 in Medina, Saudi Arabia. He received his Bachelor's degree in Biochemistry and Chemistry from the University of Kansas in 1996. Then, he went on to receive a Bachelor in Computer Information Systems from Ottawa University in 2001. He received his Master's degree in Electrical Engineering from the University of Missouri – Columbia in 2002.

Mohamed works as an Engineering manager at Primus Diagnostics in Kansas City, Missouri, from April 2003 until present.

Mohamed pursued an Interdisciplinary PhD degree at the University of Missouri – Kansas City. His primary PhD discipline is Electrical and Computer Engineering. His co-discipline is Telecommunications and Computer Networking. His research interests are in the areas of ultra-wideband microstrip patch antennas and phased arrays. His research focus is in microstrip patch antenna design guidelines and microstrip antenna array scan performance enhancement.

Mohamed is a member of the Institute of Electrical and Electronic Engineers (IEEE) and the Applied Computational Electromagnetics Society (ACES). A list of his conference and journal publications is provided below:

M. M. Elsewe and D. Chatterjee, "Ultra-wide bandwidth enhancement of single-layer single-feed patch antenna using the Theory of Characteristic Modes," *Applied Computational Electromagnetics Society (ACES) Express Journal*, accepted November, 2016.

M. M. Elsewe, V. K. Dandu, and D. Chatterjee, “Ultra-wideband low profile, U-slot microstrip patch antennas: L-probe feed design guidelines,” *Applied Computational Electromagnetics Society (ACES) Journal*, vol. 31, no. 11, pp. 1322-1329, November 2016.

M. M. Elsewe and D. Chatterjee, "Characteristic mode analysis of ground plane size in microstrip patch antennas," *2016 IEEE International Symposium on Antennas and Propagation & USNC/URSI National Radio Science Meeting*, Fajardo, Puerto Rico, pp. 429-430, June 26-July 1, 2016.

M. M. Elsewe and D. Chatterjee, "Characteristic mode analysis of excitation feed probes in microstrip patch antennas," *2016 IEEE International Symposium on Antennas and Propagation & USNC/URSI National Radio Science Meeting*, Fajardo, Puerto Rico, pp. 33-34, June 26-July 1, 2016.

M. M. Elsewe and D. Chatterjee, “Modal analysis of patch slot designs in microstrip patch antennas,” *2016 IEEE International Conference on Wireless Information Technology and Systems (ICWITS) and Applied Computational Electromagnetics (ACES)*, Honolulu, HI, pp. 1-2, March 13-17, 2016.

M. M. Elsewe and D. Chatterjee, “Modal analysis of substrate permittivities in microstrip patch antennas,” *2016 IEEE International Conference on Wireless Information Technology and Systems (ICWITS) and Applied Computational Electromagnetics (ACES)*, Honolulu, HI, pp. 1-2, March 13-17, 2016.

M. M. Elsewe and D. Chatterjee, “Mutual coupling characterization of ultra-wideband U-slot microstrip patch array antennas,” *Applied Computational Electromagnetics Society (ACES) Express Journal*, vol. 1, no. 1, pp. 36-39, January 2016.

M. M. Elsewe and D. Chatterjee, "Analysis of nonuniform excitation and element spacing in sidelobe reduction of wideband U-slot microstrip patch phased array antennas," *2015 IEEE International Symposium on Antennas and Propagation & USNC/URSI National Radio Science Meeting*, Vancouver, BC, pp. 1858-1859, July 19-24, 2015.

M. M. Elsewe and D. Chatterjee, "Scan behavior of U-slot microstrip patch phased array antennas," *2014 IEEE Antennas and Propagation Society International Symposium (APSURSI)*, Memphis, TN, pp. 935-936, July 6-11, 2014.

M. M. Elsewe, V. K. Dandu, and D. Chatterjee, “Assessment of computational fidelity of MoM and FEM solvers for characterizing a class of UWB microstrip antennas: 2-element case,” *29th Annual Review of Progress in Applied Computational Electromagnetics*, Monterey, CA, pp. 399-404, March 24-28, 2013.

M. M. Elsewe, V. K. Dandu, and D. Chatterjee, “Assessment of computational fidelity of MoM and FEM solvers for characterizing a class of UWB microstrip antennas: single-element case,” *29th Annual Review of Progress in Applied Computational Electromagnetics*, Monterey, CA, pp. 393-398, March 24-28, 2013.

M. M. Elsewe and D. Chatterjee, "Evaluation of EM absorption loss for continuous monitoring of breast cancer," *2013 IEEE Topical Conference on Biomedical Wireless Technologies, Networks, and Sensing Systems (BioWireleSS)*, Austin, TX, pp. 160-162, January 20-23, 2013.

M. M. Elsewe, "Evaluation of EM absorption loss over breast mass for breast cancer diagnosis," *33rd Annual Intl Conference of the IEEE Engineering in Medicine and Biology Society (EMBS)*, pp. 3897-3900, August 30- September 3, 2011.